

# Structural Health Monitoring of Composite Structures Using Guided Lamb Waves

a project presented to the  
The Faculty of the Department of Aerospace Engineering  
San José State University

In partial fulfillment of the requirements for the degree of  
*Master of Science in Aerospace Engineering*

by  
**Emmanuel J. Nabiswa**

May 2022

approved by  
Dr. Maria Chierichetti  
Faculty Advisor



© 2022  
Emmanuel J. Nabiswa  
ALL RIGHTS RESERVED

## ABSTRACT

# STRUCTURAL HEALTH MONITORING OF COMPOSITE STRUCTURES USING GUIDED LAMB WAVES

by Emmanuel J. Nabiswa

Composite materials are increasingly being used in various applications in the Aerospace industry. Preventive maintenance of such parts is critical in maintaining the high safety standards of the industry. This project report encompasses the application of lamb waves in the non-destructive structural health monitoring of composite parts. The project report defines lamb waves, their background, previous studies, as well as their applications. The report then proceeds to discuss the implementation of SHM using guided lamb waves in a Finite Element Analysis environment. The test specimens (aluminum plate and composite plate) used in the project are modeled in APDL and, a transient analysis leveraging lamb waves is used to detect and approximate locations of modeled damage.

The results obtained provide good approximations of modeled damage in the case of both aluminum and composite plates, whenever the modeled damage is a cut. In the case of modeled delaminated damage, the procedure falls short in some instances while providing good results in other cases. Whenever the modeled delamination is small (0.01 by 0.01m) relative to the plate size, the procedure fell short of a good approximation. However, when the model delamination size was increased (0.01 by 0.03 m) relative to the plate size, the procedure provided good approximations. Hence given these results and corresponding findings from benchmark studies, this report finds that guided Lamb waves provide a good additional resource in the non-destructive structural health monitoring of composite parts.

## ACKNOWLEDGEMENTS

I would like to express my gratitude to my advisor Dr. Maria Chierichetti for her unwavering support, guidance, and advice throughout this project. Her coursework covering Finite element analysis and structures provided the foundation upon which this project was built on. Her expertise in research, structures, material behavior, and finite element analysis has been key in the successful completion of this project. Additionally, her recommendations on various research and technical resources as well as feedback on the project's progress were immensely helpful during the project.

I would also like to extend my gratitude to Dr. Mourtos, my project supervisor, and Dr. Aravamudhan for their support and feedback throughout the report. This was key in the development and completion of the report. Additionally, I would also like to thank the Aerospace Engineering department and faculty at large for providing both the coursework and technical resources that made this project a success.

Finally, I would like to express my gratitude to my family. I would like to thank my parents for their unwavering care, support, constant encouragement, and resources that enabled me to successfully complete this project. I would also like to thank my siblings for their support, encouragement, and constant push to get better in our various disciplines.

# Contents

<b>LIST OF FIGURES</b> .....	iv
<b>LIST OF SYMBOLS</b> .....	viii
<b>1. Chapter 1 – Introduction</b> .....	1
<b>1.1 Motivation</b> .....	1
<b>1.2 Literature Review</b> .....	2
<b>1.2.1 Aerospace composites definition</b> .....	2
<b>1.2.2 Aerospace composite properties</b> .....	5
<b>1.2.3 Defects in composite structures and their effects</b> .....	5
<b>1.2.4 Composite defects detection and monitoring</b> .....	12
<b>1.3 Project Objective</b> .....	13
<b>1.4 Methodology and organization of the report</b> .....	13
<b>2. Chapter 2 – Lamb waves and FEM implementation procedure</b> .....	14
<b>2.1 Lamb waves</b> .....	14
<b>2.1.1 Definition</b> .....	14
<b>2.1.2 Characteristics of Lamb Waves</b> .....	16
<b>2.1.3 Deployment methodology</b> .....	17

2.2 Finite Element simulation on Aluminum plate .....	19
2.3 Geodesic algorithm .....	22
3. Chapter 3- Damage Detection in an Aluminum Plate by FEM Setup .....	24
3.1 Analysis and Parameter choices .....	24
3.1.1 Aluminum plate sample.....	24
3.1.2 PZT Actuator .....	25
3.1.3 PZT sensors .....	26
3.1.4 Loading conditions.....	27
4. Chapter 4 – FEM simulation and results.....	29
4.1 Simulation .....	29
4.1.1 Coupled structural-electrical transient analysis .....	29
4.2 Results .....	31
4.2.1 Deformations .....	31
4.2.2 Electrical Potential output .....	35
4.2.3 Nodal Electric potential output results .....	39
5. Chapter 5 – Damage Location .....	41
5.1 Signal Denoising .....	41
5.2 Arrival times .....	44
5.3 Damage Geodesics .....	50
5.4 Damage locations and comparison .....	54
6. Chapter 6 – Composite plate.....	56
6.1 Model setup .....	56
6.2 Deformations .....	58
6.2 Electric potential output.....	60
6.3 Denoising of Nodal electric potential output .....	63
6.4 Composite plate output signal Spectrograms.....	65
6.5 Damage Geodesics .....	70
6.6 Damage locations.....	74

<b>7. Chapter 7 – Conclusion</b> .....	78
<b>7.1 Aerospace composites and SHM</b> .....	78
<b>7.2 Application of guided Lamb waves in a FEA environment</b> .....	79
<b>7.3 Results</b> .....	80
<b>7.3 Future research</b> .....	80
<b>8. References</b> .....	81
<b>9. Appendices</b> .....	83
A. Sensor output results .....	83
B. MATLAB codes .....	87
B.1 Geodesic location, damage modelling and damage approximation Matlab code .....	87
C. Geodesics from additional simulations .....	95

## LIST OF FIGURES

Figure 1.1 - the percentage of composites used in aircraft manufacturing over years .....	1
Figure 1.2 - Boeing 787 composite fuselage .....	3
Figure 1.3 - Formation of laminate from individual constituent .....	4
Figure 1.4 - Fiber direction types in laminate.....	4
Figure 1.5 - Stacking sequence of a laminate .....	4
Figure 1.6- Voids created in laminate due to loss of vacuum.....	6
Figure 1.7 - Propagation of radial delamination in L-shaped structure. Radial porosity initiates this type of delamination.....	7
Figure 1.8 - Effect of in-plane fiber misalignment on moduli.....	8
Figure 1.9 - Compressive strength retention factors vs wrinkle aspect ratio.....	8
Figure 1.10- Effect of fiber waviness on failure during compressive loading.....	9
Figure 1.11 - Gaps (in pink) and overlaps (in blue) in composite structures.....	10
Figure 1.12- Effects of delamination on the bearing and ultimate strength of composite specimens.....	11
Figure 2.1 - Illustration of primary Lamb wave modes at relatively low frequencies.....	15
Figure 2.2 - Dispersion curves for Lamb waves in a 400 by 420 by 1 mm Al5052 Aluminum alloy plate.....	20
Figure 2.3 - Normalized dispersion wavelength ratio of primary Lamb wave modes for a 400 by 420 by 1 mm Al-5052 Aluminum alloy plate from experimental studies .....	20
Figure 3.1 – A meshed model of an aluminum plate with a PZT actuator and Sensors.....	25
Figure 3.2 - coupling of nodes in actuator shown in green.....	28
Figure 3.3 - A sample residual signal based on data from a healthy and damaged signal [21]....	28
Figure 4.1 - Mesh convergence plots.....	30
Figure 4.2 - Healthy plate deformation at the beginning of the simulation.....	32
Figure 4.3 - Damaged plate deformation at the beginning of the simulation .....	33
Figure 4.4 - Healthy plate deformation in the middle of the simulation.....	33
Figure 4.5 - Damaged plate deformation in the middle of the simulation.....	34
Figure 4.6 - Healthy plate deformation at the end of the simulation .....	34
Figure 4.7 - Damaged plate deformation at the end of the simulation .....	35

Figure 4.8 - Healthy plate electric potential output at the beginning of the simulation .....	36
Figure 4.9 - Damaged plate electric potential output at the beginning of the simulation.....	36
Figure 4.10 - Healthy plate electric potential output in the middle of the simulation .....	37
Figure 4.11 - Damaged plate electric potential in the middle of the simulation.....	37
Figure 4.12 - Healthy plate electric potential output at the end of the simulation.....	38
Figure 4.13 - Damaged plate electric potential at the end of the simulation .....	38
Figure 4.14 - Nodal electric potential output from sensor 1 in both healthy and damaged plate .	39
Figure 4.15 - Nodal electric potential output differences between healthy and damaged plates. Data obtained from sensor 1 .....	39
Figure 4.16 - Nodal electric potential output from sensor 2 in both healthy and damaged plate .	40
Figure 4.17 - Nodal electric potential output differences between healthy and damaged plates. Data obtained from sensor 2 .....	40
Figure 5.1 - Denoised (black) and original (red) data from sensor 1 during the first damaged plate simulation.....	42
Figure 5.2 - Denoised (black) and original (red) data from sensor 2 during the first damaged plate simulation.....	42
Figure 5.3 - Denoised (black) and original (red) data from sensor 1 during the second damaged plate simulation. ....	43
Figure 5.4 - Denoised (black) and original (red) data from sensor 2 during the second damaged plate simulation. ....	43
Figure 5.5 - Wavelet analysis output showing spectrogram corresponding to signal difference from sensor 1 simulation 1. Blue cones indicate positions of abrupt amplitude change, signifying large contrast between healthy and damaged plate signals.....	45
Figure 5.6 - Sampled data images showing position, arrival times, healthy plate voltage, and damaged plate voltage respectively at positions 140,175, and 210. ....	46
Figure 5.7 - Wavelet analysis output showing spectrogram corresponding to signal difference from sensor 2 in simulation 1.....	47
Figure 5.8 - Wavelet analysis output showing spectrogram corresponding to signal difference from sensor 1 in simulation 2.....	48
Figure 5.9 - Wavelet analysis output showing spectrogram corresponding to signal difference from sensor 2 in simulation 2.....	49
Figure 5.10 - First set of geodesic plots from simulation 1, where the modeled damage is centered from plate edges in the y-direction. Arrow indicates arbitrarily chosen center position of geodesic on sensor 1 (center location on sensor 1's Y edge). ....	51
Figure 5.11 - Second set of geodesic plots from simulation 1, where the modeled damage is centered from plate edges in the y-direction.....	52
Figure 5.12 - Third set of geodesic plots from simulation 1, where the modeled damage is centered from plate edges in the y-direction.....	52
Figure 5.13 - First set of geodesic plots from simulation 2, where the modeled damage is skewed towards sensor 2.....	53
Figure 5.14 - Second set of geodesic plots from simulation 2, where the modeled damage is skewed towards sensor 2.....	53

Figure 5.15 - Aluminum plate showing identified damage location from simulation with centered modeled damage. ....	54
Figure 5.16 - aluminum plate showing identified damage location from simulation with un-centered modeled damage. ....	55
Figure 6.1 - Model carbon composite plate layers. Different colors depict different material properties. ....	56
Figure 6.2 - The deformation of a 0.01m thick carbon composite plate with a cut at the beginning of the loading sequence. ....	58
Figure 6.3 - The deformation of a 0.01m thick carbon composite plate with a delamination damage at the beginning of the loading sequence. ....	59
Figure 6.4 - The deformation of a 0.01m thick carbon composite plate with a cut at the end of the loading sequence. ....	59
Figure 6.5: The deformation of a 0.01m thick carbon composite plate with a delamination damage at the end of the loading sequence. ....	60
Figure 6.6 - The electric potential distribution in a composite plate with a cut at the beginning of the ramped load application. ....	61
Figure 6.7 - The electric potential distribution in a composite plate with a delamination damage at the beginning of a ramped load application. ....	61
Figure 6.8 - The electric potential distribution in a composite plate with a cut at the end of a ramped load application. ....	62
Figure 6.9 - The electric potential distribution in a composite plate with a delamination damage at the end of a ramped load application. ....	62
Figure 6.10 - Original and denoised signals of the difference between healthy and delaminated composite plate outputs registered by sensor 1. ....	63
Figure 6.11 - Original (red) and denoised (black) signals of the difference between healthy and damaged (containing cut) composite plate outputs registered by sensor 1. ....	64
Figure 6.12 - Original and denoised signals of the difference between healthy and delaminated composite plate outputs registered by sensor 2. ....	64
Figure 6.13 - Original (red) and denoised (black) signals of the difference between healthy and damaged (containing cut) composite plate outputs registered by sensor 2. ....	65
Figure 6.14 - Spectrogram from the difference between pristine composite plate and damaged (cut) composite plate voltage output derived from sensor 1. ....	66
Figure 6.15 - Spectrogram from the difference between pristine composite plate and damaged (delamination) composite plate voltage output derived from sensor 1. ....	67
Figure 6.16 - Spectrogram from the difference between pristine composite plate and damaged (cut) composite plate voltage output derived from sensor 2. ....	68
Figure 6.17 - Spectrogram from the difference between pristine composite plate and damaged (delamination) composite plate voltage output derived from sensor 2. ....	69
Figure 6.18 - Approximate geodesic damage location plot on composite plate with modeled cut damage. ....	70
Figure 6.19 - Approximate geodesic damage location plot on composite plate with modeled cut damage. ....	71

Figure 6.20 - Approximate geodesic damage location plot on composite plate with modeled cut damage .....	71
Figure 6.21 - Approximate geodesic damage location plot on composite plate with modeled delamination damage .....	72
Figure 6.22 - Approximate geodesic damage location plot on composite plate with modeled delamination.....	72
Figure 6.23 - Approximate geodesic damage location plot on composite plate with modeled delamination damage .....	73
Figure 6.24 - Approximate vs modeled damage (cut) locations on a composite plate.....	74
Figure 6.25 - Approximate vs modeled damage (delamination) locations on a composite plate.	75
Figure 6.26 - Approximate vs modeled damage (delamination) locations on a composite plate.	75
Figure 6.27 - Approximate vs modeled damage (delamination) locations on a composite plate.	76
Figure 6.28 - Approximate vs modeled damage (delamination) locations on a composite plate.	76

## LIST OF SYMBOLS

<b>Symbol</b>	<b>Definition</b>	<b>units</b>
SHM	Structural Health Monitoring	---
BVID	Barely Visible Impact Damage	---
ESL	Equivalent Single Layer	---
h	Plate thickness	mm
k	Wavenumber	---
CL	Longitudinal velocity	m/s
CT	Transverse Velocity	m/s
$\omega$	Circular wave frequency	Hz
A0	Asymmetric mode	---
S0	Symmetric mode	---
Cp	Phase velocity	m/s
CFRP	Carbon fiber reinforced polymer	---
GFRP	Graphite fiber reinforced polymer	---
EMAT		---
SH	Shear Horizontal mode waves	---
CWT	Continuous Wavelet Transform	---
PW	Piezo Wafer transducers	---
PZT	Piezoelectric Transducers	---
AE	Acoustic Emission sensor	---
sensors		
FEM	Finite Element Modeling	---

## LIST OF TABLES

Table 1.1 - Tensile strength reduction in 32 plies graphite/epoxy composite due to scratches....	10
Table 1.2- Effects of foreign object impact on RTW strength .....	12
Table 1.3- Effects of node disbonds on composite strength and failure modes .....	12
Table 2.1 - Magnitude attenuation and amplitude reduction with the distance of propagation along different media for Lamb waves .....	16
Table 2.2 - Magnitude attenuation and amplitude reduction with the distance of propagation along different media for Lamb waves .....	17
Table 2.3 - Modes of Lamb wave generation, distribution, signal collection, and their features.	17
Table 2.4 - Modes of Lamb wave generation, distribution, signal collection, and their features.	18
Table 2.5 - Modes of Lamb wave generation, distribution, signal collection, and their features.	19
Table 3.1 - Model Aluminum plate parameters .....	24
Table 3.2- Model PZT actuator dimensions .....	25
Table 3.3- Piezo ceramics 151 properties [25] .....	26
Table 3.4 - Model PZT sensor dimensions .....	27
Table 3.5 - Element type and element mesh size used in FEA setup .....	27
Table 4.1 - Finite Elements used in models and their characteristics.....	29
Table 4.2 - Mesh convergence analysis .....	30
Table 4.3 - Time integration parameters for the Newmark method .....	31
Table 5.1 - Arrival times corresponding to spectrogram positions.....	50
Table 5.2 - calculated geodesics from arrival times .....	50
Table 6.1: Composite plate material properties .....	56
Table 6.2: SOLSH190 element properties .....	57
Table 6.3 - X and Y coordinates of damage location obtained from geodesic plots .....	73
Table 6.4 - Centroid location distance between modeled and approximated locations and percentages of differences to the plate length.....	77
Table 7.1- Optimal Parameters for simulation models .....	79



# 1. Chapter 1 – Introduction

## 1.1 Motivation

Composite materials are increasingly being used in a variety of settings in the aerospace industry. There has been a significant gradual increase in the use of composite parts in the aerospace industry over the past few decades as shown in figure 1 below.

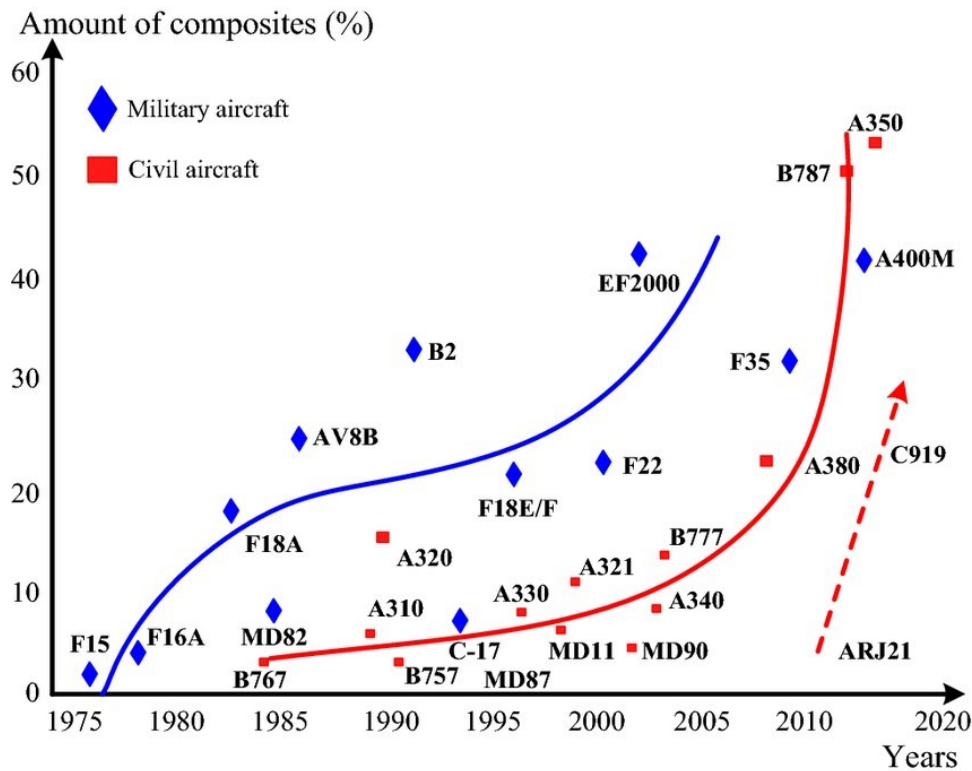


Figure 1.1 - the percentage of composites used in aircraft manufacturing over the years [1]

Structures made from composite materials often are comparatively lighter while maintaining the structural strength required [2]. These structures, however, are susceptible to damage caused by low-velocity impacts such as those caused by bird strikes, stones during takeoffs, or tools being dropped during maintenance [3] [4]. These impacts result in damage such as indentation, cracking, or delamination to the parts, which in turn reduces the structural strengths of the parts making them susceptible to failure [2]. The specific damage modes depend on a variety of factors such as the type of loading, geometry, layup, or stacking sequence [5]. Damage by indentation and cracks on the surface is easily noticed and hence necessary repairs can be made on time, however, damage to interior parts often goes unnoticed and can grow leading to disastrous failures [6]. These hidden damages to composite parts are referred to as Barely Visible Impact

Damage (BVID) in the aerospace industry and call for the routine inspection of composite parts [2].

Structural Health Monitoring (SHM) is one of the methods being increasingly researched to inspect composite parts. It can be defined as the process of continuously detecting and quantifying structural damage within parts using onboard sensors [7]. The sensors relay information either in the form of vibration measurements or acoustics to a processing unit, where the information is analyzed. While most of the objectives for SHM are accomplished using sensors and actual parts in a laboratory setting, these objectives can be simulated using finite element methods software. These simulation results provide a good estimation of what is to be expected during actual SHM in field applications [7].

## **1.2 Literature Review**

### **1.2.1 Aerospace composites definition**

Aerospace composites are a group of materials with a specific set of properties that are difficult to come across within single mineral materials. They can be best described as a combination of two or more distinct materials, whereby one of the materials acts as a supporting matrix, while the other one builds on this scaffolding and reinforces the entire material structure [7]. Aerospace parts made from composite materials utilize either polymer matrix, metal matrix, ceramic matrix, or carbon matrices [8]. These different matrices have different applications within the industry, with the polymer matrices being utilized in airframes while other matrices are used in aircraft engine parts, landing gear parts, and reentry nose cones [8].

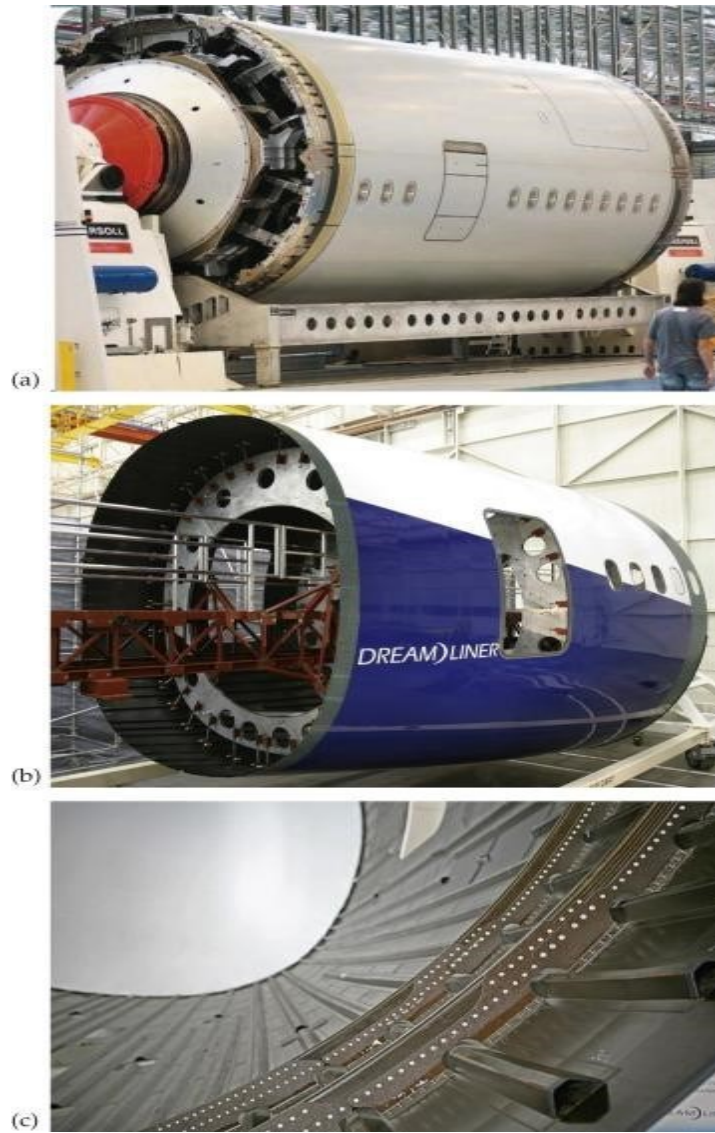


Figure 1.2 - Boeing 787 composite fuselage [8]

Composite parts usually consist of composite laminates. A composite laminate can be termed as superposed layers or folds of unidirectional sheets, fabrics, or mats [8]. Laminates can further be classified into two categories namely, Monolithics and sandwiches [9]. Monolithics consist of a fiber and resin arrangement whereas sandwiches consist of two or more monolithic layers separated by foam or honeycomb [9]. When laminate fibers are aligned in the same direction, the laminate is termed unidirectional, if they are however in a fabric form, it is said to be woven [9]. The images below illustrate the various properties of laminate plies.

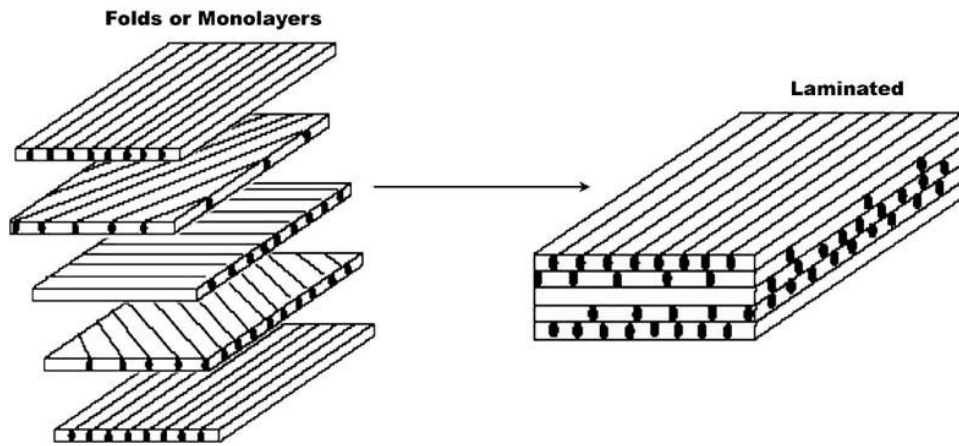


Figure 1.3 - Formation of laminate from individual constituent [9]

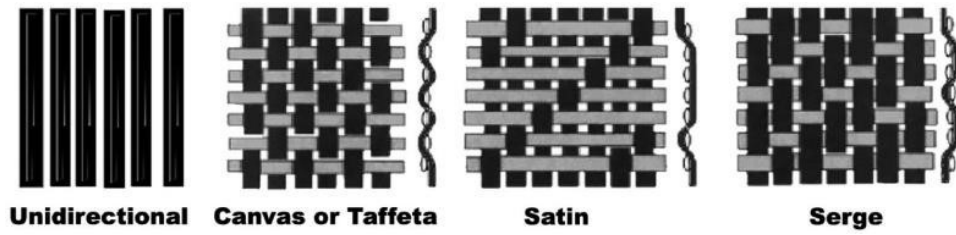


Figure 1.4 - Fiber direction types in laminate [9]

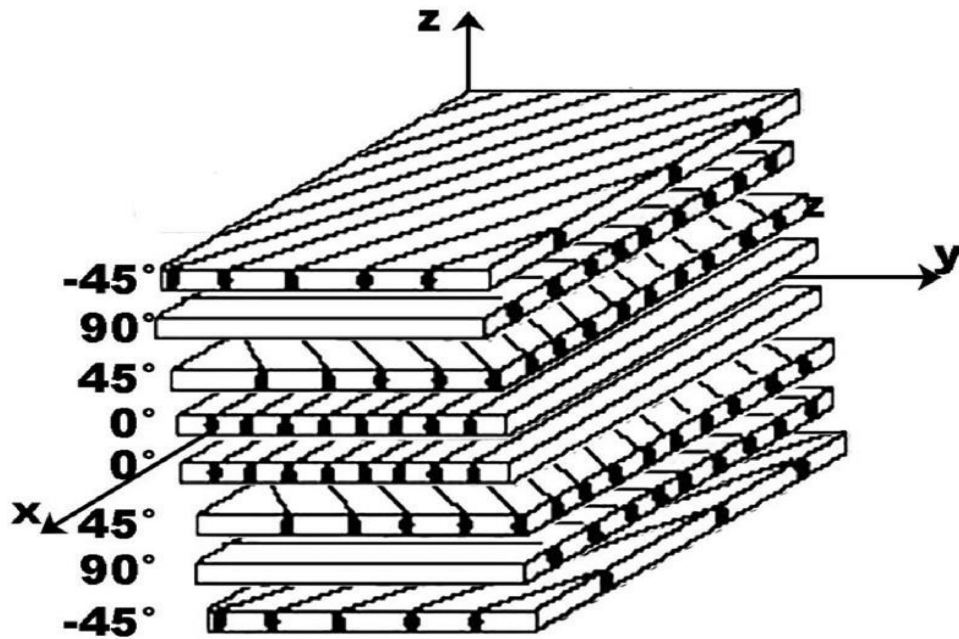


Figure 1.5 - Stacking sequence of a laminate [9]

## 1.2.2 Aerospace composite properties

The need for high-performance composites came about because of the lack of single mineral materials that could provide the high strength requirements, for specific comparatively low weight requirements [8]. Fiber-reinforced composites provide a solution to this issue due to their anisotropic properties. These properties allow for reinforcement of materials in directions with high loading requirements while keeping to a minimum the material amount in low loading directions. The reduced materials in areas that have lower load capacities, however, do not compromise the tensile or compressive strength requirements due to unique composite material properties. Such properties are:

- High tensile strength due to fibrous nature
- High compressive strength due to adhesiveness and stiffness of the matrix Higher strength-to-weight ratio over conventional materials
- Higher stiffness to weight ratio over conventional materials
- Less susceptibility to failure propagation over the entire part due to fibrous nature
- Preferred orientation allows for changes in modulus/strength
- Resistance to corrosion
- Ability to tailor aeroelasticity, hence increasing flight envelope
- Thermal stability
- Low-observability airframes for stealth [8]

## 1.2.3 Defects in composite structures and their effects

Composite parts, like conventional parts, usually have defects that result in reduced performance characteristics. Examples of such defects include:

- Cure cycle anomalies
- Porosity
- non-uniformly distributed voids
- Stratified porosity
- In-plane fiber misalignment
- Waviness in curved parts
- Ply gaps and overlaps
- Cuts, scratches, and gorges
- Edge delamination
- Foreign object impacts [10]

Cure cycle anomalies can be characterized as issues that occur during the manufacturing processes of composites that result in parts that do not fall within the required tolerance limits [10]. Examples of such issues include:

- Loss of vacuum at certain stages

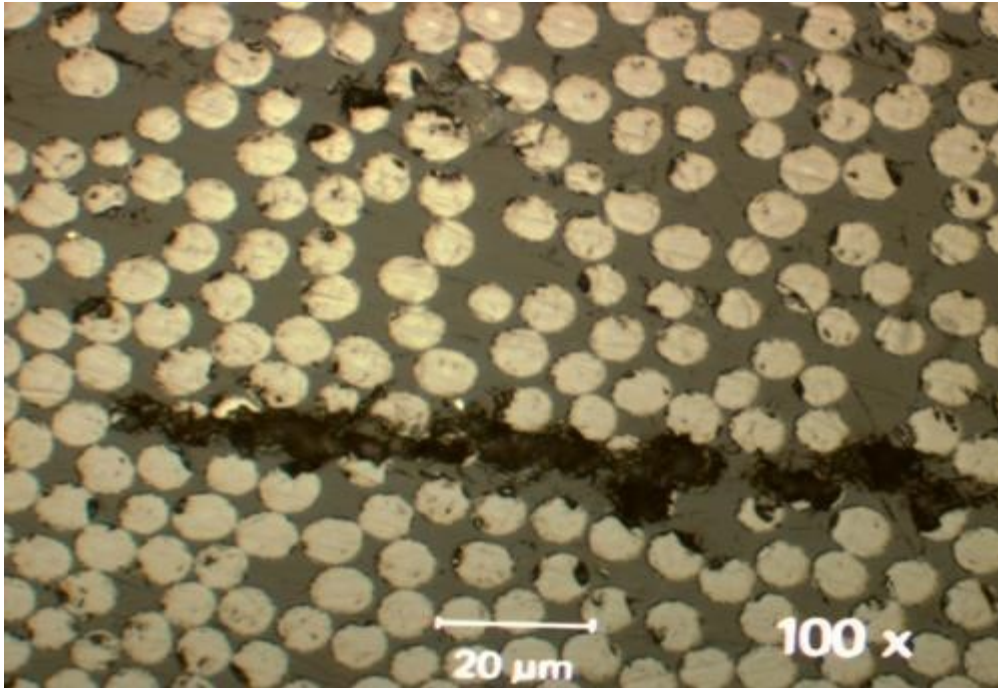


Figure 1.6- Voids created in laminate due to loss of vacuum [11]

- The rapid or slow ramp rate of temperature
- Extended dwell at maximum temperature
- Shortened/ extended dwell after ramp [10]
- 

Testing during certification usually ensures that parts that are produced during such instances meet the tolerance requirements and hence avoid failure [10].

Porosity can be described as the occurrence of a cluster of voids inside the laminate, whereby, the maximum diameter of any void does not exceed 5 mm [10]. Effects of porosity on the part properties include:

- Effect of up to 2% on resin-dominated properties such as compressive strength and interlaminar shear strength
- A similar effect on out of plane shear strength
- Little/ no effect on tensile strength [10]

Although rare, processing and quality-induced errors can result in non-uniformly distributed voids in the laminates. Such voids have been found to have mild strength reduction except at elevated temperatures [10]. For instance, at 265 F the non-uniformly distributed void parts were found to achieve less than 25% compressive strength of similar void-free parts [5]. Uniformly distributed void parts on the other hand achieved 80 percent compressive strength like void-free parts [10].

Porosity along the radius in L-shaped structures can reduce the flange bending strength and overall structural strength due to the initiation and growth of delamination [10]. This is

referred to as stratified porosity. Repeated loading of structures with such a defect causes the porous spots to initiate cracks, which grow into delamination, reducing the structural strengths of parts. The figure below highlights radial delamination due to porosity [10].

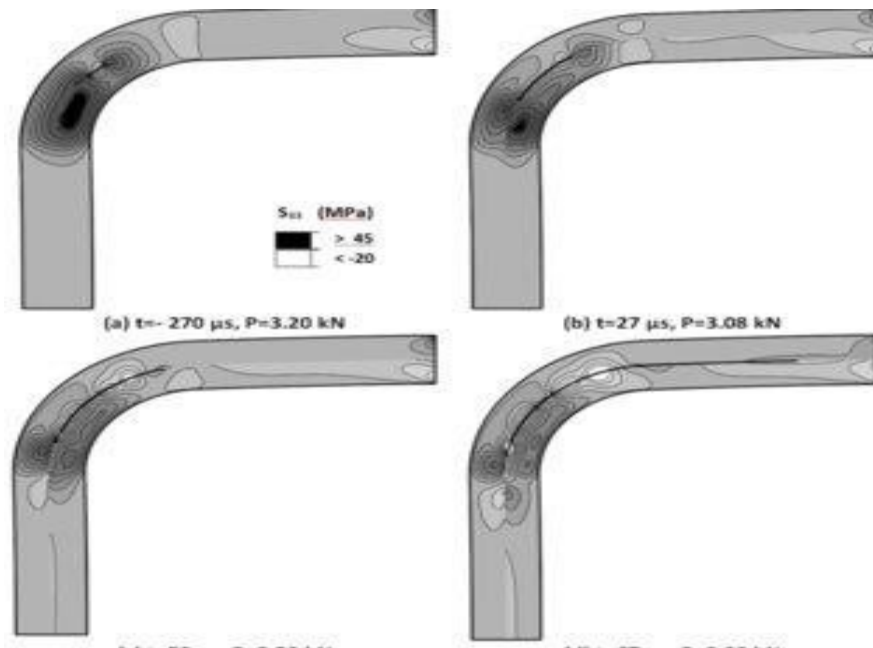


Figure 1.7 - Propagation of radial delamination in L-shaped structure. Radial porosity initiates this type of delamination [12]

A 1-5% in-plane fiber misalignment occurs in wind turbine skins during processing [10]. However, this defect has been found to have little to no effect on the turbine's performance when traditional blade manufacturing techniques are utilized [10]. Significant changes in performance, however, have been noticed in parts involving highly asymmetric and imbalanced laminates [10]. Additionally, glass-fiber parts are less sensitive to misalignment than their carbon fiber counterparts [10].

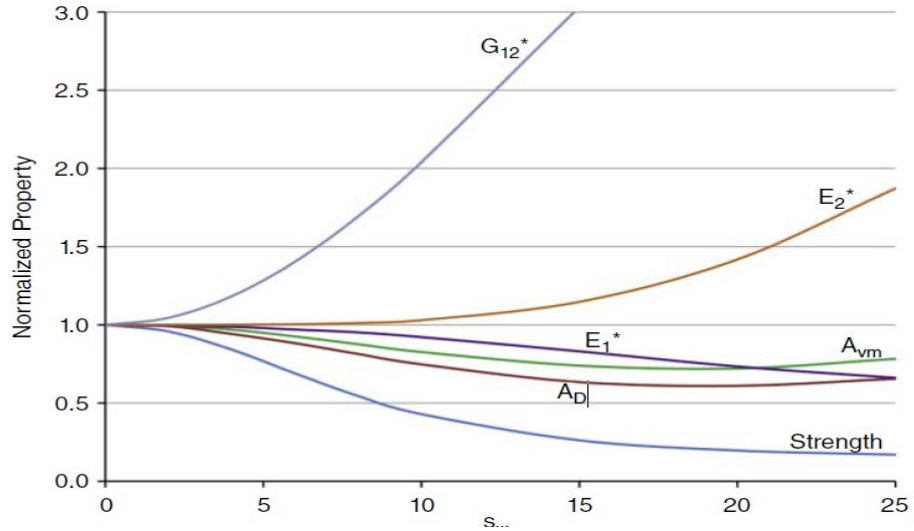


Figure 1.8 - Effect of in-plane fiber misalignment on moduli [10]

Waviness in curved parts has been observed to cause a reduction in load-carrying capacities as well as fatigue life. In compression for a 1 ply, a 10-25 % reduction was observed in presence of waviness in curved parts where the surface ply was in a 0-degree direction [10]. The effects observed in tension were less compared to those in compression, however, it was observed that waviness resulted in delamination during tension loads [10]. The graph below illustrates compressive strength retention properties during loading.

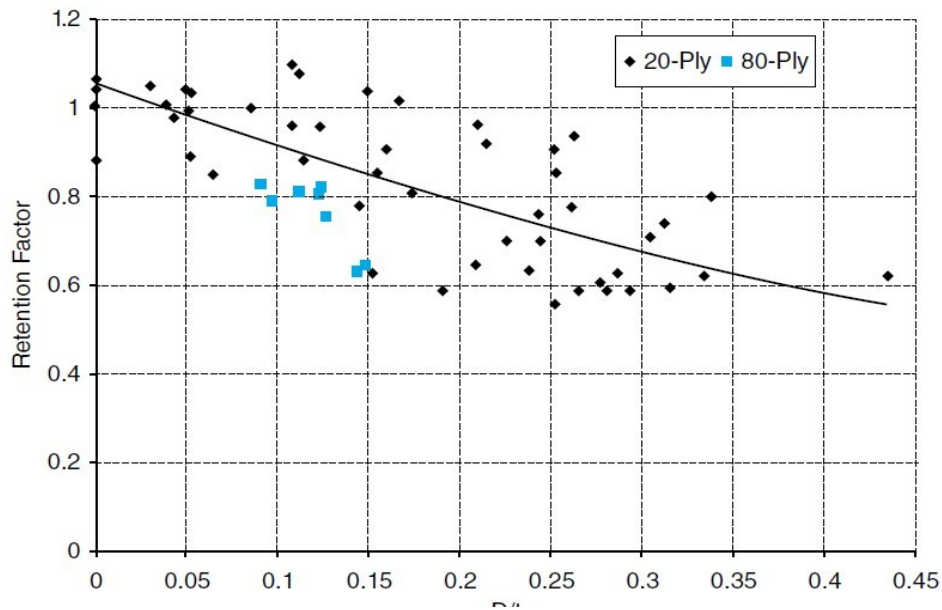


Figure 1.9 - Compressive strength retention factors vs wrinkle aspect ratio [10]

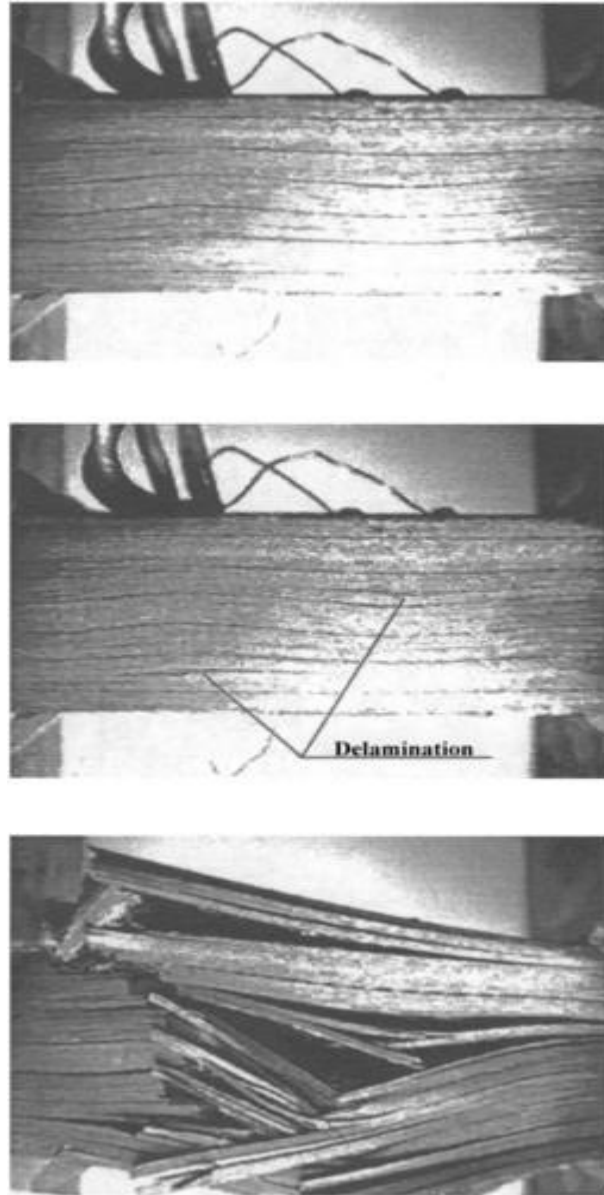


Figure 1.10- Effect of fiber waviness on failure during compressive loading [10]

Ply gaps and overlaps normally occur in parts manufactured by hand or using automated procedures. Some of the effects of these defects include:

- Reduction in the tension and compression failure strains
- Reductions between 6-17 % in compression properties have been associated with these defects depending on the layup
- Unnotched tension properties up to 13% may be affected [10]

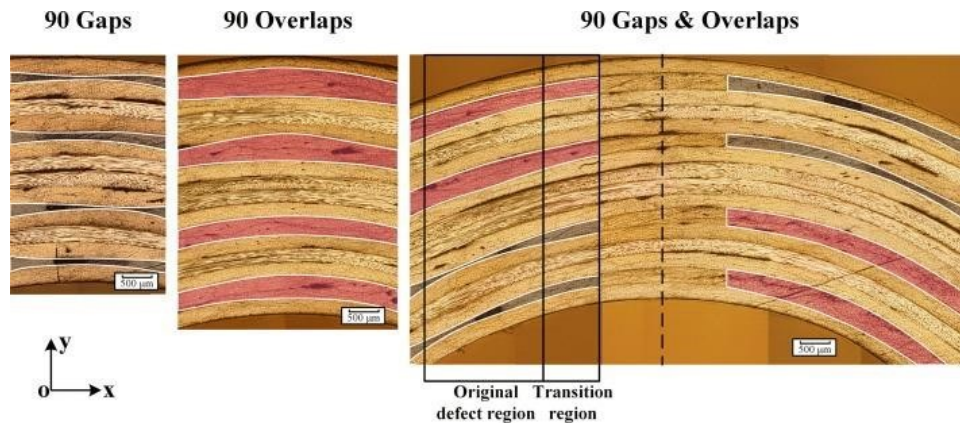


Figure 1.11 - Gaps (in pink) and overlaps (in blue) in composite structures [13]

Cuts, scratches, and gouges can reduce the static strength of a part by up to 50 %. Tests carried out on samples indicated that scratches affected the tension properties significantly, especially if the 0-degree plies were scratched or if they were located at the edge of the specimen [10]. Table 1 highlights the reported tensile strength reductions in graphite/epoxy 32 plies composite laminate due to scratches.

Table 1.1 - Tensile strength reduction in 32 plies graphite/epoxy composite due to scratches [10]

Defect	Depth	% Of basic laminate tensile strength
Center scratch	Three plies	75.1
Center scratch	Six plies	69.7
Edge scratch	Three plies	75.1

Delamination is the separation of laminate layers. In this case, the sample specimens used for the tests had delamination defects 0.3 in and 0.6 in, located at the quarter thickness of the laminate [10]. Edge delamination resulted in a reduction in tensile strength of up to 20 % for larger delamination and 15 % for smaller delamination [10]. The defect also resulted in premature failure during compression [10]. Additionally, delamination in composite parts results in a reduction in the bearing and ultimate strength of the part. This is depicted in figure 7 below which shows the results of compression tests on a variety of samples without and with different sized delamination. Specimen #1 has no delamination, #2 has a 20 mm delamination, #3 has a 40 mm delamination, and #4 has two 20 mm delamination. Specimens #5, #6, and #7 have half rib, one rib, and two rib-sized delaminations respectively. Specimens #8, #9 and #10 have similar sizes as #6, #7 and #8 respectively [14].

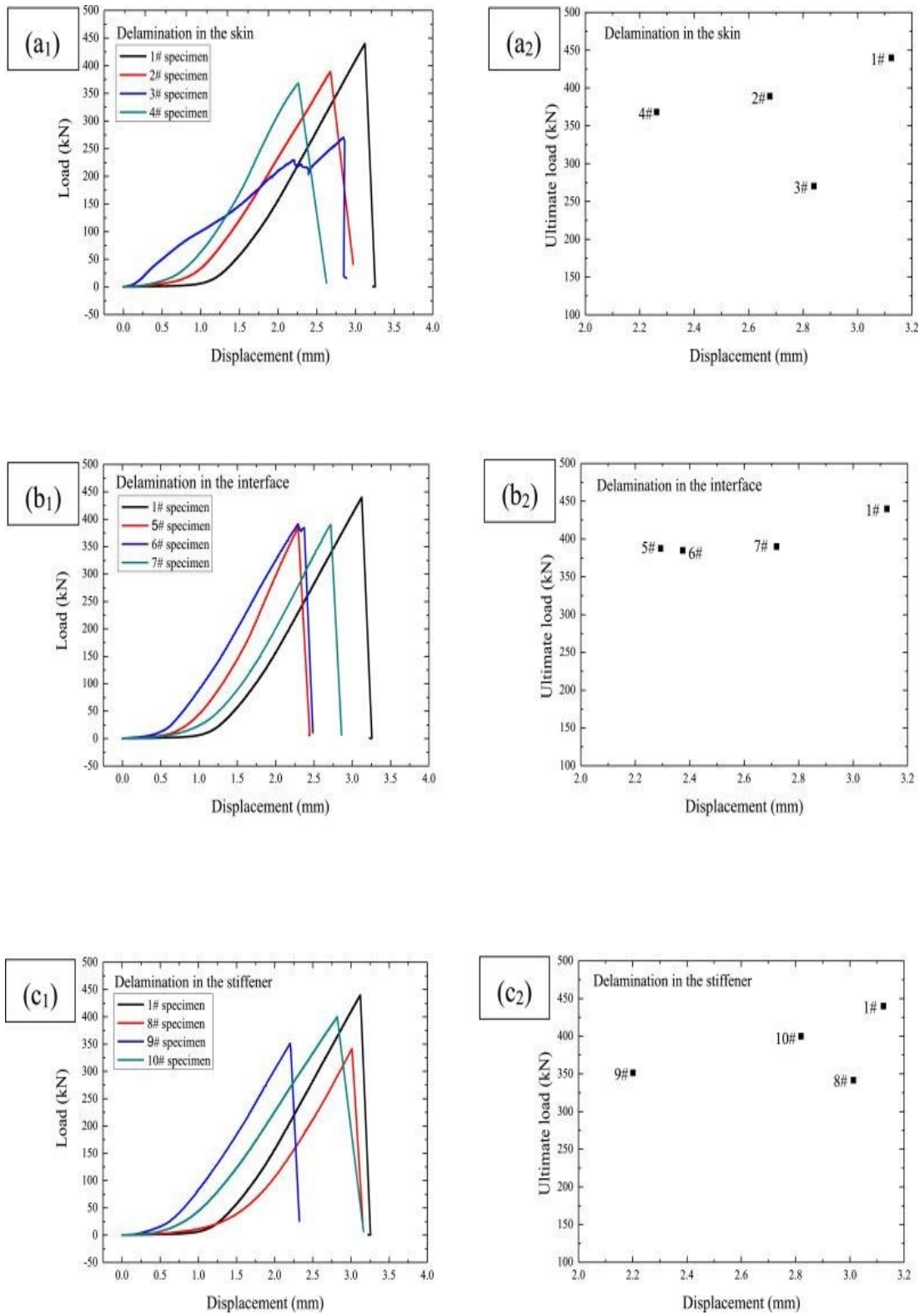


Figure 1.12- Effects of delamination on the bearing and ultimate strength of composite specimens [14]

Impact by foreign objects causes a reduction in the strength of composite structures. Tables 2 and 3 illustrate the effects of foreign object impacts on composite parts:

Table 1.2- Effects of foreign object impact on RTW strength [10]

Laminate	Energy level	Tension strength (static)	Tension residual strength	Compression strength	Compression residual strength
(0/±45 <sub>2</sub> /0/±45) <sub>s</sub>	1	78	72	75	69
(0/±45/0 <sub>2</sub> /90/0) <sub>s</sub>	1	71	77	60	55
(0/±45/90) <sub>2s</sub>	1	91	51	70	35
(0/±45/90) <sub>2s</sub>	2	42	30	61	31

Table 1.3- Effects of node disbands on composite strength and failure modes [10]

Core batch	The density of disbands located	Failure mode	% Of baseline capacity
1	None (baseline)	Facesheet delamination	100
2	Low	Core shear	59
3	High	Core shear	43

### 1.2.4 Composite defects detection and monitoring

Given the critical significance of ensuring the structural integrity of composite structures, especially in high-load demand applications such as the aerospace industry, there are numerous ways to inspect and monitor parts for damage. Some popular non-destructive methods that are in use include:

- Eddy currents
- Visual inspections
- Optical methods
- Laser ultrasonics
- Acoustic emission
- Vibration analysis
- Thermography
- Radiography
- Lamb waves [15]

This project's scope will, however, be limited to the use of lamb waves in a finite element environment.

### 1.3 Project Objective

The objective of the project is to study structural health monitoring (SHM) of composites using guided waves. The project will be carried out by simulating guided Lamb waves through modeled composite parts using finite element analysis tools such as Ansys. Lamb waves are suitable for this type of application, due to their ability to propagate long distances and high sensitivity to minute changes in material properties or structural properties [16]. The velocities of the resulting Lamb waves from the propagation will then be utilized in conjunction with arrival times to locate material changes such as damage [17]. Whereas it may have been ideal to carry out SHM tests on real sample parts, such tests are costly, and the equipment needed to carry them out is also expensive and currently not available for the project. Finite element analysis tools, on the other hand, provide a platform for modeling comparatively similar tests at low costs and are easily available. Hence, the choice to carry out the project using finite element analysis tools.

### 1.4 Methodology and organization of the report

The project's objective will be accomplished through:

- I. Defining guided Lamb waves and the bending moment properties they infer on the mediums they travel through. Due to this property, guided Lamb waves travel at different velocities within delamination regions, since these regions have reduced flexural stiffness caused by the delamination [19]. Defining the procedure to implement damage detection using FEM. These portions are covered in chapters 1 and 2.
- II. Simulating propagation of guided Lamb waves through a modeled Aluminum plate in chapters 3,4 and 5. First, the simulations are carried out in a plate case without damage and then within a plate with a modeled damage, whereby the damage is modeled by holes or cracks [17], [20].
- III. Modeling equivalent single layer (ESL) laminates, first with simple geometry such as a plate using Finite element software. The ESL will then be divided into sub-laminates in the modeled delamination region [18]. This is covered in chapter 6.
- IV.
- V. Simulating propagation of guided Lamb waves through a modeled composite plate in chapter 6, first in the case without delamination and then within the modeled delaminated plates/ modeled plates with simulated holes or cracks and denoting the differences in velocities [17], [20].
- VI. Comparing the results obtained to benchmark studies on SHM using guided waves and performing studies to gauge the accuracy of the results obtained. This is elaborated in chapter 6.
- VII. Summarizing the findings in the report in chapter 7.

## **2. Chapter 2 – Lamb waves and FEM implementation procedure**

The existence of defects in composite structures results in loss of structural strength and premature failure of structures as discussed in the previous chapter. Early identification of such defects through non-destructive SHM is key in keeping structures safe. This chapter explores the use of guided Lamb waves in the identification of defects in structures. The chapter will cover the definition of lamb waves, their characteristics, modes of actuation, distribution, collection, and processing of Lamb wave signals. Additionally, the chapter will elaborate on the procedure to implement SHM on an isotropic aluminum plate using FEM.

### **2.1 Lamb waves**

#### **2.1.1 Definition**

Lamb waves are a type of elastic guided wave that propagates through plates and are a result of reflection, refraction, and mode conversion of bulk waves from the surface of the plates. Their propagation characteristics are dependent on the wave's entry angle, and excitation. Additionally, the propagation characteristics are also dependent on the structural geometry of the medium. When propagated through a medium, the tension and compression of the medium particles result in two primary Lamb wave modes: symmetric (S0) and asymmetric (A0) [19].

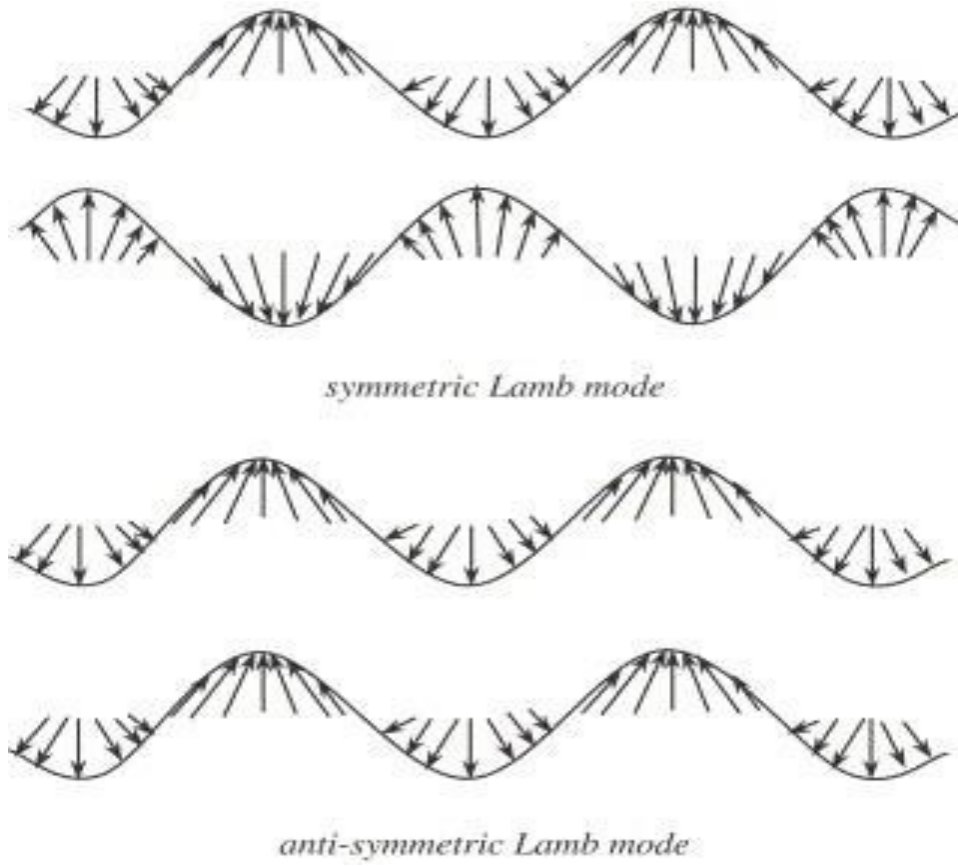


Figure 2.1 - Illustration of primary Lamb wave modes at relatively low frequencies [19]

Given that:

$$p^2 = \frac{w^2}{c_L^2} = -k^2, \quad q^2 = \frac{w^2}{c_p^2} = -k^2, \quad k = \frac{w}{c_p} \quad (2.1)$$

[19]

Where,  $h$ ,  $k$ ,  $c_L$ ,  $c_T$ ,  $c_P$ ,  $w$  are the plate thickness, wavenumber, longitudinal velocity, transverse velocity, phase velocity, and wave circular frequency, respectively.

The symmetric mode can be modeled by the following equation:

$$\frac{\tan(qh)}{\tan(ph)} = \frac{4k^2 qp}{(k^2 - q^2)^2} \quad (2.2)$$

[19]

Whereas the asymmetric mode can be modeled by:

$$\frac{\tan(qh)}{\tan(ph)} = \frac{(k^2 - q^2)^2}{4k^2qp} \quad (2.3)$$

[19]

### 2.1.2 Characteristics of Lamb Waves

Both primary modes and any additional modes of Lamb waves that occur at higher frequencies exhibit dispersion tendencies when propagated through mediums [19]. The dispersion behavior is identified by noting:

- Magnitude attenuation
- wavenumber changes
- Various propagation velocities [19]

Magnitude attenuation has been cited as being of particular concern, especially when deploying guided waves in composite defect detections [19]. However, several studies have been carried out to show that Lamb waves propagate for long distances within composite samples. Table 4 illustrates how far Lamb waves propagate before their amplitude is reduced to 10% of the original signal in various material plates.

Table 2.1 - Magnitude attenuation and amplitude reduction with the distance of propagation along different media for Lamb waves [19].

Materials	Lamb mode	Excitation frequency(kHz)	Attenuation coefficient (mm <sup>-1</sup> )	10% amplitude distance(mm)
CFRP woven 8-ply	S0	250	0.0014	1700
CFRP woven 10-ply	A0	285	0.087	87
CFRP woven 10-ply with stringers (parallel to stringers)	S0	250	0.00078	3000
CFRP woven 10-ply with stringers (perpendicular to stringers)	S0	250	0.0016	1500
GFRP random	S0	220	0.0035	660

Table 2.2 - Magnitude attenuation and amplitude reduction with the distance of propagation along different media for Lamb waves [19]

CFRP/GFRP hybrid (RTM) sandwich honeycomb core	S0	250	0.0036	640
GFRP filament wound pipe	S0	150	0.0015	1600
	S0	250	0.015	150
	S0	150	0.011	210

### 2.1.3 Deployment methodology

In addition to their lengthy propagation distances, Lamb waves can also be generated, and their corresponding resulting signals are collected in several ways. Table 5 shows ways in which this can be achieved.

Table 2.3 - Modes of Lamb wave generation, distribution, signal collection, and their features [19]

Sensor	Applications	Features	Format
Ultrasonic probe	<ul style="list-style-type: none"> <li>Flaw detection</li> <li>Distance and thickness detection,</li> </ul>	<ul style="list-style-type: none"> <li>Exact and efficient</li> </ul>	<ul style="list-style-type: none"> <li>Contact</li> <li>air-fluid coupled</li> </ul>
Laser interferometer	<ul style="list-style-type: none"> <li>Derivation measurement</li> <li>displacement measurement</li> </ul>	<ul style="list-style-type: none"> <li>High precision</li> <li>Expensive</li> </ul>	<ul style="list-style-type: none"> <li>contactless</li> </ul>
Piezoceramics	<ul style="list-style-type: none"> <li>Active sensor</li> <li>Vibration detection</li> </ul>	<ul style="list-style-type: none"> <li>High-frequency response</li> <li>Low driving force</li> <li>cheap</li> </ul>	<ul style="list-style-type: none"> <li>Attaching</li> <li>embedding</li> </ul>

Table 2.4 - Modes of Lamb wave generation, distribution, signal collection, and their features [19]

Piezoelectric paint and PVDF	<ul style="list-style-type: none"> <li>• Vibration and or crack detection</li> </ul>	<ul style="list-style-type: none"> <li>• Easily applied on non-flat shapes</li> <li>• Cheap</li> </ul>	<ul style="list-style-type: none"> <li>• Attaching</li> <li>• embedding</li> </ul>
EMAT	<ul style="list-style-type: none"> <li>• Narrowband</li> </ul>	<ul style="list-style-type: none"> <li>• Avoidance of physical features</li> </ul>	<ul style="list-style-type: none"> <li>• Contact</li> <li>• Attaching</li> </ul>
Accelerometer	<ul style="list-style-type: none"> <li>• Acceleration detection</li> </ul>	<ul style="list-style-type: none"> <li>• High frequency response</li> </ul>	<ul style="list-style-type: none"> <li>• Attaching</li> </ul>
Shape memory alloy	<ul style="list-style-type: none"> <li>• Active sensor</li> <li>• Deformation detection</li> <li>• Active control</li> </ul>	<ul style="list-style-type: none"> <li>• Large force</li> <li>• Low-frequency response</li> </ul>	<ul style="list-style-type: none"> <li>• Attaching</li> <li>• Embedding</li> </ul>
Magnetic sensor	<ul style="list-style-type: none"> <li>• Crack/large deformation with magnetic leakage</li> </ul>	<ul style="list-style-type: none"> <li>• Soft magnetic piece</li> <li>• Magnetic field required</li> </ul>	<ul style="list-style-type: none"> <li>• Contact</li> <li>• Attaching</li> </ul>
Optical fiber	<ul style="list-style-type: none"> <li>• Deformation detection</li> <li>• Temperature detection</li> <li>• Location detection</li> <li>• Line sensing</li> </ul>	<ul style="list-style-type: none"> <li>• Attaching</li> <li>• Embedding</li> <li>•</li> </ul>	<ul style="list-style-type: none"> <li>•</li> </ul>
Eddy-current transducer	<ul style="list-style-type: none"> <li>• Electromagnetic impedance detection</li> </ul>	<ul style="list-style-type: none"> <li>• Good for composites</li> <li>• Too complicated</li> <li>• Expensive</li> </ul>	<ul style="list-style-type: none"> <li>• Attaching</li> </ul>
AE sensor	<ul style="list-style-type: none"> <li>• Changes in physical properties only</li> <li>• Location detection</li> </ul>	<ul style="list-style-type: none"> <li>• Passive sensor</li> </ul>	<ul style="list-style-type: none"> <li>• Attaching</li> <li>• Embedding</li> </ul>
Strain gauge	<ul style="list-style-type: none"> <li>□ Deformation detection</li> </ul>	<ul style="list-style-type: none"> <li>• Applicable in hostile environments</li> <li>• Cheap</li> </ul>	<ul style="list-style-type: none"> <li>• □Attaching</li> </ul>

Table 2.5 - Modes of Lamb wave generation, distribution, signal collection, and their features [19]

FEM	<input type="checkbox"/> Simulation of deformation detection	<ul style="list-style-type: none"> <li>• Expensive software</li> <li>• Relatively inexpensive simulations</li> </ul>	<ul style="list-style-type: none"> <li>• <input type="checkbox"/> FEM software</li> </ul>
-----	--	--	---

Despite there being numerous Lamb wave modes, the two primary modes are the ones that are mostly employed in deformation and displacement detections, with the occasional inclusion of the love/Shear Horizontal (SH) mode [19]. The SH mode was discovered in 1911 by Love. It propagates horizontally among laminate layers and is different from the vertical shear mode [19]. A key question that usually arises is the selection criteria of the mode to employ. Some of the key considerations for a good mode for damage detection include:

- Low attenuation
- Non-dispersion
- High sensitivity
- Good detectability
- Easy excitability
- Effortless selectivity [19]

## 2.2 Finite Element simulation on Aluminum plate

To begin the modeling and simulation phase of the project, guided Lamb waves will be propagated through an aluminum plate. An Aluminum model presents a good test case due to the isotropic nature of the material, which in turn reduces the complexity of the SHM procedure to be carried out. The following steps will be involved in the simulation:

- Obtain the center frequency. This is the suitable frequency at which the ratio of the peak wavelengths of the  $S_0$  and the  $A_0$  modes are maximum.

The Lamb wave used in the simulation will be propagated at this frequency. This frequency is obtained from a plot of the primary mode wavelengths against frequencies, based on the analytical dispersion curve equations of the two modes highlighted in equations 1 and 2. Based on figures 14 and 15, the center frequency will be about 204 kHz [21].

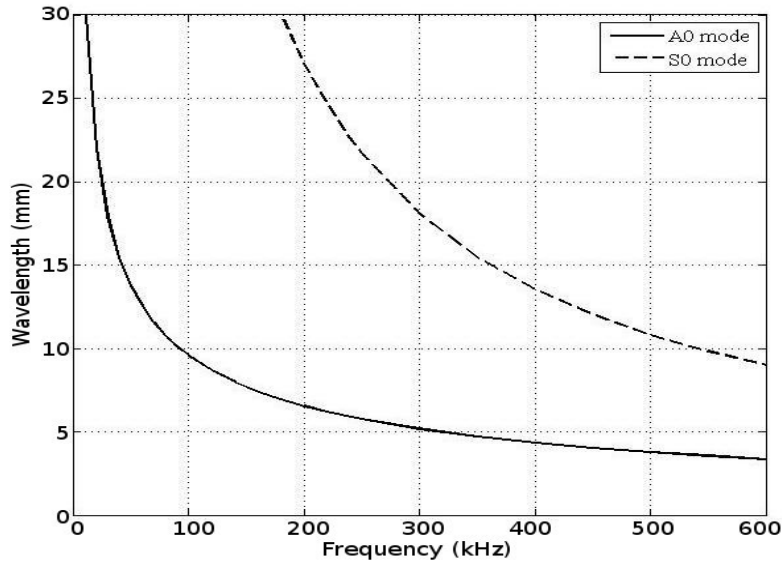


Figure 2.2 - Dispersion curves for Lamb waves in a 400 by 420 by 1 mm Al5052 Aluminum alloy plate [21].

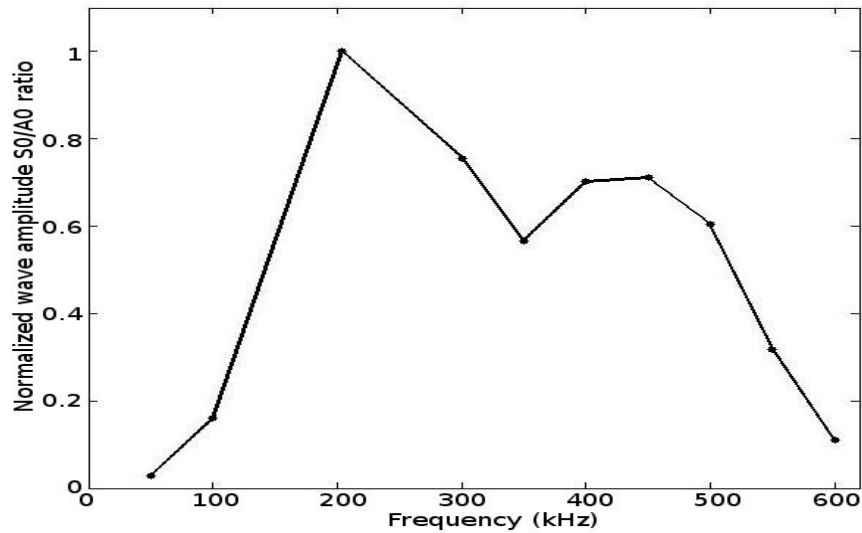


Figure 2.3 - Normalized dispersion wavelength ratio of primary Lamb wave modes for a 400 by 420 by 1 mm Al-5052 Aluminum alloy plate from experimental studies [21]

- Select the type of element to be used in Ansys. The element chosen for this simulation is 3D solid elements. This element type will be utilized to model both the aluminum plate and piezo wafer (PW) actuators and sensors. At each instance two PW will be utilized as sensors while one will be used as an actuator [21].

- Select the element size. The size of the element is based on the lowest wavelength of the Lamb wave modes at the center frequency of the wave that will be propagated through the sample plate. Given the existence of two primary modes  $A_0$  and  $S_0$ , at the 204 kHz frequency, the element size will be based on the  $A_0$  mode, which exhibits a shorter wavelength of 6.545 mm compared to 27.51 mm in the  $S_0$  mode. The element size selected should be such that at least ten elements can fit within one propagated wavelength. Hence, in this case, a 0.5 mm element size is selected [21].
  - Select PW size. Studies have shown that PW diameters that are odd integer multiples of the Lamb wave modes result in high voltage actuation during simulation compared to even integer multiple diameters [21].
  - Model the aluminum plate as well as the PWs in Ansys.
  - Electrically couple the upper and lower face nodes of the PW transducers to form a master node [21].
  - Set a 0-voltage constraint on the lower face of the PW transducers [21].
  - Set the excitation voltage on the upper face of the PW transducers, for the actuators, while measuring the output at the sensor transducer [21].
  - The Newmark algorithm will be used for time integration, where alpha is 0.25 and sigma is 0.5. These values ensure unconditional stability for the method [21].
- Select a time step size. This can be achieved by applying equation 2.4 for rectangular elements. Given  $c_p = \frac{w}{k}$ ,  $h_p = \frac{\lambda_{A_0}}{10}$ , and  $h_y$ , where  $c_p$ ,  $h_x$ ,  $h_y$  are the phase velocity of the  $S_0$  mode, the selected element size in the x-direction, and the selected element size in the y-direction respectively, the time step size  $\Delta t$  is given by [22], [23]:

$$\Delta t = \frac{1}{\sqrt{h_x^2 + h_y^2}} \quad (2.4)$$

[21]

- Once a suitable timestep has been calculated, the finite element simulations are carried out at the center frequency, using a 10-volt peak to peak Gaussian input signal at 8.5 cycles [21].
- Signal processing: The output results are processed using a Continuous Wavelet Transform (CWT), which is defined by equation 2.5. Where  $f(t)$  is the input signal and  $a$  and  $b$  are real number values of the dilation and position, respectively  $c_f(a, b)$  and  $\frac{t-b}{a}$  are the wavelet coefficients of  $f(t)$ , and the wavelet functions, respectively. The multiplication symbol implies complex conjugation of the terms involved [21].

$$c_f(a, b) = \frac{1}{\sqrt{a}} \int_{-\infty}^{\infty} f(t) \varphi * \left( \frac{t-b}{a} \right) dt \quad (2.5)$$

The CWT allows for the splitting of a continuous-time function into wavelets, and hence a time-frequency representation of a signal can be generated. It is used in this case to obtain the arrival

times of the signal by being applied to the residual signal, which is the difference between the damage and healthy response.

A Matlab wavelet software will be utilized to implement this [21].

- The final step is identifying the location of the damage. To implement this, the geodesic algorithm elaborated below is applied.

### 2.3 Geodesic algorithm

This algorithm works on the principle that a wave takes the minimum energy path to travel between any two points. This translates to the shortest distance in a homogenous isotropic medium represented by lines on a planar surface. Upon extraction of these minimum energy paths for a particular geometry, the defect is located by finding the intersection location of the geodesics [21].

Given two sensors  $S_1$  and  $S_2$  located at  $S_{1x}$  and  $S_{2x}$  and  $S_{1y}$  and  $S_{2y}$  and  $v$ , being the velocity of the wave in the medium, let  $t_1$  and  $t_2$  be the time taken by the waves generated from the damage  $s$  to reach the sensors  $S_1$  and  $S_2$ , respectively. With the time taken to reach the sensors being proportional to the distance between the source and the sensors, the following governing equations can be obtained [21]:

$$D(S_1 - S) = Vt_1 \quad (2.6)$$

$$D(S_2 - S) = Vt_2 \quad (2.7)$$

If a source is located at  $S_x$  and  $S_y$  on a planar surface, then the distance between the source and sensors 1 and 2 is given by equations 7 and 8 respectively [21].

$$D(S_1 - S) = \sqrt{(S_{1x} - S_x)^2 + (S_{1y} - S_y)^2} \quad (2.8)$$

$$D(S_2 - S) = \sqrt{(S_{2x} - S_x)^2 + (S_{2y} - S_y)^2} \quad (2.9)$$

Once the geodesic distances have been extracted in equations 7 and 8, the damage location can be found by locating the intersection of geodesics which satisfy the condition [21]:

$$D(nkS_i) = Vt_i \quad (2.10)$$

Where for a given mesh, let  $nk$  be the  $K^{th}$  node in the mesh,  $D(nkS_i)$ , the distance between the node and the sensor  $i$  and,  $t_i$  the hit arrival time between sensors  $S_i$  and the damage. A curve corresponding to the geodesic distance can be represented as a set of nodes by equation 10 [21].

$$C_{ij} = nk | D(nkS_i) = Vt_i \quad (2.11)$$

The intersection point (damage location) in the set is given by equation 11 [21].

$$S = (n|C1s \cap C2s \cap C3s \cap C4s) \quad (2.12)$$

### 3. Chapter 3- Damage Detection in an Aluminum Plate by FEM Setup

This chapter defines the set-up, parameter choices, and design choices for a FEM simulation carried on an aluminum sample plate. These three key inputs are implemented using mechanical APDL software to obtain initial residual signals necessary for the arrival times. The arrival times coupled with signal velocities in the plate form the basis for the identification of damage locations in sample specimens. While the chapter will cover most of the details involved in the setup and simulation, the results obtained in the initial simulations will be presented in chapter 4.

#### 3.1 Analysis and Parameter choices

The modeling and simulation are carried out using Mechanical APDL software. The APDL interface provides a powerful yet affordable computational tool to carry out the simulations. A choice is made to carry out the simulation using transient structural analysis. This choice allows the input loads to be modeled as a function. The analysis type also allows for an output result of amplitude vs time signal. The difference in the output signal between the healthy and damaged response provides the residual signal necessary for calculations of the group velocities.

The analysis involves four key components:

- Aluminum plate sample
- PZT actuator
- Two PZT sensors
- Loading conditions

##### 3.1.1 Aluminum plate sample

The aluminum sample plate chosen for the analysis is defined by parameters highlighted in table 6. The selected sample size is kept small to keep the computational time cost of the analysis low. The specific aluminum material choice is arbitrary. The material selection choice is, however, restricted to elastic, isotropic materials.

Table 3.1 - Model Aluminum plate parameters

Aluminum plate parameters	
Length (m)	0.024
Width (m)	0.024
Height (m)	0.001
Poisson ratio	0.33
Young's modulus	7.030 E10
Density (kg/cubic meter)	2680

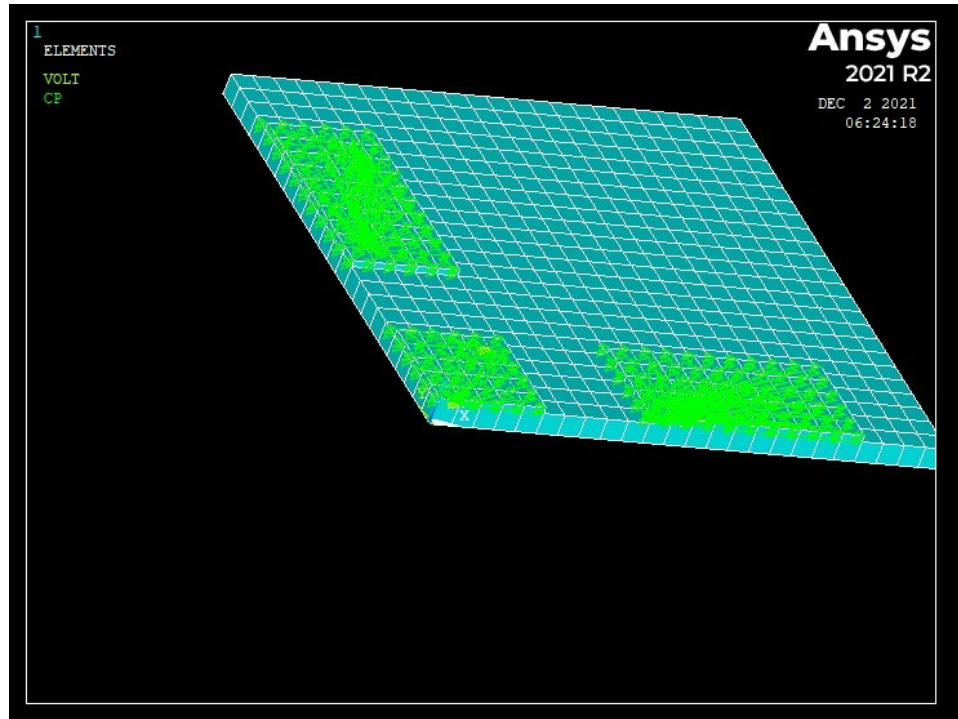


Figure 3.1 – A meshed model of an aluminum plate with a PZT actuator and Sensors

### 3.1.2 PZT Actuator

A PZT actuator is a device that transforms electrical energy into mechanical energy in the form of a displacement or force [24]. PZT actuators are made of Piezo materials, which when subjected to an electrical signal, change their dimensions [24]. This change in dimension is useful in mechanical systems since it can be precisely calibrated to achieve certain desired motions. The precise motions can be arrived at by altering the applied voltages to the actuator [24]. It is this principle that makes PZT actuators great at non-destructive structural health monitoring techniques, such as the use of lamb waves.

A PZT actuator with the dimensions in Table 7 is implemented within the model.

Table 3.2- Model PZT actuator dimensions

PZT actuator dimensions in meters		
Length	5	10 <sup>-3</sup> m
Width	5	
Height	3	

The model PZT actuator material is selected to exhibit anisotropic properties, while its relative permittivity is modeled as orthotropic. Both selections are modeled by the PZT properties of a Piezo ceramics 151 shown in table 8.

Table 3.3- Piezo ceramics 151 properties [25]

Parameters	Symbols	Values	Unit
Density	$\rho$	7800	Kg/m <sup>3</sup>
Dielectric loss factor	$\tan\delta$	0.02	10-12 m2/N
Compliance	S11	15.0	10 <sup>-8</sup> F/m
	S22= S33	19.0	
	S12 = S21	-4.50	
	S13 = S31	-5.70	
	S23 = S32	-5.70	
	S44 = S55	39.0	
	S66	49.4	
Electric Permittivity	T 11	1.75	10 <sup>-8</sup> F/m
	T 22	1.75	
	T 33	2.12	
PZT strain coefficients	d31	-2.10	10 <sup>-10</sup> m/V
	d32	-2.10	
	d33	5.0	
	d24	5.80	
	d15	5.80	

Two node surfaces are created within the PZT actuator. A Master node at the top surface, and a lower surface node which is attached to the aluminum plate. The two nodes are then coupled, with the voltage flowing from the Master node to the lower surface node. The actuator is then glued to the plate and the motion of the side is constrained in the x and y-direction. A voltage boundary, modeled as a function to include the suitable wave frequency for the lamb waves, is then applied to the Master node.

### 3.1.3 PZT sensors

PZT sensors operate on a principle opposite to PZT actuators, in that they transform mechanical energy into an electrical signal [24]. PZT sensors operate based on the Piezo material property, that the material generates an electrical potential when mechanical energy in form of a force or displacement is applied [24]. Piezo materials consist of a balanced number of positively charged and negatively charged ions, and thus are electrically neutral [24]. When a mechanical force is applied on one end, it causes a redistribution of these ions, resulting in the creation of an electrical potential [24]. This property can be utilized in mechanical systems to precisely measure displacements, forces, and stress which are proportionally collected as voltages by the sensors [24].

Two PZT sensors are incorporated into the model to receive to collect the response. The sensors apply similar Piezo ceramic 151 material properties listed in table 7. The sensors are larger

than the actuator, to increase the area of the nodes that are coupled to collect the output response. As was the case in the actuator model, the sensors have two node surfaces, a Master node, and a lower surface node. The coupling direction of the nodes is, however, from the lower surface nodes to the Master node. The sensors are glued to the plate as well. Both sensors are of equal dimensions and are defined by parameters in table 9.

Table 3.4 - Model PZT sensor dimensions

Dimension (meters)	Sensor 1	Sensor 2
Length	1E-2	1E-2
Width	5E-3	5E-3
height	3E-3	3E-3
Distance from actuator in x direction	1E-2	0
Distance from the actuator in the y-direction	0	1E-2

### 3.1.4 Loading conditions

The model plate, PZT actuator, and PZT sensors are meshed by the following parameters in table 10.

Table 3.5 - Element type and element mesh size used in FEA setup

Model	APDL element type	Element length *10 <sup>-3</sup> m
Aluminum plate	Solid45	1
PZT actuator	Solid5	1
PZT sensors (both)	Solid5	1

The choice of the mesh size is dependent on the lamb wave wavelength as mentioned in the previous chapter. The element length is selected such that, at least ten elements fit within one wavelength of the propagated signal.

Several constraints are applied to the plate, actuator, and sensors to avoid singularity conditions. Both the x and y axes of the plate, actuator, and sensors are constrained to zero degrees of freedom in the y and x directions, respectively. The lower surface of the plate is constrained to zero degrees of freedom in the x, y, and z directions.

Voltage boundary conditions are applied to the actuator Master nodes and the lower surface nodes. The Master node boundary condition is defined as voltage modeled by a Hanington function, which can be used to model lamb waves at suitable frequencies based on the material. The Hanington function is defined in equation 13 at a 204 kHz frequency. The lower coupled surface node boundary condition is modeled as a zero-voltage condition. No loads are defined for the sensors.

$$A = \frac{\alpha}{2} * (1 - \cos(2 * \pi * f_0 * t)) * \sin(2 * \pi * f_0 * t) \quad (3.13)$$

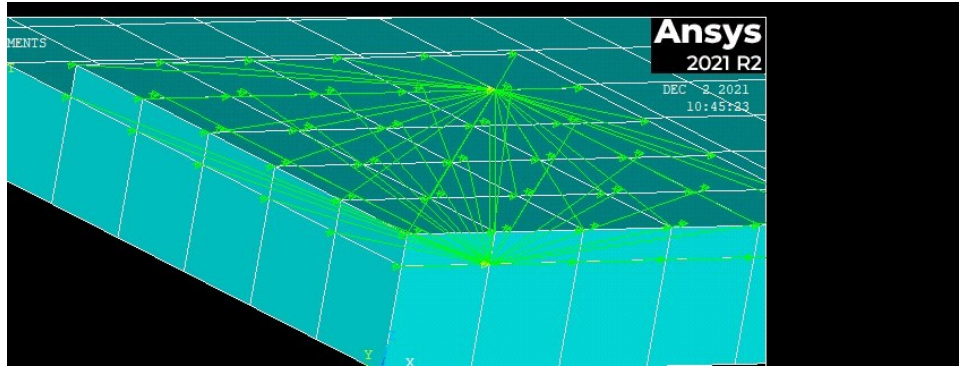


Figure 3.2 - coupling of nodes in actuator shown in green

While results for the simulation will be presented in the next chapter, figure 18 illustrates a sample residual signal that is to be expected from the simulation.

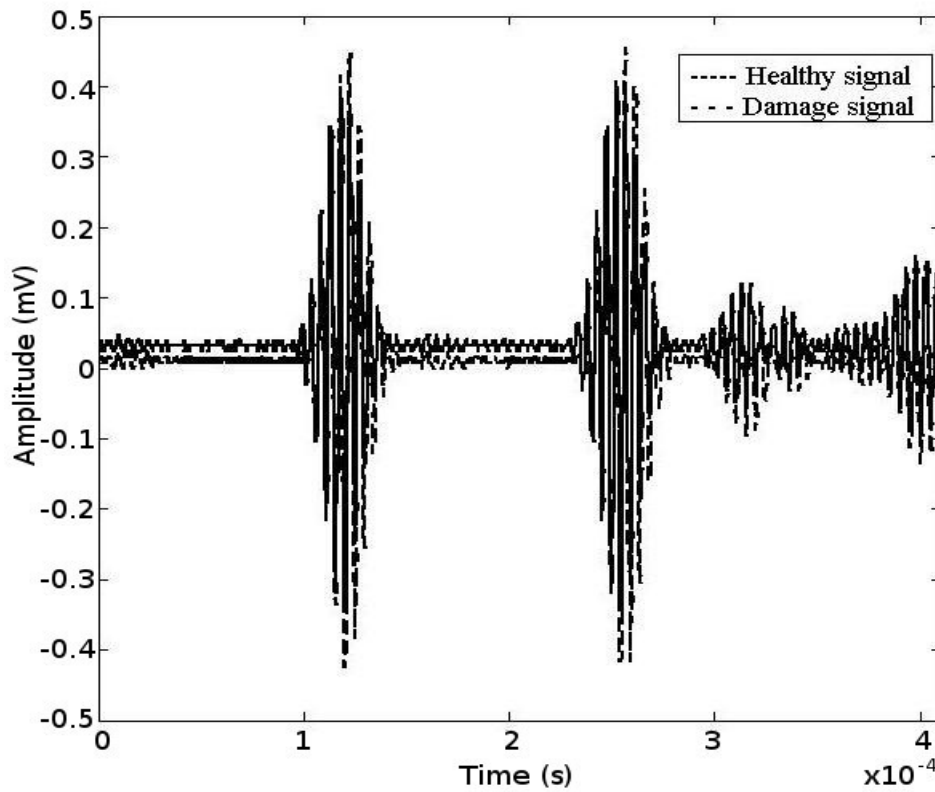


Figure 3.3 - A sample residual signal based on data from a healthy and damaged signal [21]

## 4. Chapter 4 – FEM simulation and results

Following the setup and simulation procedure laid out in chapter 3, this chapter presents the results obtained and the sequential analysis. The chapter defines the boundary conditions involved in the simulation setup, a mesh convergence analysis, and ultimately the transient analysis results. The results incorporate plate deformations plots as well as nodal electric potential outputs from the sensors. The results in this chapter will be utilized in establishing identified damage locations using wavelet analysis in chapter 5.

### 4.1 Simulation

#### 4.1.1 Coupled structural-electrical transient analysis

Following the successful setup of the model as explained in the previous chapter, a coupled structural-electrical transient analysis is carried out as described in this chapter. After selecting the type of analysis to be carried out in APDL, the type of elements to be used in modeling the plate, sensors, and actuators are selected. The choice of elements depends on factors explained in the previous chapters. Element types Solid45, Solid5, and circuit94 are selected. Their characteristics are illustrated in table 11 below.

Table 4.1 - Finite Elements used in models and their characteristics

Element	Degrees of freedom	Applications
Solid45	UX, UY, UZ	Stress analysis
Solid5	UX, UY, UZ, VOLT	<ul style="list-style-type: none"><li>Structural-electro coupled analysis</li></ul>
Circuit94	VOLT, CURR	<ul style="list-style-type: none"><li>Resistor, capacitor, inductor, current source, voltage source for a PZT-circuit, and charge-based transient and harmonic analysis</li></ul>

The next step involves defining material models, and model dimensions. This includes declaring material properties for the plate, actuator, and sensors. The material properties are listed in tables 5 and 7. Resistance of 200 ohms is also defined for the sensors, ensuring they are properly constrained and thus can register voltage outputs. Once the material properties are saved, the geometry of the models is then set up. This is achieved using dimensions declared in the previous chapter. The volumes are then glued together to ensure that meshed elements at joints overlap.

The various volume configurations are then assigned material attributes, and element type attributes. This ensures that modeled sensors and actuators receive PZT material attributes and that the plate volume models the behavior of aluminum material. The volumes are then meshed using a selected element length arrived at by carrying out a mesh convergence study. The mesh

convergence analysis is carried out to ensure that the element size choice results in a higher-order accuracy in the output. Table 12 provides data from the mesh convergence analysis. While there is still a significant change in % output when increasing the number of elements from 1.4E3 to 7E4 and sequentially 6.5E-4, the simulation run time and memory required tradeoff is too costly for the latter. A decision is therefore made to run the simulations at an element size of 7.5E-4, due to the limitations, with hindsight, that the level of accuracy of results is slightly lower than what could be achieved.

Table 4.2 - Mesh convergence analysis

Element size (m)	Number of elements	% change in output	Simulation run time
2.5E-3	898		Less than 2 minutes
1E-3	14000	39.4	5 minutes
7.5E-4	36486	12.0	45 minutes
6E-4	71309	16.0	Over 2 hours

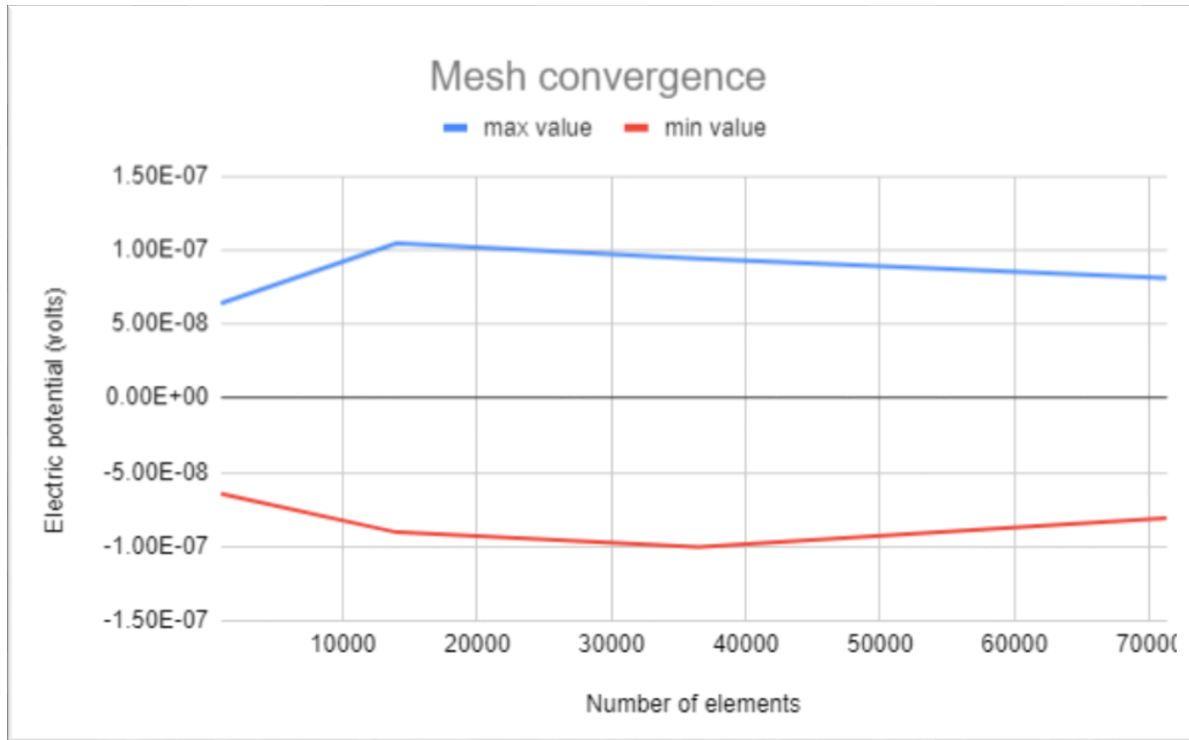


Figure 4.1 - Mesh convergence plots

Once the models have meshed, the top and lower nodes of actuators and nodes are coupled. This coupling connects all the nodes at the top and similarly at the bottom, allowing for loads to be applied only at a singular leading node, as well as data to be collected, at a single leading node in a coupled set.

The next step involves establishing boundary conditions. Setting up boundary conditions for the model ensures that singularity and unconstrained errors are avoided. For the plate-sensor-actuator combo, motion is allowed in:

- The UX degree of freedom (DOF)
- The UY DOF
- The UZ DOF and,
- Rotation
- for all nodes except, for the plate nodes at  $UY = 0.05$  m. Motion for the exempt nodes is restricted in the UX, UY, and UZ directions. This DOF constraint prevents rigid body motion, and thus, makes it possible for the convergence of a solution.

For the sensors and actuators, electro-mechanical coupled analysis boundary conditions must be observed. This involves allowing freedom in:

- The UX DOF
- The UY DOF
- The UZ DOF and
- The Voltage DOF

The Temperature DOF is restricted to zero since the simulation does not involve huge fluctuations in temperature. As a result of the minimal changes in the temperature variable, its role in the analysis can be assumed to be negligible. Therefore, no declarations for thermal properties are needed in the setup.

The final preparation step involves time selection. This is achieved by defining the end time for the simulation and the time steps. The choice for the end time for the current simulation is selected as  $5E-4$  seconds, while the time step is selected as  $2E-6$  seconds. The choice of this time step as mentioned in chapter two is to ensure that more than at least ten elements fit within one wavelength of the propagating Lamb wave. In addition to the end time and time step, the Newmark algorithm requires the declaration of time integration parameters. These already established parameters for the algorithm are listed in Table 13.

Table 4.3 - Time integration parameters for the Newmark method [21]

Integration parameter (Newmark method)	Value
Alpha	0.25
Beta	0.5
Theta	0.5

## 4.2 Results

### 4.2.1 Deformations

Figures 20 to 25 illustrate the deformation that takes place within the model during the simulation. As expected, there is significant deformation to the actuator relative to other parts of the model. This is a result of the actuator being the initial load application point. It is also noted

that deformation across the whole model increases as data is collected from one set to the next. This is a result of ramping up of the Lamb wave. A higher level of actuator deformation is noticed in the last set of results compared to the first two, this is due to the ramped load reaching maximum values, hence resulting in larger deformations.

There is a subtle difference in deformations for the healthy and damaged plate models across the three sets of results. The difference is very small to accurately depict it from deformation models, due to the small size of the damage relative to the model. The discussion on the difference in output results between the two models is therefore left for the nodal electric potential output, where plots give a clearer picture.

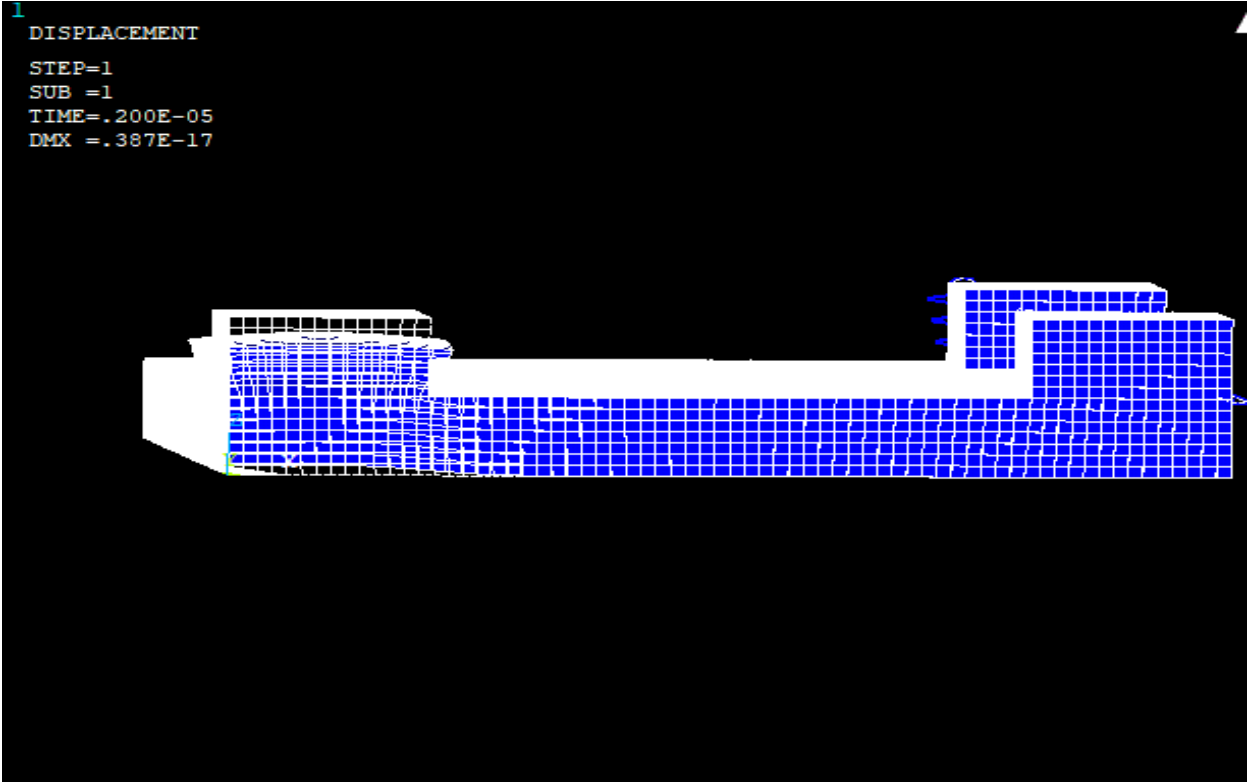


Figure 4.2 - Healthy plate deformation at the beginning of the simulation

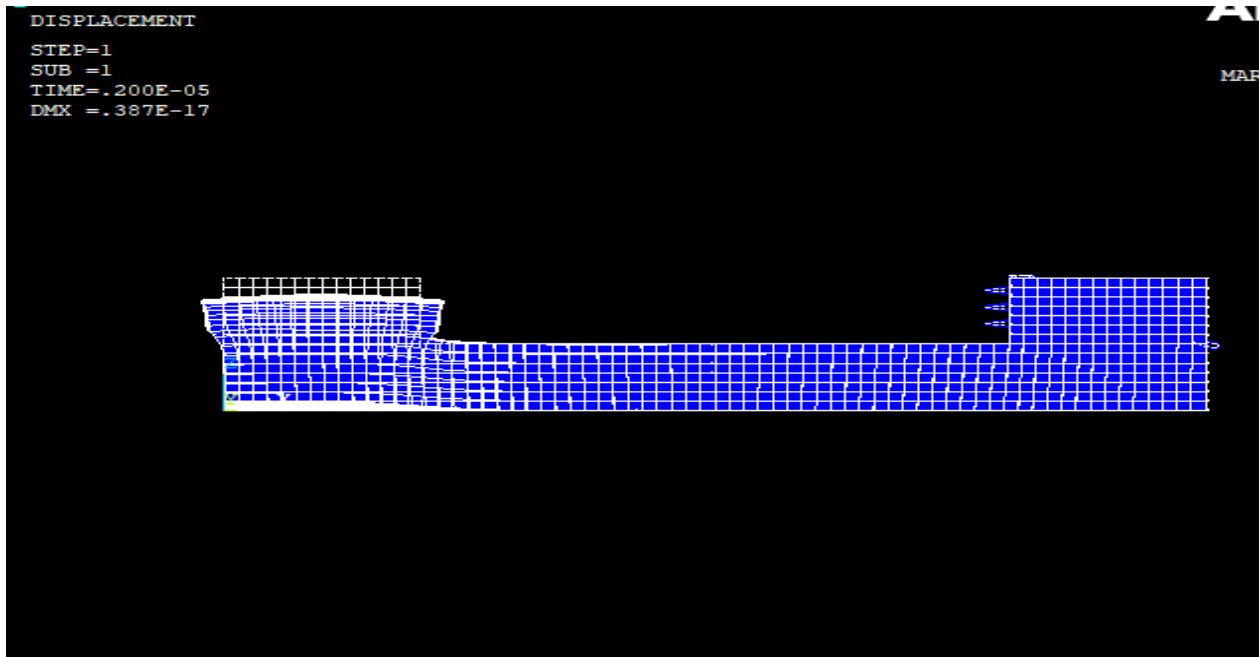


Figure 4.3 - Damaged plate deformation at the beginning of the simulation

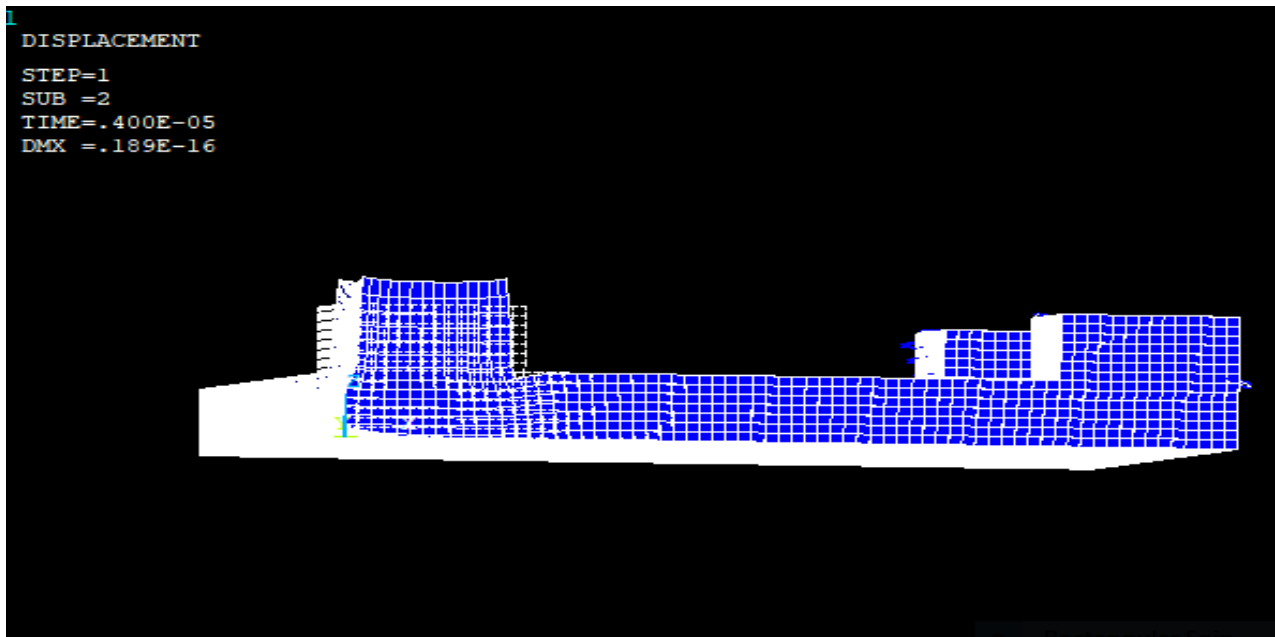


Figure 4.4 - Healthy plate deformation in the middle of the simulation

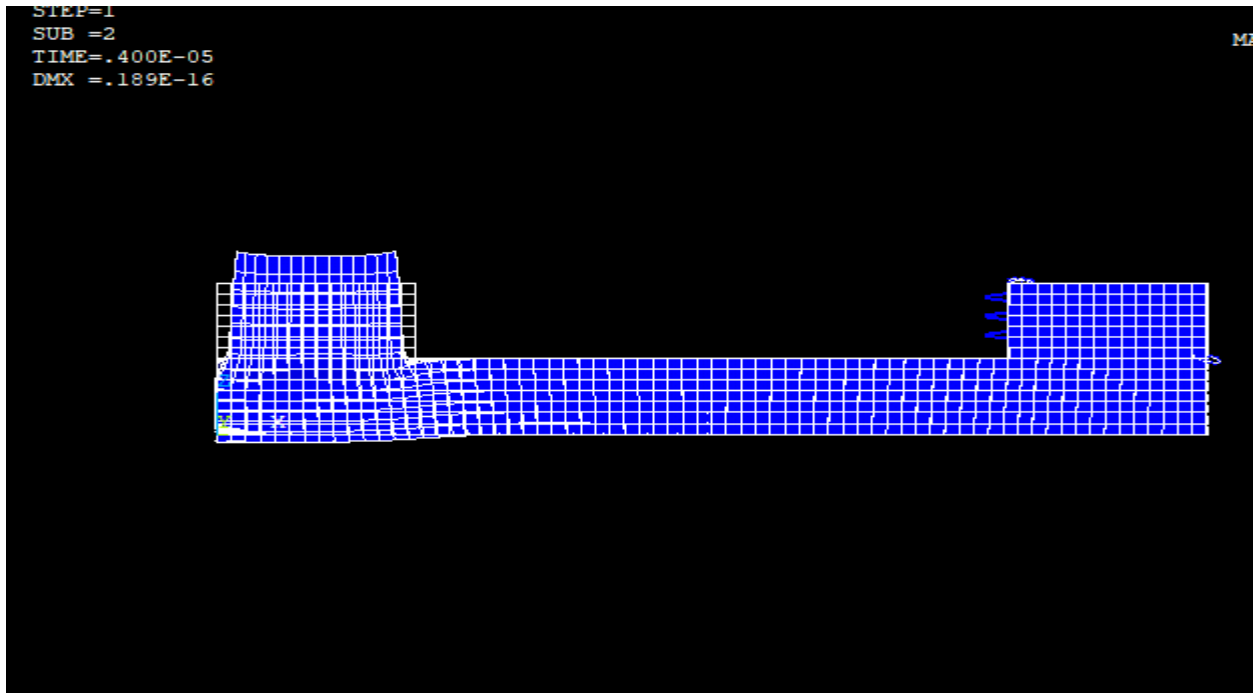


Figure 4.5 - Damaged plate deformation in the middle of the simulation

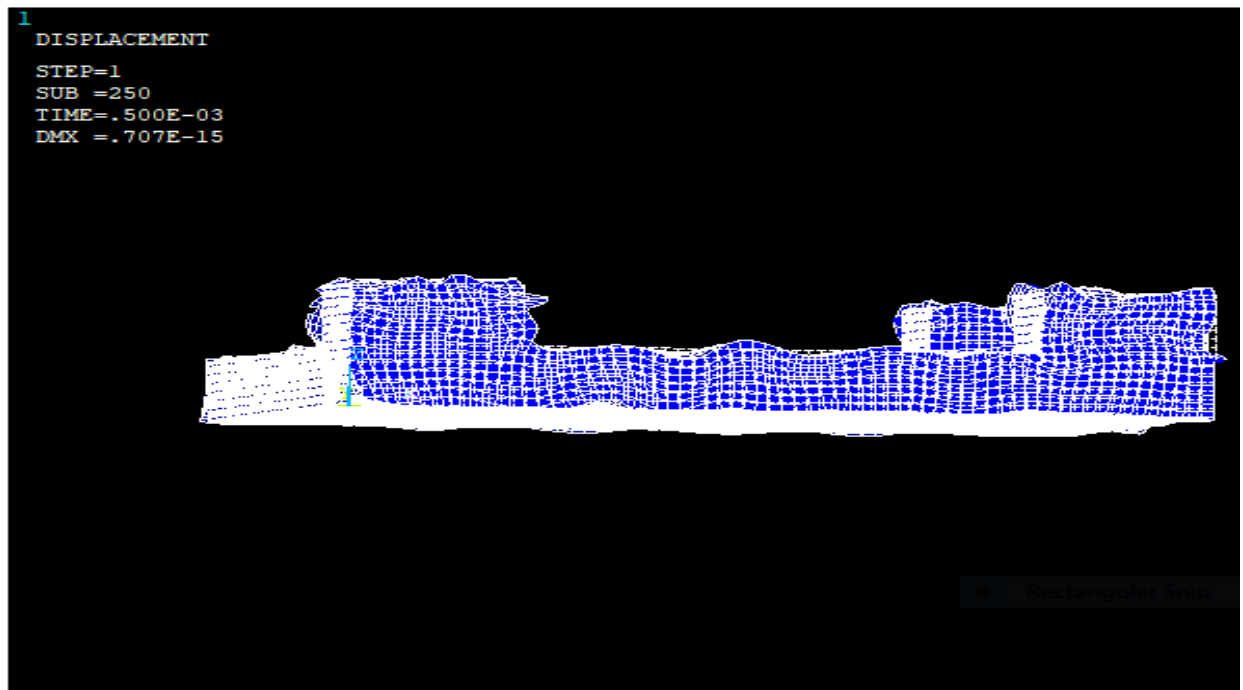


Figure 4.6 - Healthy plate deformation at the end of the simulation

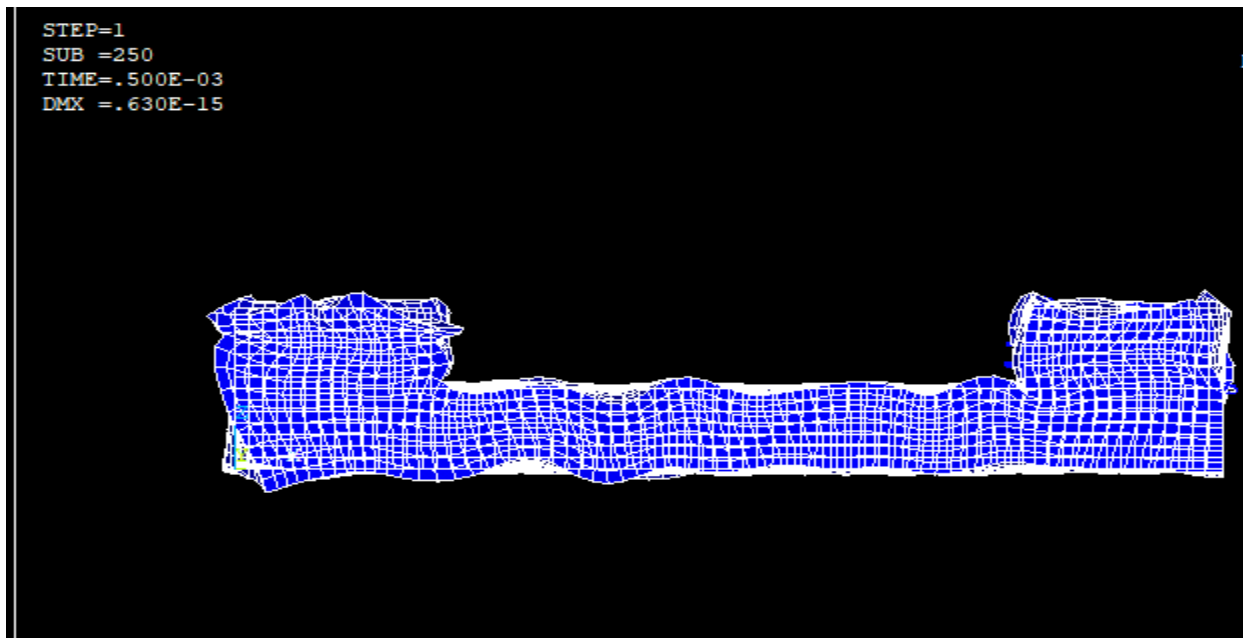


Figure 4.7 - Damaged plate deformation at the end of the simulation

#### 4.2.2 Electrical Potential output

The electric potential outputs follow the same trends as the deformation outputs in the previous section. There is a higher voltage at the actuator compared to the sensors, as a result of a voltage drop across the model for all sets of results.

The electric potential difference between the healthy and damaged plate models is too subtle to be noticed within the first two data sets. The last data set for the damaged model displays a relatively large amount of warping near the actuator than the sensors compared to the healthy model which exhibits almost uniform deformation. This can be attributed to the presence of the damage which causes an interruption in the wave propagation, resulting in more deformations near the point of origin (actuator) than the destination (sensors). This phenomenon results in lower voltages being recorded by the sensors for the damaged model. Figures 26 to 31 illustrate the electric potential outputs.

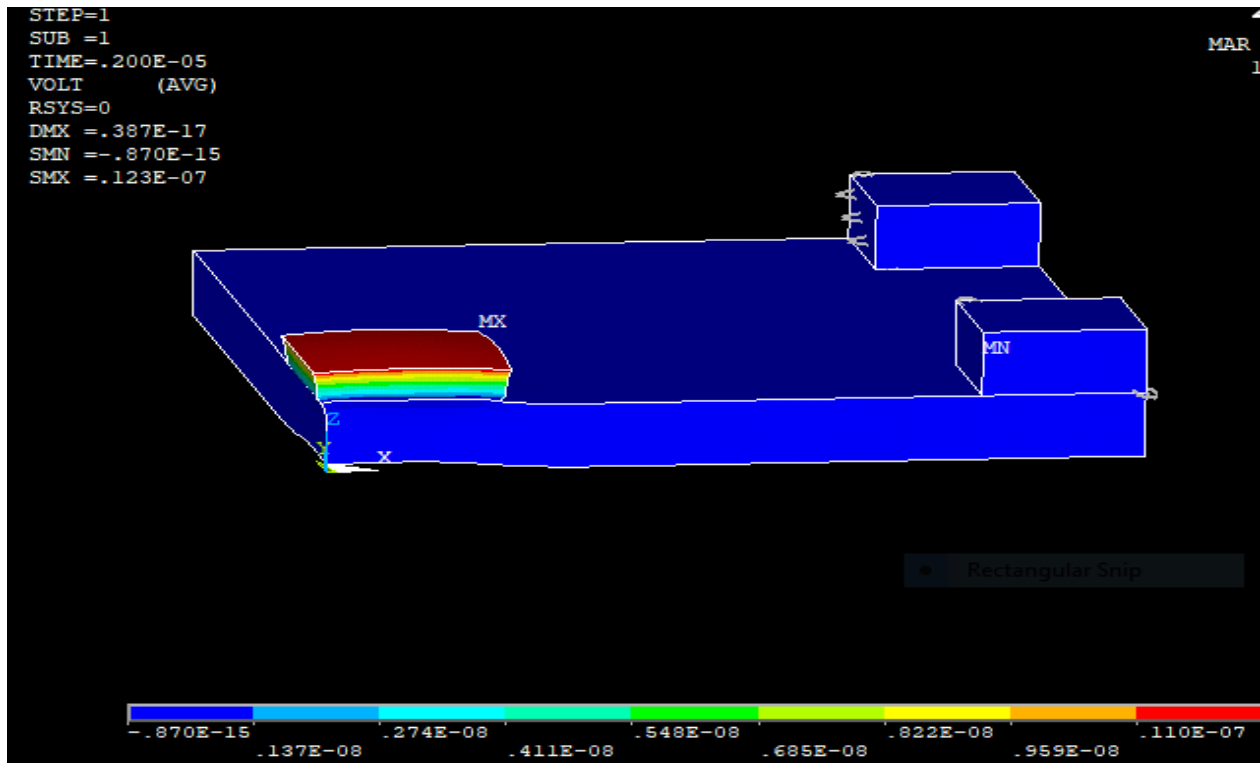


Figure 4.8 - Healthy plate electric potential output at the beginning of the simulation

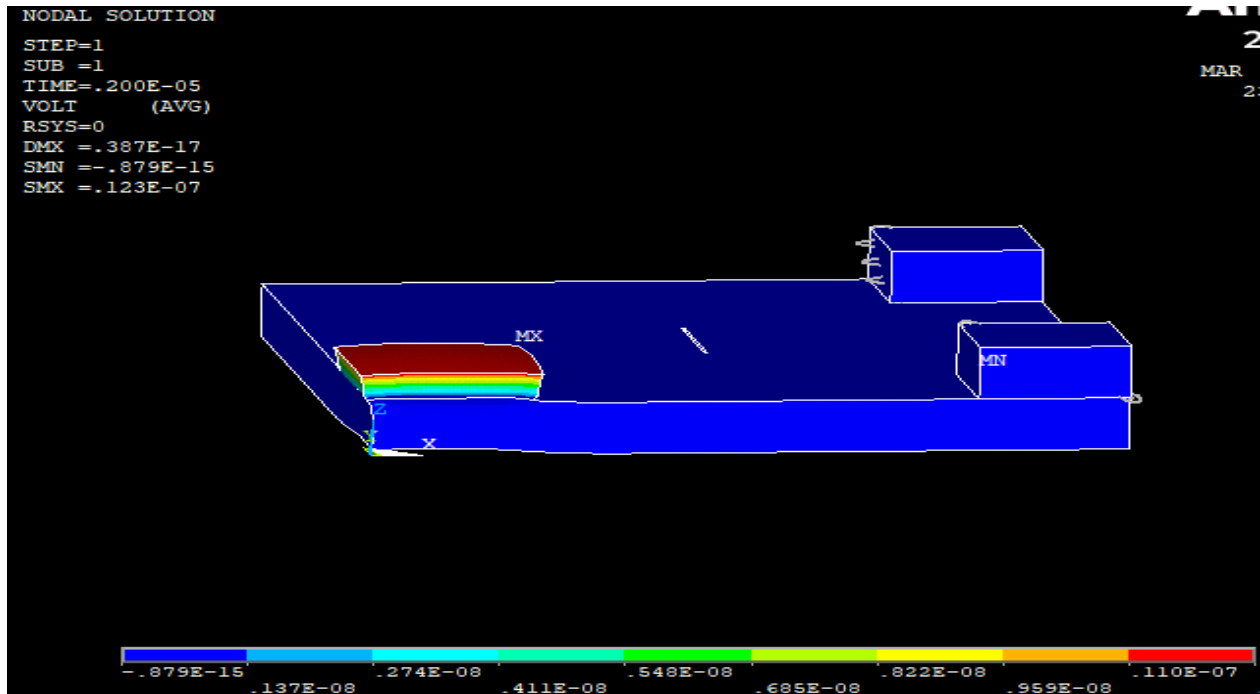


Figure 4.9 - Damaged plate electric potential output at the beginning of the simulation

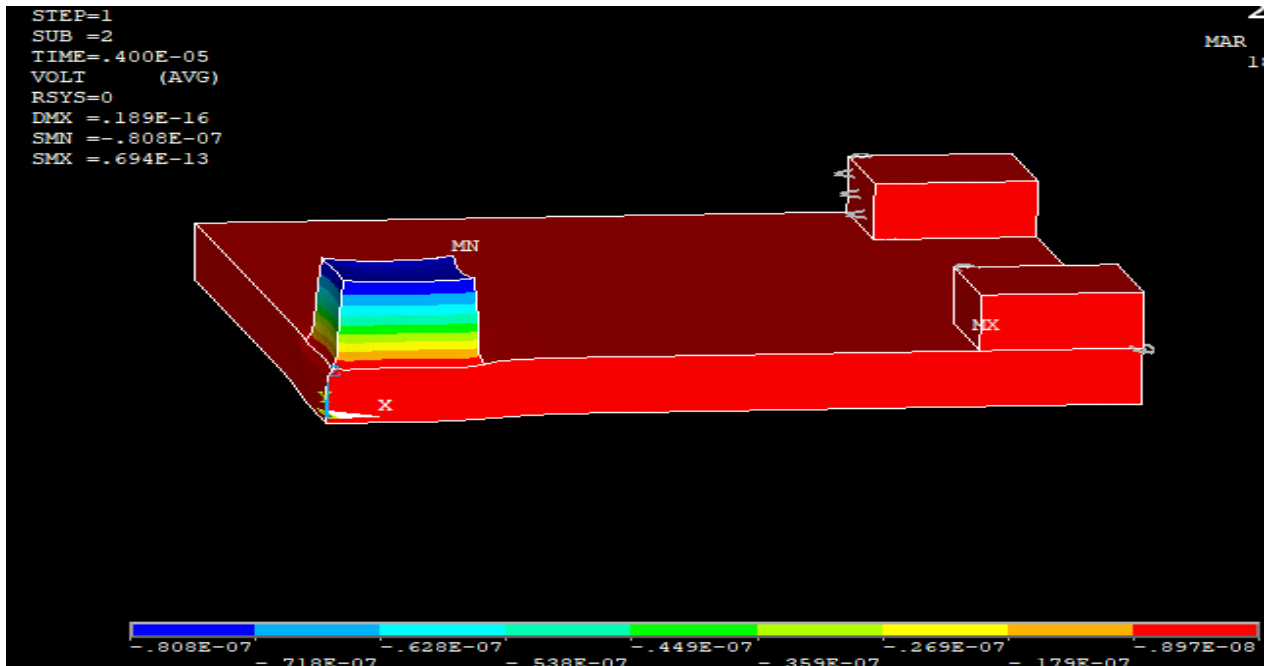


Figure 4.10 - Healthy plate electric potential output in the middle of the simulation

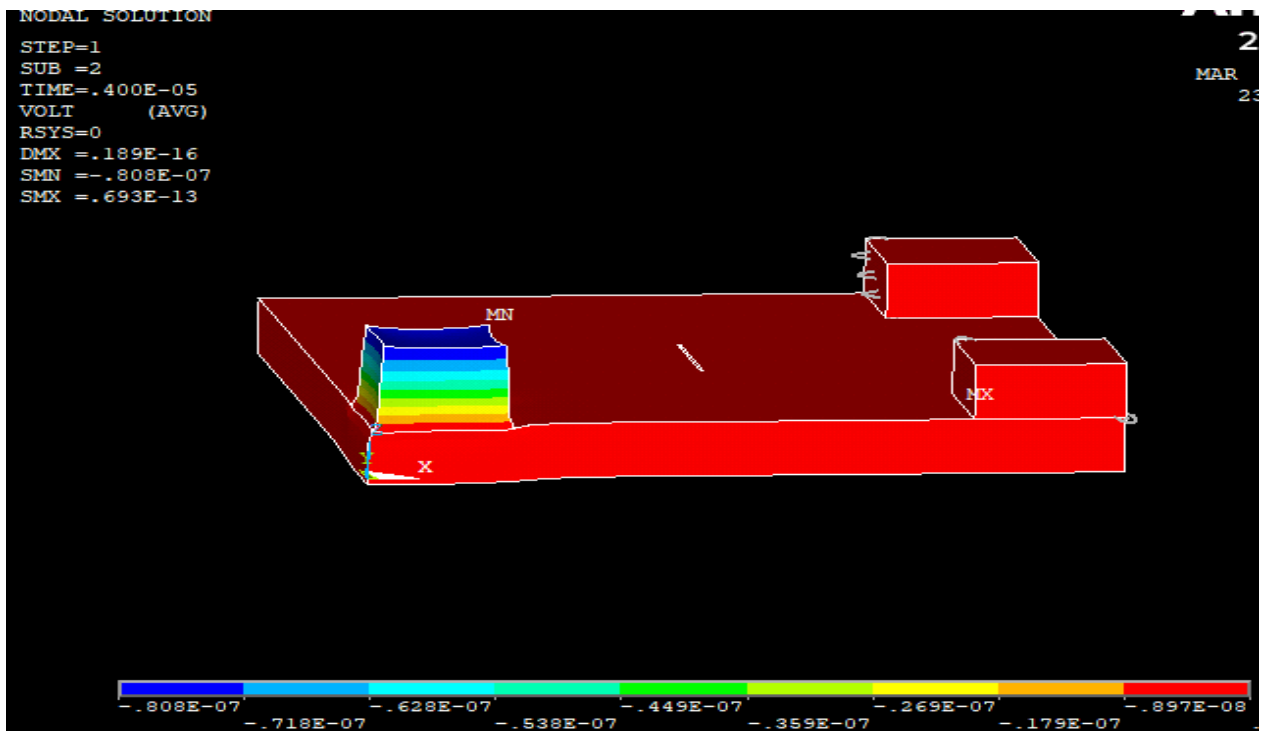


Figure 4.11 - Damaged plate electric potential in the middle of the simulation

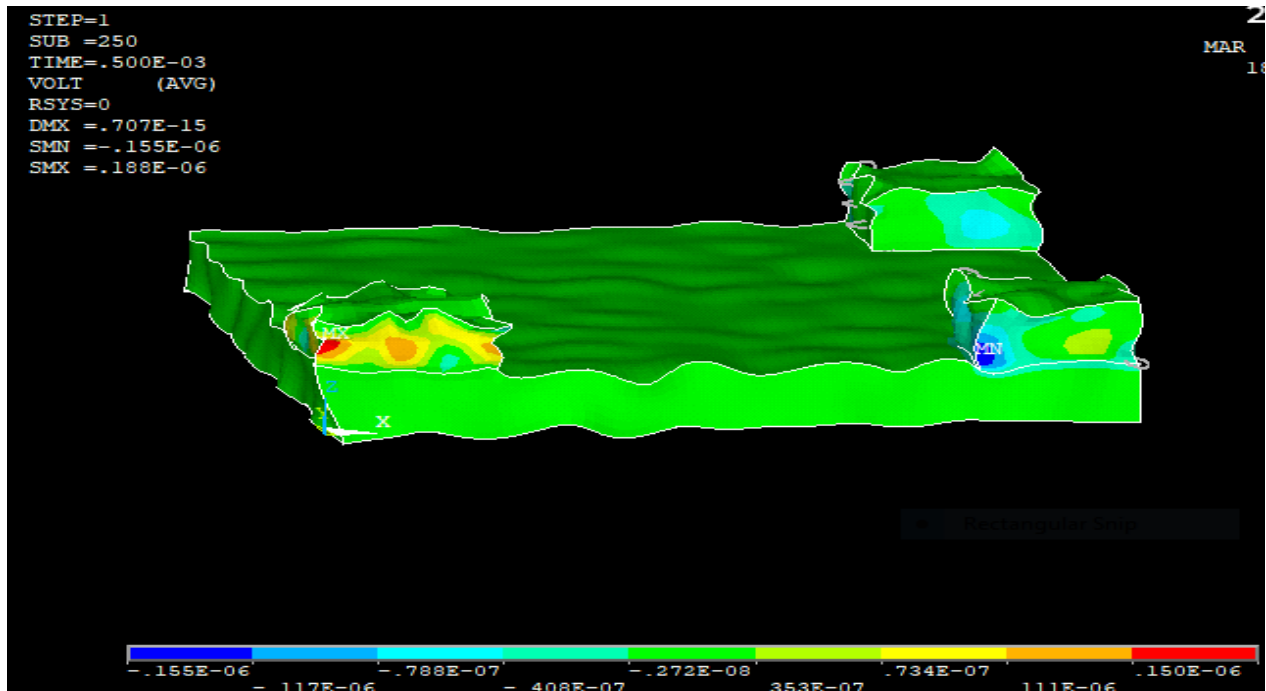


Figure 4.12 - Healthy plate electric potential output at the end of the simulation

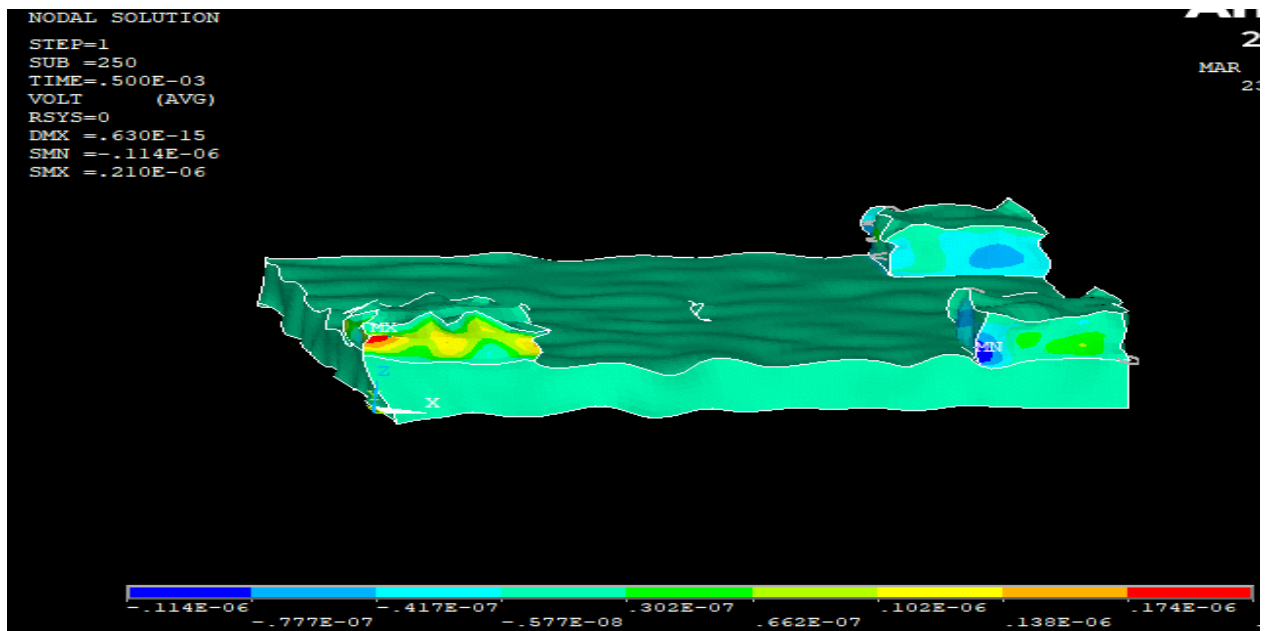


Figure 4.13 - Damaged plate electric potential output at the end of the simulation

### 4.2.3 Nodal Electric potential output results

The Nodal electrical potential output results highlight the differences between the healthy and damaged plates. As expected, the difference is very small during the beginning phase of the simulation due to the relatively smaller load values. There is a significant difference towards the tail end of the simulation, as a result of the high load values that make the contrast clear. It can be observed from the difference in outputs that the damaged plate has lower outputs generally compared to the healthy plate. This is to be expected, as the presence of the damage disrupts the wave propagation, resulting in loss of velocity and hence reduced output. Figures 32 to 35 illustrate the difference in nodal electric potential output between the healthy plate and the damaged plate for both modeled sensors.

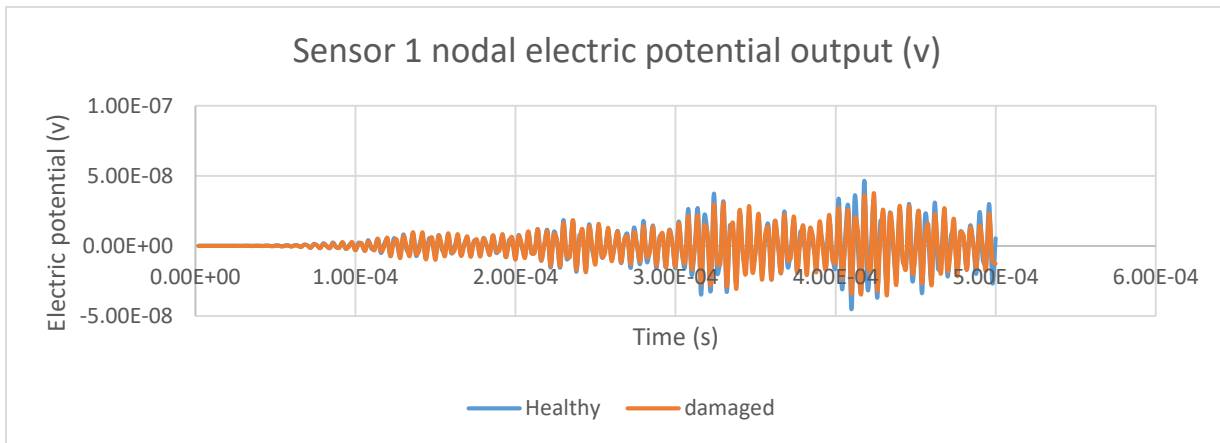


Figure 4.14 - Nodal electric potential output from sensor 1 in both healthy and damaged plate

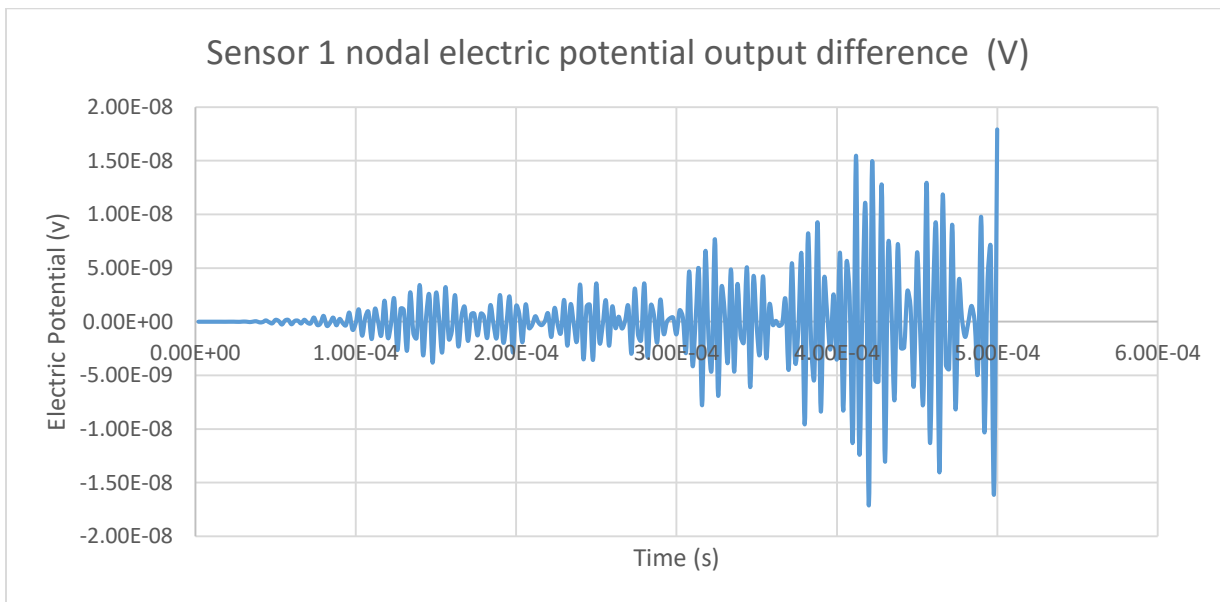


Figure 4.15 - Nodal electric potential output differences between healthy and damaged plates. Data obtained from sensor 1

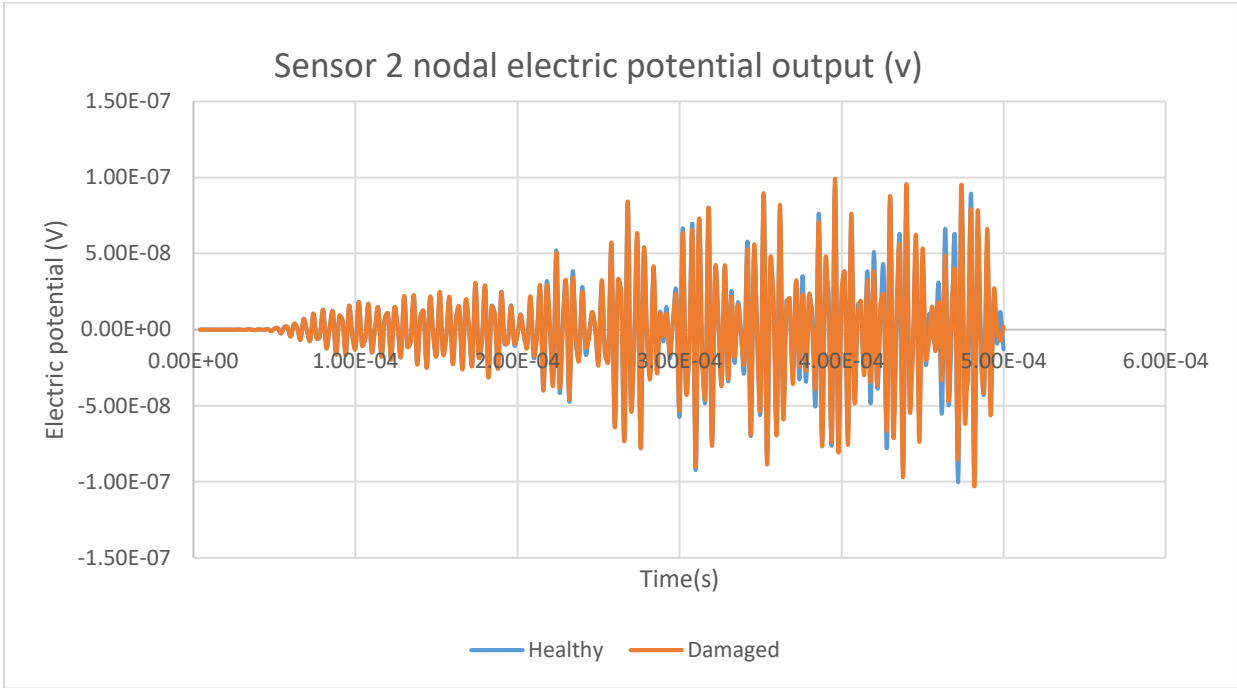


Figure 4.16 - Nodal electric potential output from sensor 2 in both healthy and damaged plate

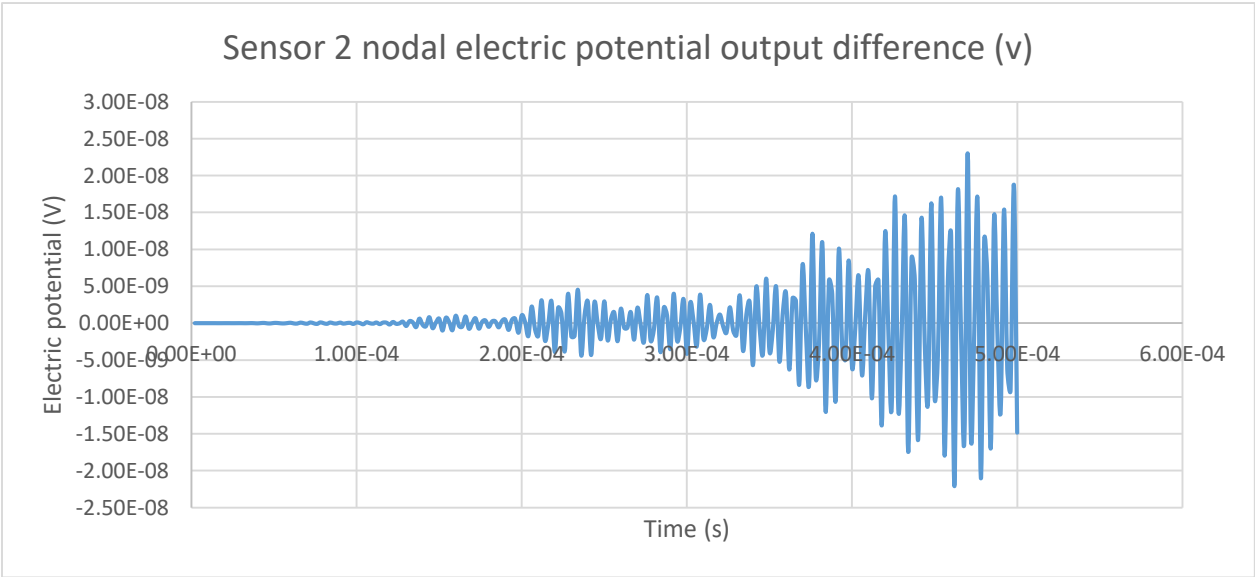


Figure 4.17 - Nodal electric potential output differences between healthy and damaged plates. Data obtained from sensor 2

## 5. Chapter 5 – Damage Location

Following the nodal electric potential outputs obtained in chapter 4, chapter 5 establishes the identified damage locations. This chapter discusses electric potential output results analysis using the Matlab wavelet toolbox, the identification of arrival times, plotting of the geodesics and eventually location of damage locations, and how they compare to the modeled damage locations.

### 5.1 Signal Denoising

The signal output obtained from the sensors in the previous chapter contains a lot of noise, which makes it difficult to visualize the arrival times of huge spikes of voltages occurring over a small time window. To better derive these arrival times, signal denoising is applied to the sensor outputs.

Signal denoising is defined as the removal of unwanted information from a signal while preserving useful features [26]. This is done by applying select wavelets and thresholds, from which coefficients of the denoised signal are calculated [26]. To achieve the objective of having clearly defined arrival times of high amplitude voltage, it is necessary to penalize low amplitude voltage. This leaves the signal with fewer details, consisting of high amplitude outputs.

A Daubechies Db5 is applied in the decomposition process, followed by a soft fixed form threshold [27]. The Db5 is selected due to the energy-preserving characteristics of orthogonal wavelets when applied in signal Denoising [27]. Additionally, the db5 oscillations provided a good estimate of the original signal used in the simulation and therefore ensured the preservation of important aspects of the original signal. The choice of a fixed form threshold is informed by how much low amplitude data, which is treated as noise too, needed to be penalized. The ratio of these data to the high amplitude data is small and thus makes the fixed form threshold scale the suitable choice [27]. The selection of whether to apply soft or hard denoising is quite clear, since hard denoising eliminates even important aspects of the signal, soft denoising becomes the default choice [27].

Two sets of data are analyzed using the Matlab wavelet packet and the Matlab continuous wavelet graphical user interfaces. Each set of data represents sensor outputs from a modeled damage simulation. Set 1 has output data from sensors 1 and 2 respectively. Set 2 correspondingly has data from sensors 1 and 2 also. The input data to the Matlab wavelet packet graphical user interface consists of amplitude data obtained from the sensors. This is coupled with the data length to create a 2d plot of the input signal. The output signal similarly has coupled voltage and position data. The position data corresponds to an amplitude and time location and can therefore be used to map the signal in the voltage-time domain again. Figures 36 to 39 show the output denoised signals together with the original signals. It is evident that a lot of low amplitude signal, which consists mostly of noise, is penalized in the denoised signal. This leaves behind mostly high amplitude signals which correspond to large discrepancies in signals between data from a healthy plate and that from a damaged plate. Additionally, it can be seen that there is a very small variation between figures 36 and 37, as opposed to the large variation between figures 38 and 39. This is a result of the damage being almost equidistant between the two sensor data in figures 36 and 37 while being skewed in the last couple of sensors.

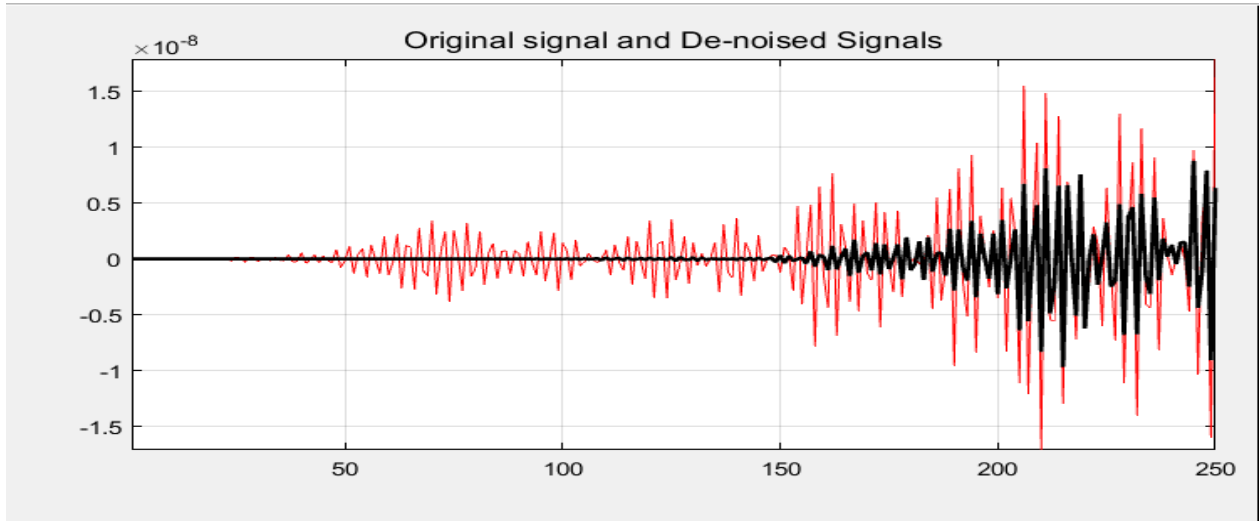


Figure 5.1 - Denoised (black) and original (red) data from sensor 1 during the first damaged plate simulation.

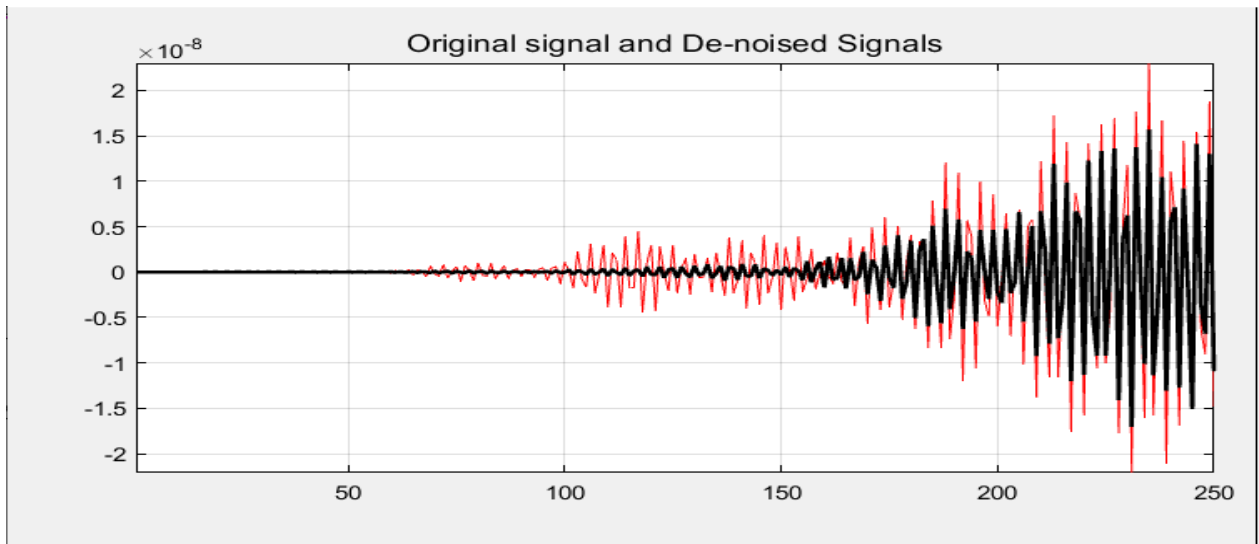


Figure 5.2 - Denoised (black) and original (red) data from sensor 2 during the first damaged plate simulation.

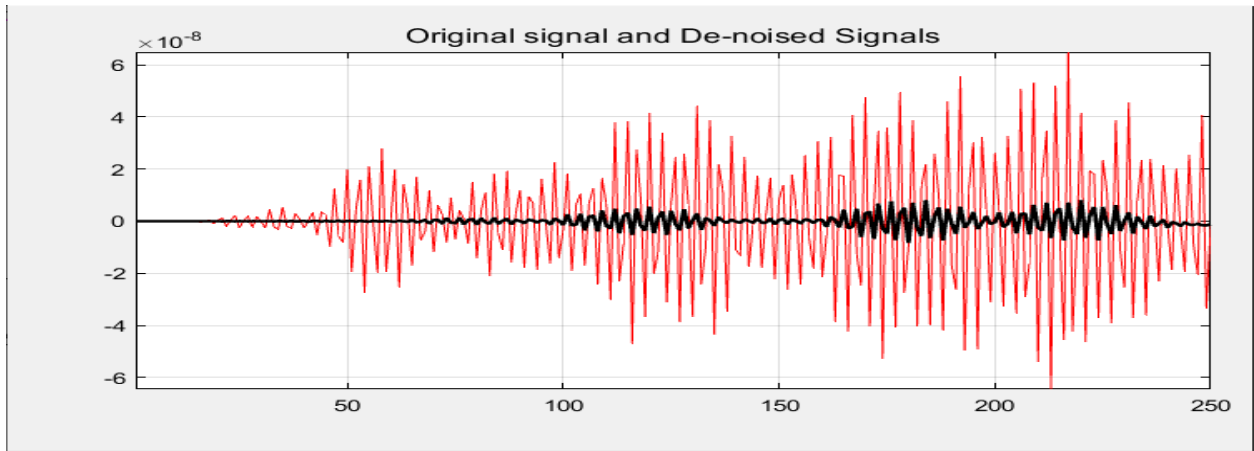


Figure 5.3 - Denoised (black) and original (red) data from sensor 1 during the second damaged plate simulation.

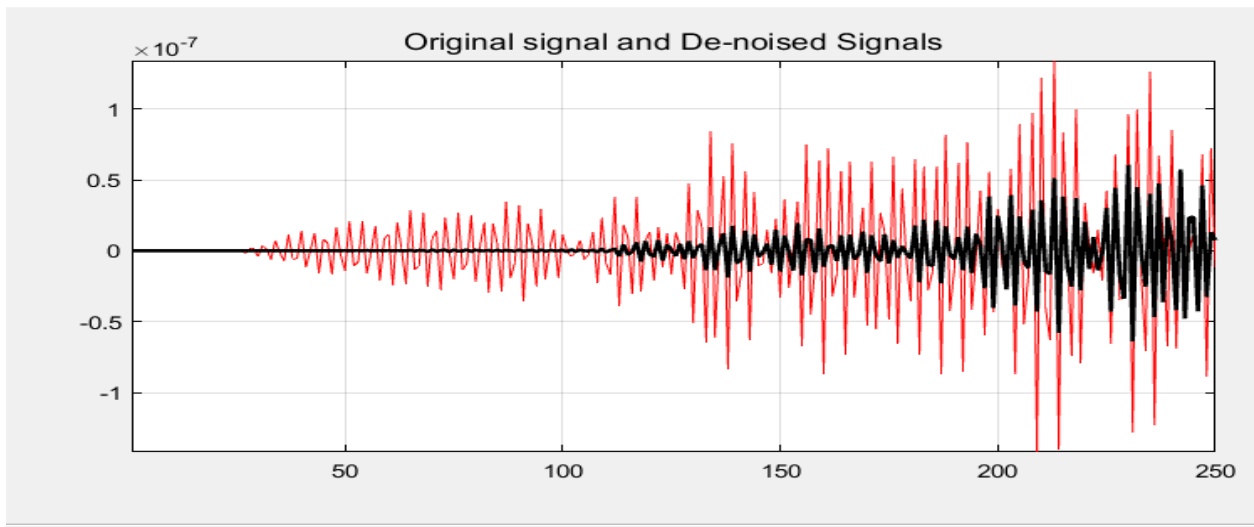


Figure 5.4 - Denoised (black) and original (red) data from sensor 2 during the second damaged plate simulation.

## 5.2 Arrival times

Based on the denoised signal acquired in the previous step, a 1-D continuous wavelet is applied to obtain a spectrogram, which allows visualization of the arrival of high amplitude signals. The spectrogram analysis is done using similar wavelets as the decomposition. While the usual choice would be to use a Morlet wavelet, with a Gaussian window for spectrogram analysis, since they are based on continuous wavelet transforms, a choice is made to use a Db5 wavelet again. This is due to the smoothing effect of the Db5 wavelet, which gets rid of small transients at peaks that would otherwise cloud the spectrogram. The analyzed data still retains the high-frequency peaks, regardless of the harsh penalties imposed by the Db5 wavelet. A sampling frequency of 204 kHz is used in the analysis. This frequency is similar to the original signal sampling frequency. The scaling for the outputs is left as Matlab default, although significantly larger than what is needed, it allows better visualization of high amplitude areas, unlike when the scale is restricted to 5. The focus on the output results will however be restricted to scales under 5.

Figures 40 to 44 depict the output results of the continuous wavelet analysis. The figures contain an analyzed signal plot, data samples, a spectrogram, and a spectrogram coefficients plot. The focus of this project is the spectrogram output. The spectrogram highlights high amplitude areas using high-density shades as indicated by the color scale. Using data from the spectrogram/coefficient plot, high amplitude arrival positions are obtained. The high amplitude positions are highlighted using blue cones. This then corresponds to the time-voltage data, and subsequent arrival times obtained as shown in figure 41 and table 14. A look at figures 40 and 42 show very few discrepancies. Darker shades occur at almost similar positions in both spectrograms as expected. This is a result of the damage location being equidistant between the two sensors, thus almost disrupting the damage signal in almost equal magnitude. Figures 43 and 44 however, show a large discrepancy as expected, with sensor 2 experiencing early onset perturbations than sensor 1, despite the well-contrasted disturbances in sensor 1. The earlier perturbations in sensor 2 are a result of its proximity to the damage, as well as its position, where most signals have to incur the damage first before registering.

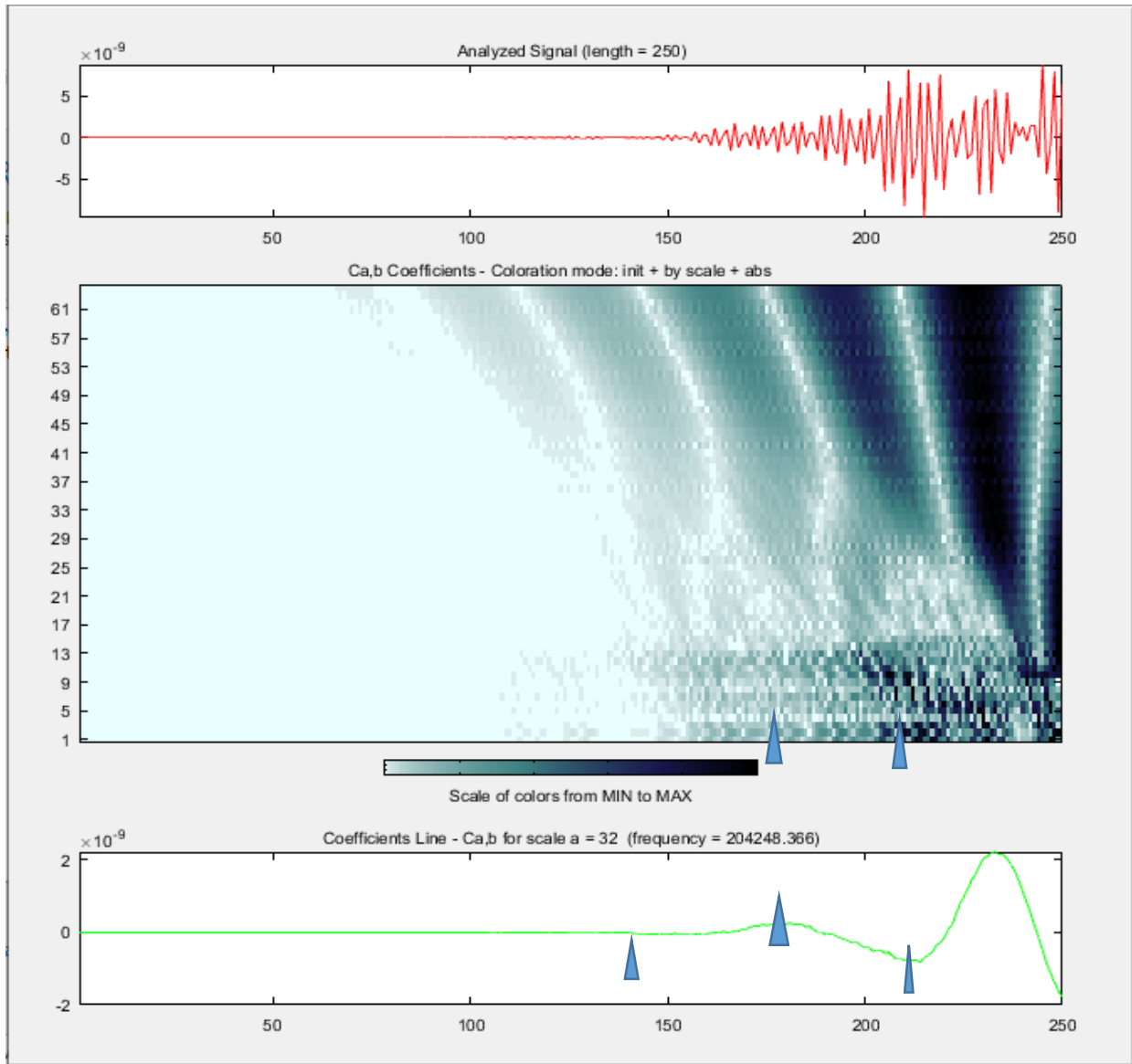


Figure 5.5 - Wavelet analysis output showing spectrogram corresponding to signal difference from sensor 1 simulation 1. Blue cones indicate positions of abrupt amplitude change, signifying large contrast between healthy and damaged plate signals.

140	2.78E-04	5.04E-08	5.27E-08
141	2.80E-04	-7.26E-09	-6.41E-09
142	2.82E-04	-2.78E-08	-3.13E-08
143	2.84E-04	3.78E-08	4.17E-08
144	2.86E-04	-2.64E-08	-2.84E-08
145	2.88E-04	1.15E-08	1.05E-08
146	2.90E-04	-7.76E-09	-4.26E-09
147	2.92E-04	1.47E-08	1.07E-08
148	2.94E-04	-1.87E-08	-1.64E-08
149	2.96E-04	5.89E-09	6.48E-09
150	2.98E-04	2.48E-08	2.16E-08
151	3.00E-04	-5.69E-08	-5.28E-08
152	3.02E-04	6.66E-08	6.39E-08
153	3.04E-04	-4.02E-08	-4.04E-08
173	3.44E-04	-6.99E-08	-6.93E-08
174	3.46E-04	5.07E-08	5.49E-08
175	3.48E-04	-2.46E-09	-8.51E-09
176	3.50E-04	-5.36E-08	-4.98E-08
177	3.52E-04	8.87E-08	8.97E-08
178	3.54E-04	-8.34E-08	-8.84E-08
179	3.56E-04	3.97E-08	4.49E-08
180	3.58E-04	1.96E-08	1.84E-08
181	3.60E-04	-6.47E-08	-6.88E-08
182	3.62E-04	7.59E-08	8.22E-08
183	3.64E-04	-5.45E-08	-5.79E-08
184	3.66E-04	1.84E-08	1.54E-08
185	3.68E-04	1.22E-08	2.05E-08
208	4.14E-04	-2.50E-08	-3.00E-08
209	4.16E-04	3.81E-08	3.23E-08
210	4.18E-04	-4.85E-08	-3.47E-08
211	4.20E-04	5.10E-08	3.88E-08
212	4.22E-04	-3.77E-08	-3.64E-08
213	4.24E-04	4.89E-09	1.64E-08
214	4.26E-04	4.00E-08	2.28E-08
215	4.28E-04	-7.77E-08	-6.60E-08
216	4.30E-04	8.62E-08	8.79E-08
217	4.32E-04	-5.58E-08	-7.01E-08
218	4.34E-04	-2.36E-09	1.51E-08
219	4.36E-04	6.07E-08	5.20E-08
220	4.38E-04	-9.08E-08	-9.68E-08
221	4.40E-04	7.97E-08	9.55E-08
222	4.42E-04	-3.59E-08	-5.00E-08

Figure 5.6 - Sampled data images showing position, arrival times, healthy plate voltage, and damaged plate voltage respectively at positions 140,175, and 210.

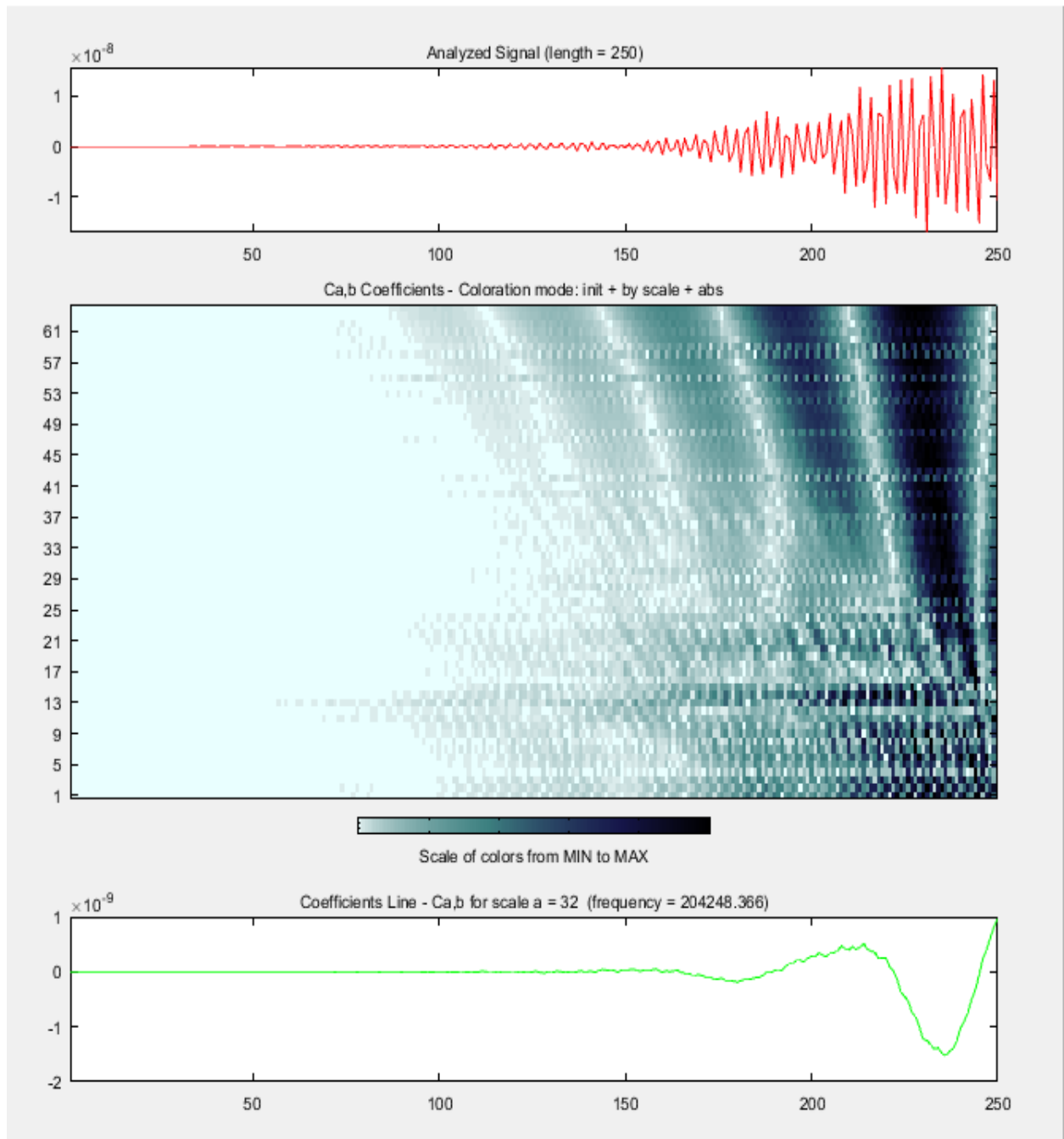


Figure 5.7 - Wavelet analysis output showing spectrogram corresponding to signal difference from sensor 2 in simulation 1

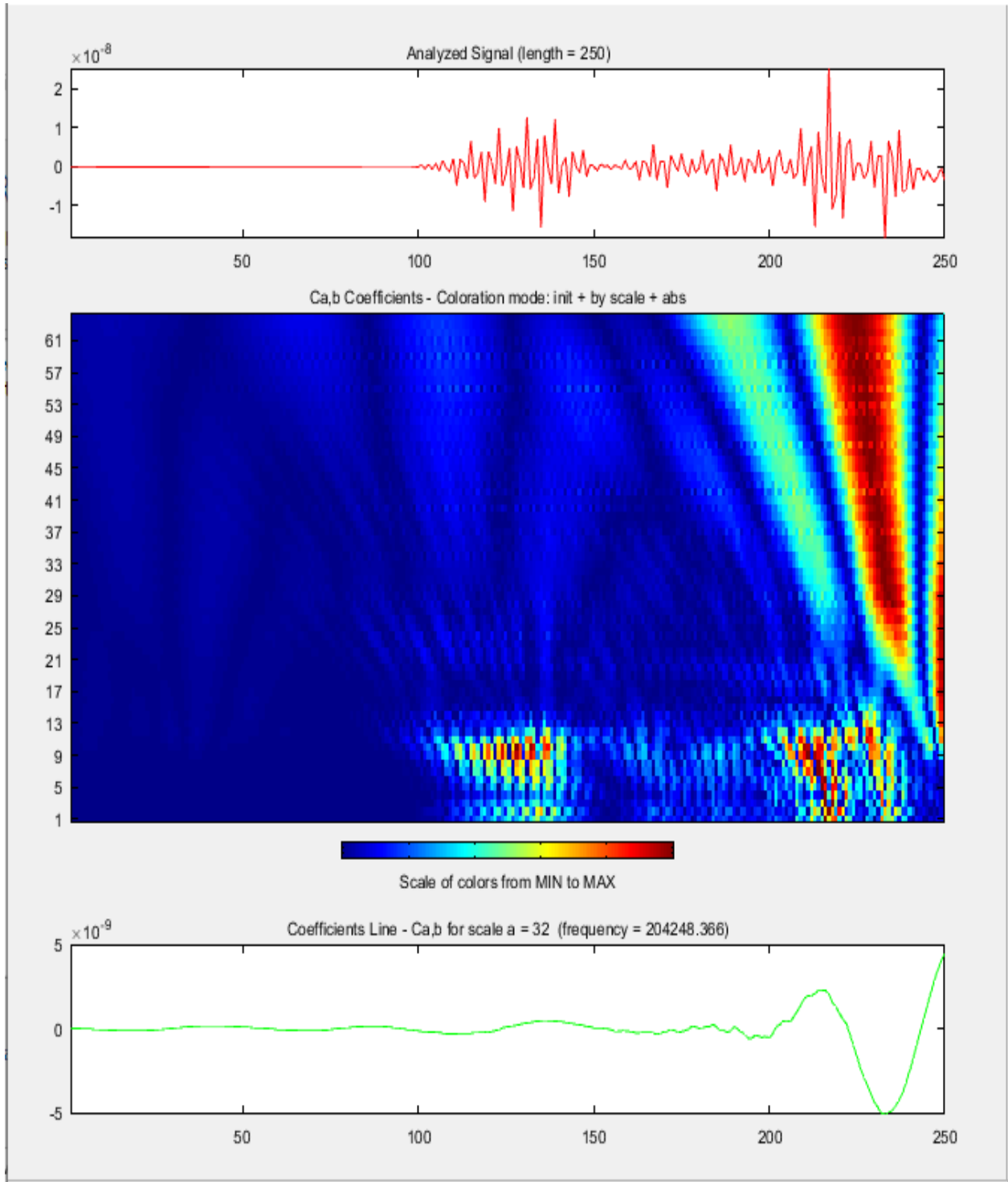


Figure 5.8 - Wavelet analysis output showing spectrogram corresponding to signal difference from sensor 1 in simulation 2

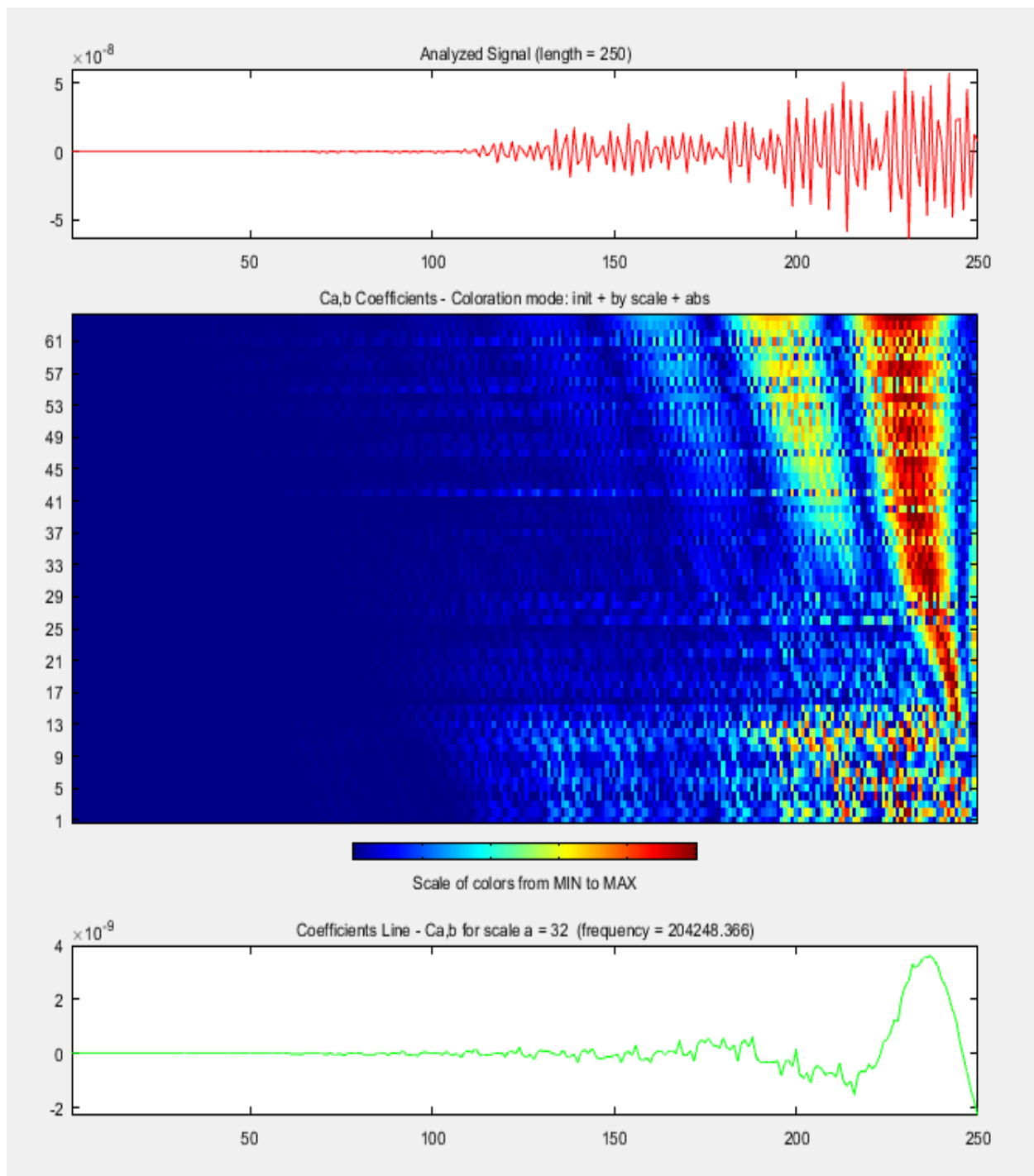


Figure 5.9 - Wavelet analysis output showing spectrogram corresponding to signal difference from sensor 2 in simulation 2

Table 5.1 - Arrival times corresponding to spectrogram positions

Entity	Arrival time number	Position	Corresponding time [s] * 10 <sup>-4</sup>
Damage 1 sensor 1	T1	140	2.78
	T2	175	3.48
	T3	210	3.98
Damage 1 sensor 2	T1	140	2.78
	T2	175	3.48
	T3	210	3.98
Damage 2 sensor 1	T1	125	2.48
	T2	148	2.94
Damage 2 sensor 2	T1	105	2.08
	T2	205	4.08

### 5.3 Damage Geodesics

Once the corresponding arrival times have been located, the damage geodesics are calculated using the waves' speed and arrival time. The wave's speed is determined using the frequency and wavelengths of the outputs. The radial geodesics are then obtained by multiplying the speed and arrival times as discussed in chapter 2. The results of these calculations are displayed in table 15.

Table 5.2 - calculated geodesics from arrival times

Wavelength (m)	Frequency (Hz)	Speed (m/s)	Damage & sensor number	Time number	Time [s] *E-4	Distance [m]*E-2
3E-5	2E6	6.12E1	1,1	T1	2.78	1.7
				T2	3.48	2.13
				T3	3.98	2.44
			1,2	T1	2.78	1.7
				T2	3.48	2.13
				T3	3.98	2.44
			2,1	T1	2.48	1.52
				T2	2.94	1.8
			2,2	T1	2.08	1.27
T1	4.08	2.50				

After obtaining the geodesic distances, the geodesics are plotted/applied to the geodesics formula to locate the identified approximate locations of the damage. In plotting the geodesics, the shortest distances from the actuator to the sensors are selected. For sensor 2, the location is one definite point, occurring at the corner of the sensor. However, for sensor 1, an

arbitrary position is chosen along the Y length of the sensor. Varying center locations slightly vary the accuracy of the located damage. Figure 45 illustrates an example chosen location. An analysis of how this variation affects the results will be explored in detail in the next chapter.

Figures 45 to 48 depict damaged plate models, sensors, actuators, corresponding modeled damages, corresponding geodesic plots, and corresponding identified damage locations. The geodesics and located damages are plotted in green. Figures 45 to 47 correspond to geodesics plotted using data derived from the first simulation of a damaged plate, in which the damage is modeled at equidistant locations between the sensors. As expected, the geodesics intersections map an area close to the middle of the modeled damage, due to the almost equal distance that delayed waves have to propagate from the damage to the sensors.

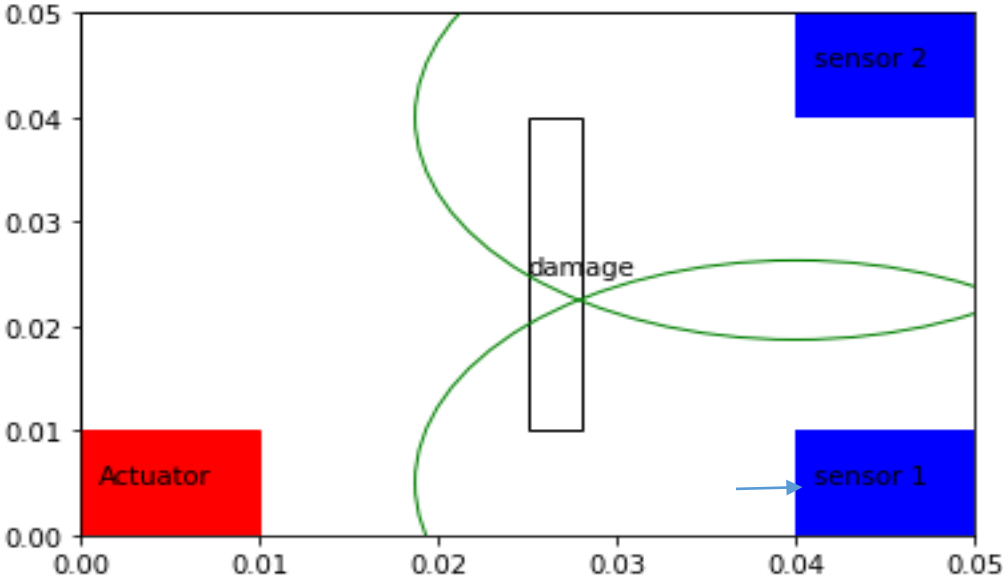


Figure 5.10 - First set of geodesic plots from simulation 1, where the modeled damage is centered from plate edges in the y-direction. Arrow indicates arbitrarily chosen center position of geodesic on sensor 1 (center location on sensor 1's Y edge).

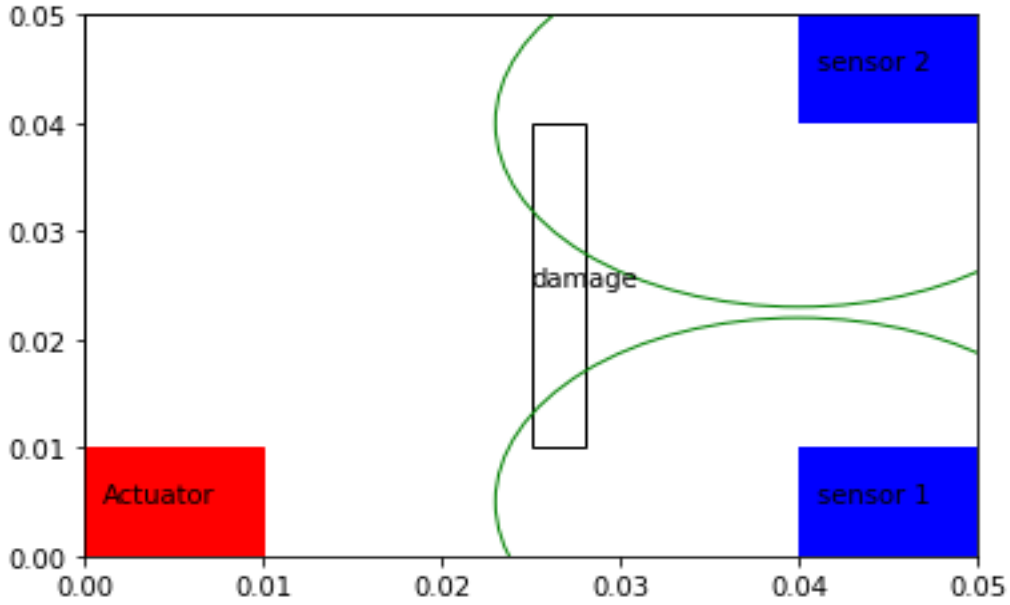


Figure 5.11 - Second set of geodesic plots from simulation 1, where the modeled damage is centered from plate edges in the y-direction.

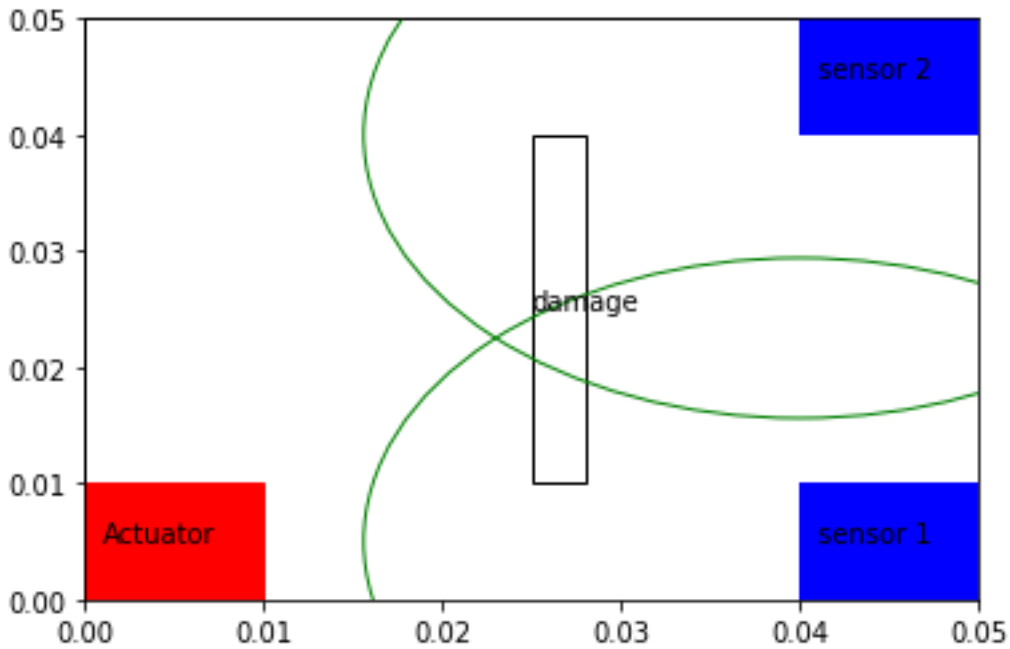


Figure 5.12 - Third set of geodesic plots from simulation 1, where the modeled damage is centered from plate edges in the y-direction.

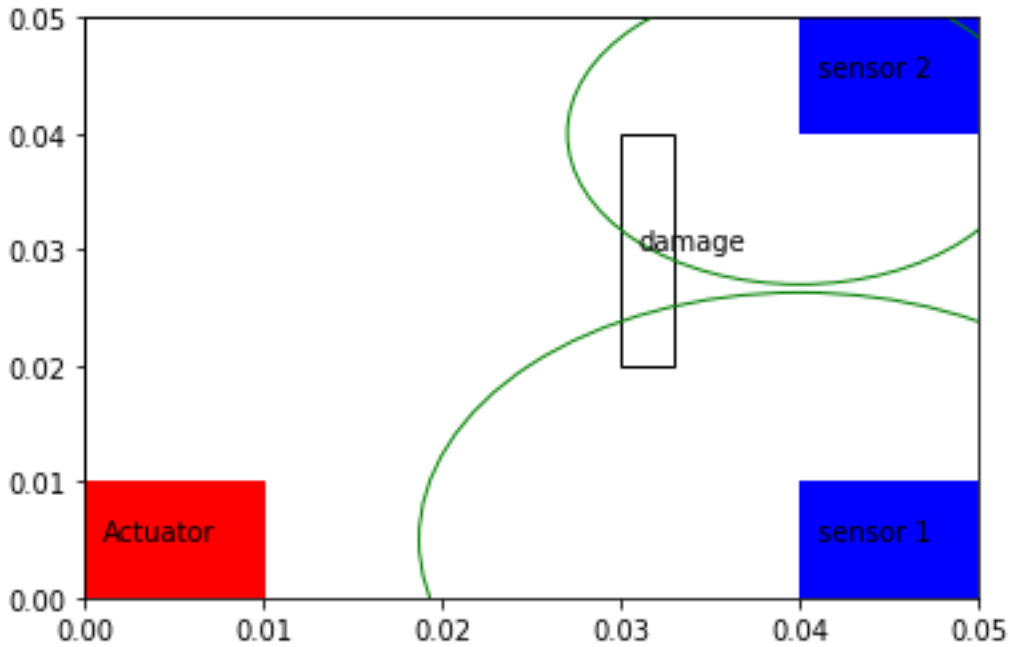


Figure 5.13 - First set of geodesic plots from simulation 2, where the modeled damage is skewed towards sensor 2.

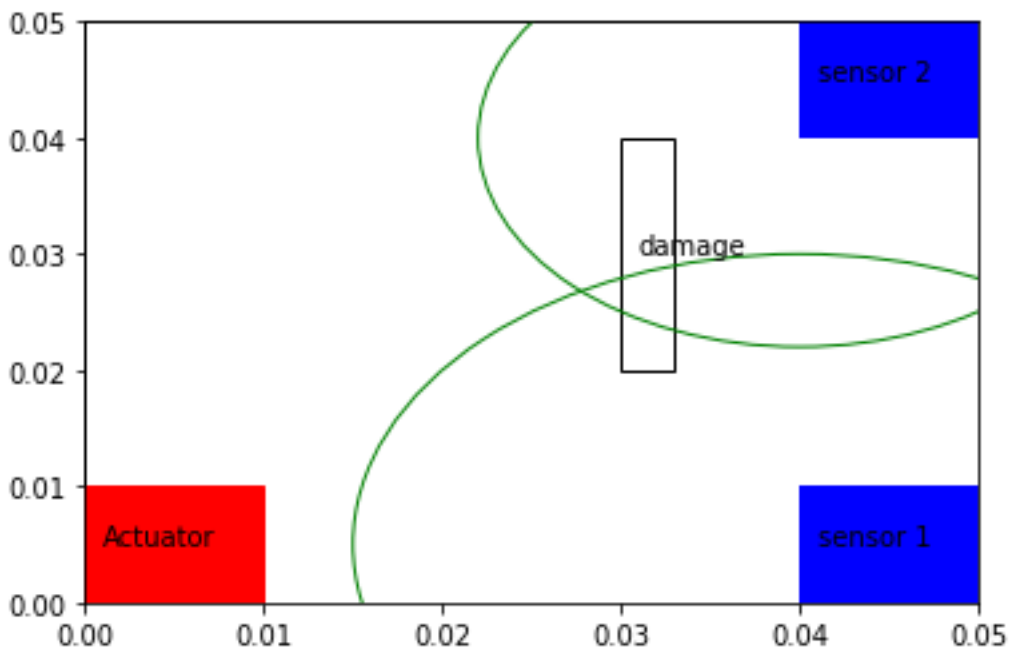


Figure 5.14 - Second set of geodesic plots from simulation 2, where the modeled damage is skewed towards sensor 2

## 5.4 Damage locations and comparison

The identified damage locations correspond to the mapping of the intersections of the geodesics. The final damage area is arrived at by connecting the three intersections in figures 45-46-47 on one plot with straight lines. The area circumscribed by the lines represents the region that falls within the likely identified damage. This region is depicted by the triangle in figure 50. This is a good damage identification since most of the area falls within the modeled damaged area.

Due to the central location of the modeled damage, it is expected that accurate identification of the damage would be favorably towards the center in the first simulation. As expected simulation 1 identified location is more centered compared to simulation 2 where the location skews towards sensor 2 as shown in figures 50 and 51 respectively. While the identified locations provide good tracking of the approximate position, they don't depict the scope or shape of the damage as illustrated in figures 50 and 51. They, however, provide a good starting point as evident from the aluminum plate simulation. Further analysis and variation of geodesic center locations may provide results.

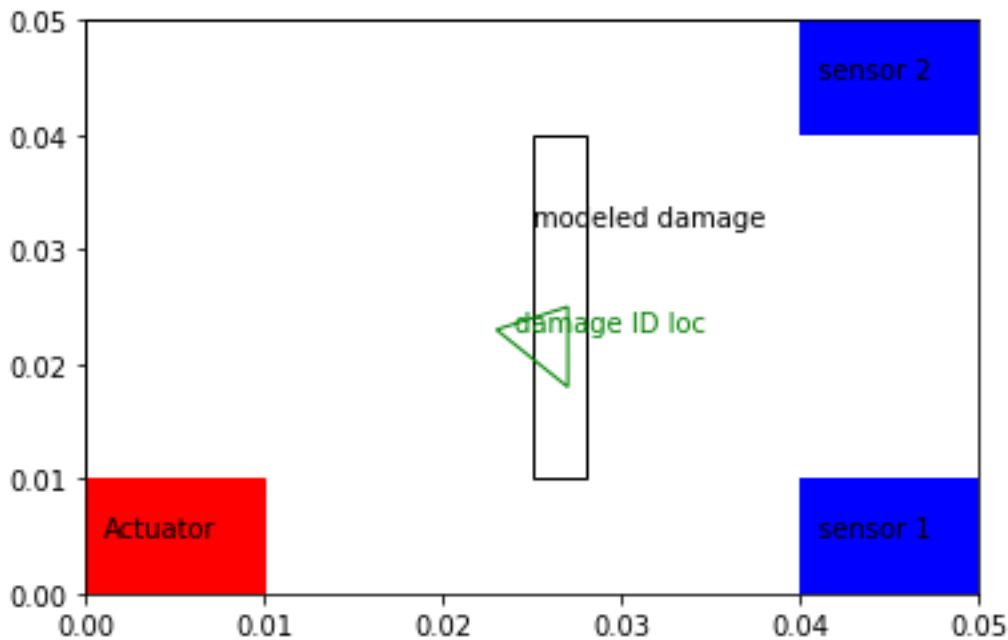


Figure 5.15 - Aluminum plate showing identified damage location from simulation with centered modeled damage.

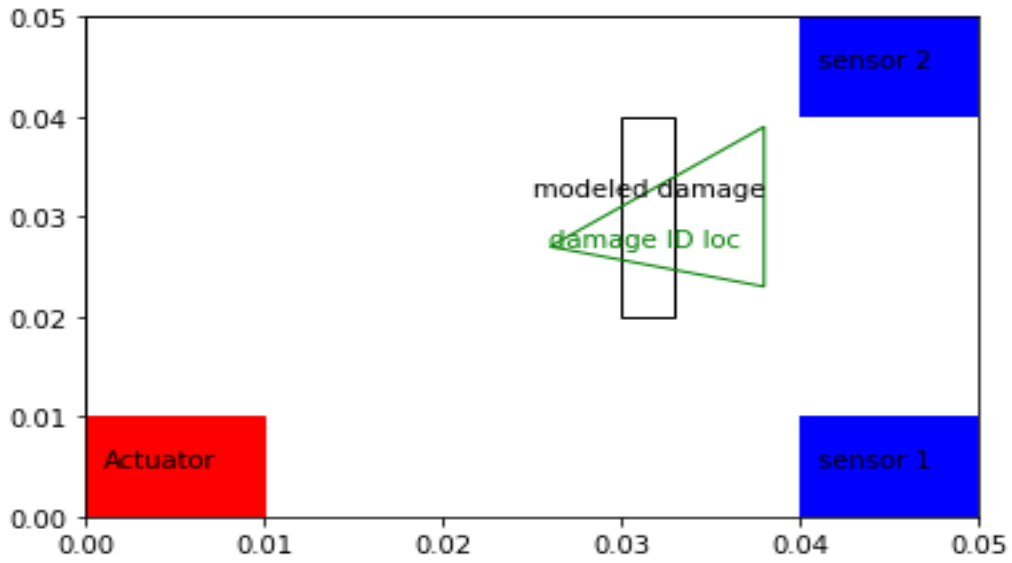


Figure 5.16 - aluminum plate showing identified damage location from simulation with un-centered modeled damage.

## 6. Chapter 6 – Composite plate

Building on the principles applied in chapters 4 and 5 on the aluminum plate to obtain approximate damage locations of a modeled damage, this chapter applies the same principles to a composite plate. The chapter involves defining a composite plate setup, material properties, simulation model setup, simulation results, and analysis of the results.

### 6.1 Model setup

The composite plate is modeled using thin layers of two different fibers, woven carbon fiber, and unidirectional fiber. The fibers are stacked up in successive layers, with the orientation of each layer being at a 45-degree angle to the previous layer as illustrated in figure 52. The layer sequence  $[0, +45, 90, -45, 0]$  allows the meshed fibers to better handle loads applied from different angles. This is a result of the loads encountering longitudinal fiber orientations in this arrangement, as opposed to the matrix in lateral directions or diagonal directions in some woven fibers.

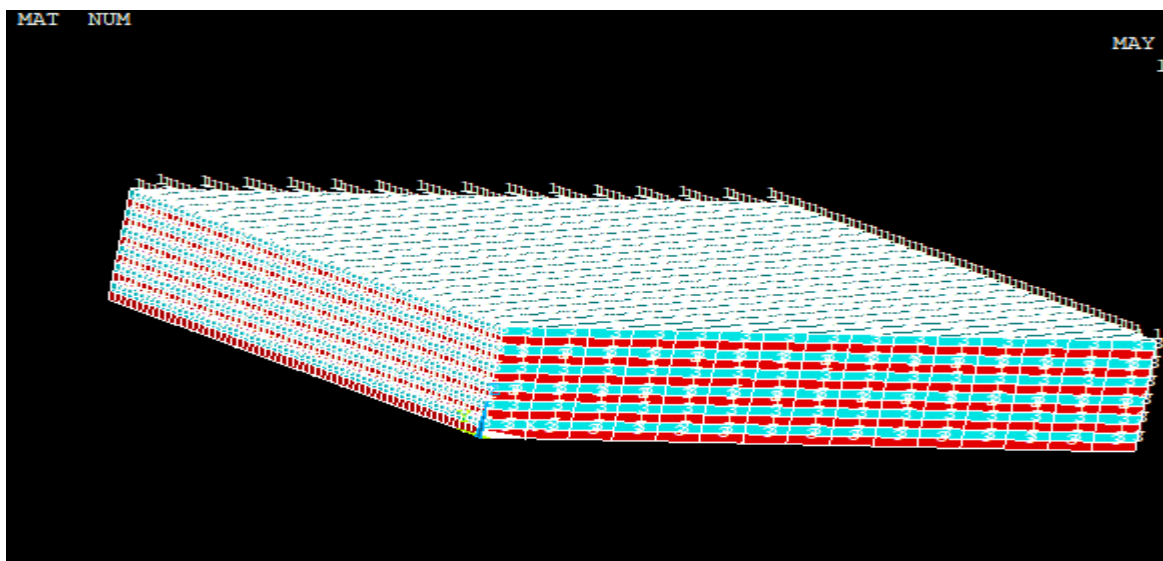


Figure 6.1 - Model carbon composite plate layers. Different colors depict different material properties.

Thus, the plate is composed of layers of interlaced fibers forming a woven composite fiber. The choice for this kind of layup stems from the beneficial mechanical properties that woven composite fibers possess over their unidirectional counterparts. Interlacing the fibers, together with a resin matrix, results in composite parts with better rigidity, strength, and dimensional stability than parts made of unidirectional layers only. The plate is composed of five layers, two different materials, and one element. Different material properties are assigned to each layer in the laminate. The material properties utilized in the layers are highlighted in table 15.

Table 6.1: Composite plate material properties [28]

Material	Material property	Symbol	Magnitude	Unit
Epoxy-carbon woven wet	Density		1451	Kg/m <sup>3</sup>
	Young's modulus	E1	5.916E10	Pa
		E2	5.916E10	Pa
		E3	7.5E9	Pa
	Poisson ratio	PXY	0.04	-
		PYZ	0.3	-
		PXZ	0.3	-
	Shear Modulus	GXY	3.3E9	Pa
		GYZ	2.7E9	Pa
		GXZ	2.7E9	Pa
Epoxy-carbon UD wet	Density		1518	Kg/m <sup>3</sup>
	Young's modulus	E1	1.2334E11	Pa
		E2	7.78E9	Pa
		E3	7.78E9	Pa
	Poisons ratio	PXY	0.27	-
		PYZ	0.42	-
		PXZ	0.27	-
	Shear modulus	GXY	5E9	Pa
		GYZ	3.08E9	Pa
		GXZ	5E9	Pa

For the element choice, Solid shell elements are selected to model the layers of the composite laminate. The suitability for this role stems from their characteristics of allowing gluing operations between laminate layers and solid elements which are used to model sensors and actuators. Solid-shell 190 is used in this case. Table 16 highlights some of the element output properties of the solid shell element.

Table 6.2: SOLSH190 element properties [28]

SOLSH190 Property	Definition
8 Nodes	I, J, K, L, M, N, O, P
Degrees of freedom	UX, UY, UZ
Real constants	None

The actuator and sensor models retain similar properties that were assigned in the previous chapters respectively. They both retain solid element 5 and PZT material properties listed in chapter 3. However, the propagating signal changes its frequency. The Lamb wave signal is propagated through the composite plate at 85 kHz.

In terms of the model setup preprocessing, similar boundary conditions utilized in the aluminum plate simulation are used with the composite plate. These include:

- fixing one end of the plate while the other end remains free

- Attaching the actuator on the free end
- Attaching the sensors on the fixed end
- Setting the upper coupled nodes of the sensor to 0 voltage
- Setting the lower coupled set nodes of the actuator to 0 voltage
- Utilizing the same end time and time step

## 6.2 Deformations

Figures 53 to 56 illustrate deformations on the composite plate during the ramped loading phase. Less deformation occurs at the beginning of the load application compared to the end. Additionally, there is more deformation around the damaged areas. This is due to lower material strength in those areas as a result of the damage. Also, a subtle difference is noticeable between the deformed plate with a cut and that with delamination at the end of the ramped load, the delaminated plate experiences slightly less deformation. This may be due to the difference in the size of the damage or the location of the damage.

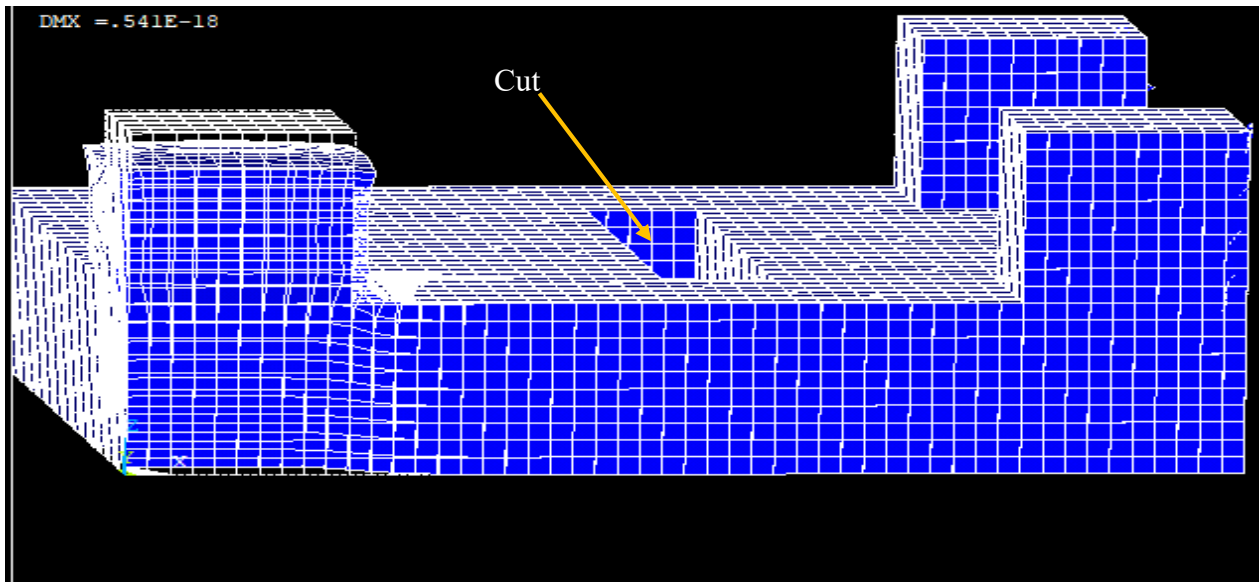


Figure 6.2 - The deformation of a 0.01m thick carbon composite plate with a cut at the beginning of the loading sequence.

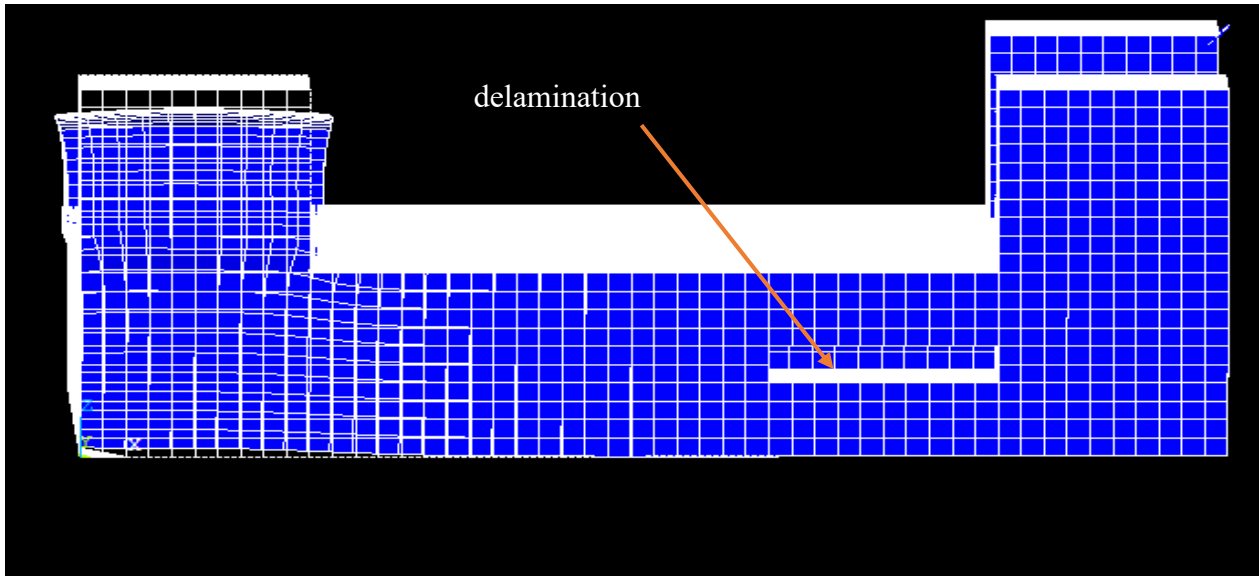


Figure 6.3 - The deformation of a 0.01m thick carbon composite plate with a delamination damage at the beginning of the loading sequence.

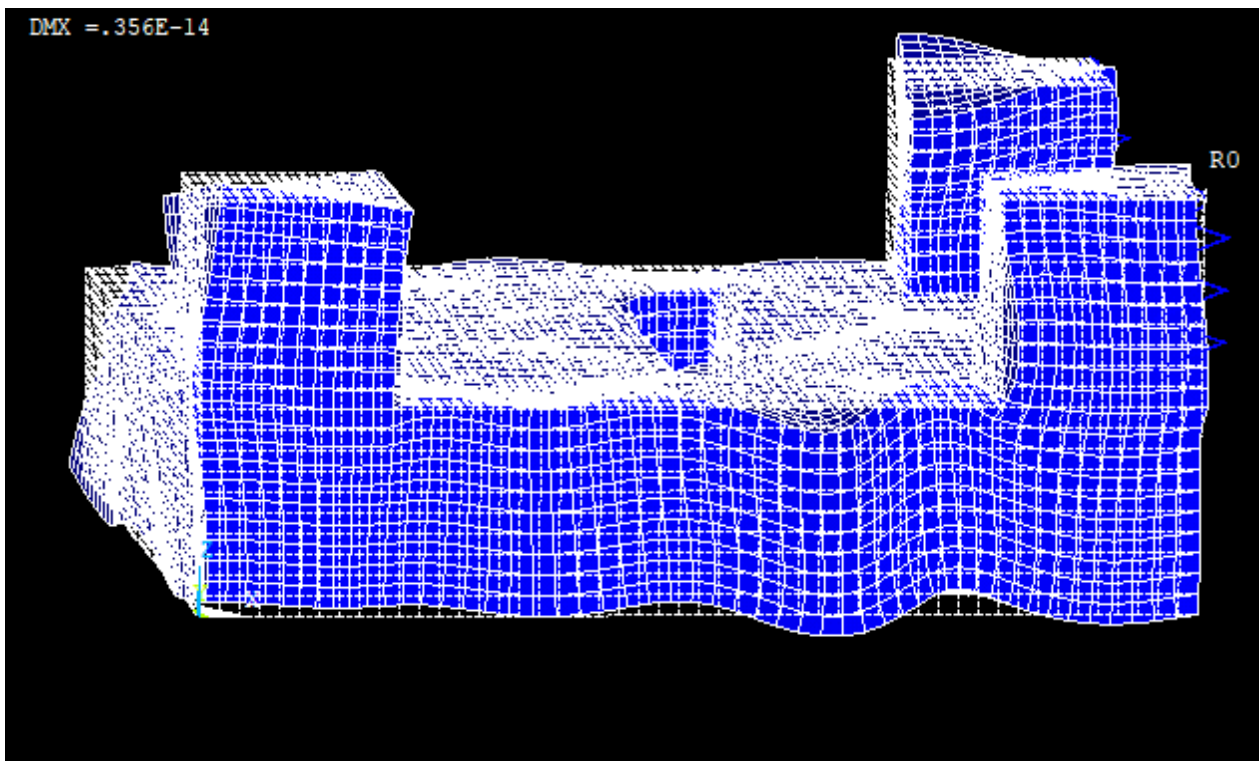


Figure 6.4 - The deformation of a 0.01m thick carbon composite plate with a cut at the end of the loading sequence.

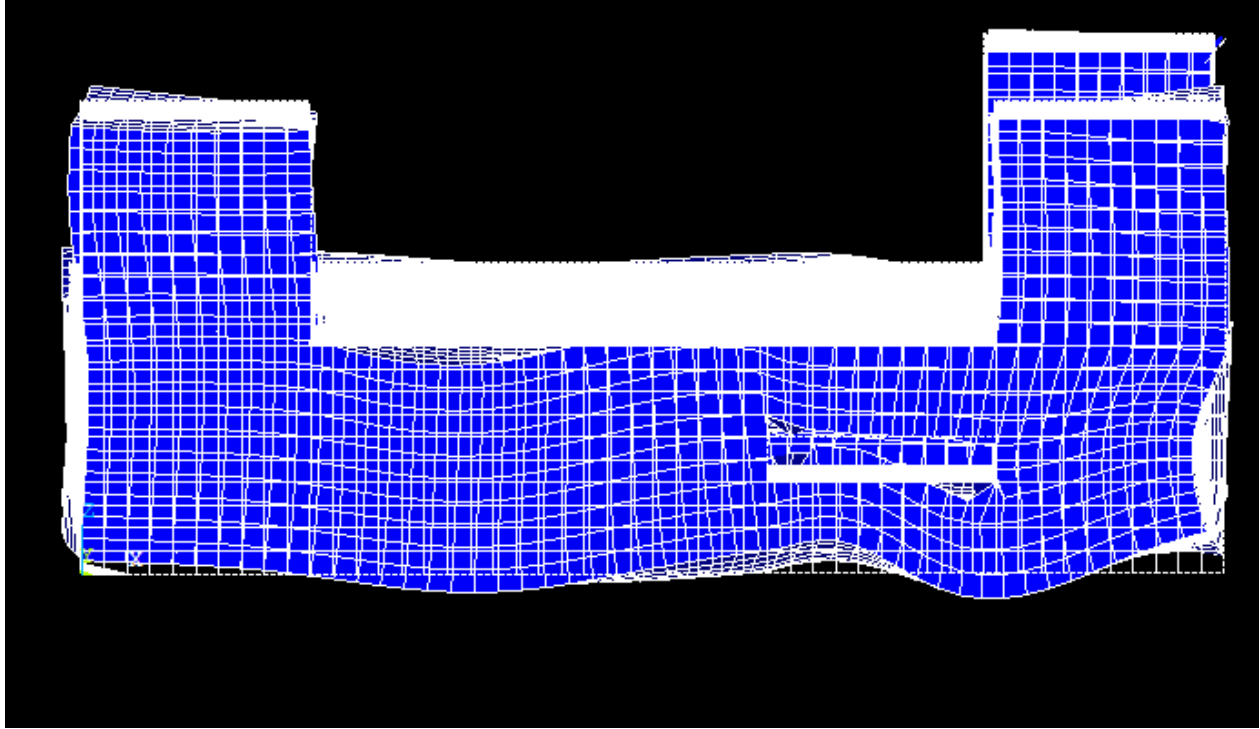


Figure 6.5: The deformation of a 0.01m thick carbon composite plate with a delamination damage at the end of the loading sequence.

## 6.2 Electric potential output

The electric potential output plots follow a similar trend to the deformations. Figures 57 to 60 below show an upwards progression of the distribution of the potential with the ramping up of the load. At the beginning of the loading, the potential is concentrated at the actuator, this changes with increased loading, resulting in a fairly uniform distribution with few high peak areas. These high peak areas occur around the actuator and sensor edges. This is likely due to the high torsional and lateral displacement activity around these edges, corresponding to a higher voltage generation. There isn't much of a distinction in terms of potential distribution around the cut and delaminated areas. There are, however, larger deformations as shown previously.

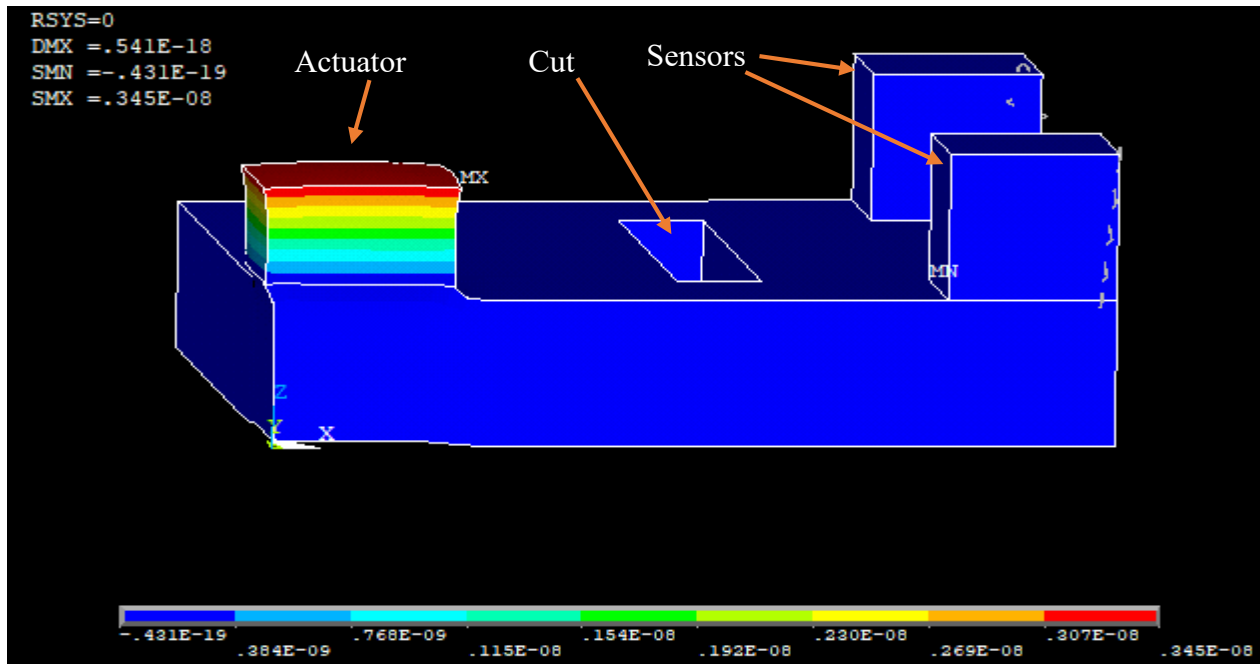


Figure 6.6 - The electric potential distribution in a composite plate with a cut at the beginning of the ramped load application

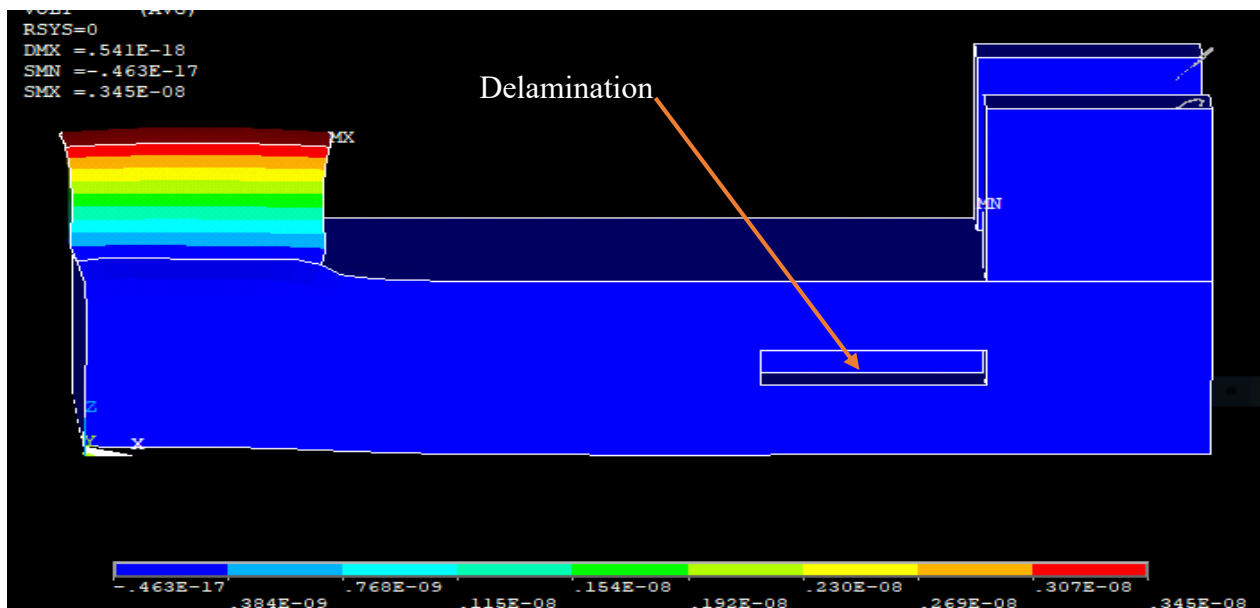


Figure 6.7 - The electric potential distribution in a composite plate with a delamination damage at the beginning of a ramped load application

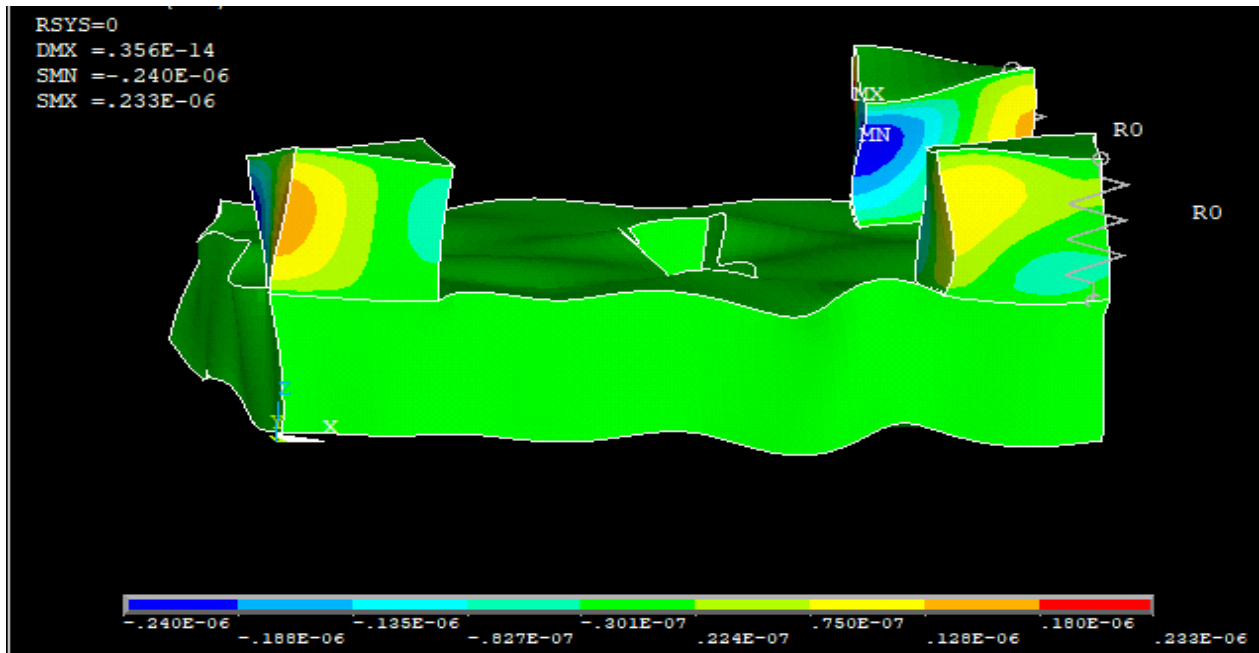


Figure 6.8 - The electric potential distribution in a composite plate with a cut at the end of a ramped load application

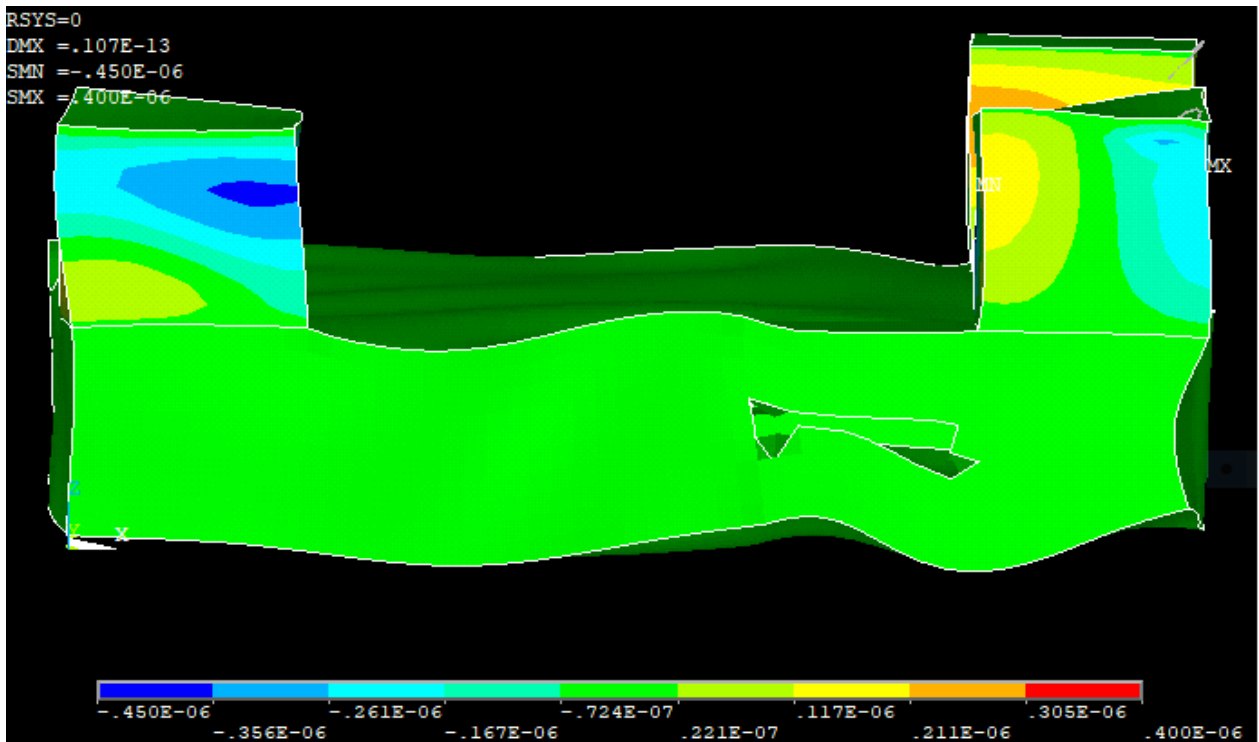


Figure 6.9 - The electric potential distribution in a composite plate with a delamination damage at the end of a ramped load application

### 6.3 Denoising of Nodal electric potential output

Corresponding to the action in the previous chapter when carrying out an analysis on the aluminum plate, denoising of difference signals is also carried out in the case of the composite plate. This is to eliminate the low energy level signals that cloud the visualization of peak areas. By denoising the signals from differences stemming from both the cut/delaminated plate and the pristine plate, a clear signal is generated that provides more clear peaks on the spectrogram. Figures 61 to 65 depict both the original and denoised signals in the two test cases. A noticeable trend is the high penalization of low-energy signals at the leading edge of the domain. This is likely a result of less interference of signals in the damaged plate at this location, due to the damage occurring near the trailing edge. As a result, the healthy and damaged signals closely resemble, resulting in low-level energy differences.

As a recap, denoising is carried out using a DB signal at the sampling frequency that corresponds to the 85kHz frequency. A continuous wavelet is then applied to the denoised signal to generate corresponding spectrograms.

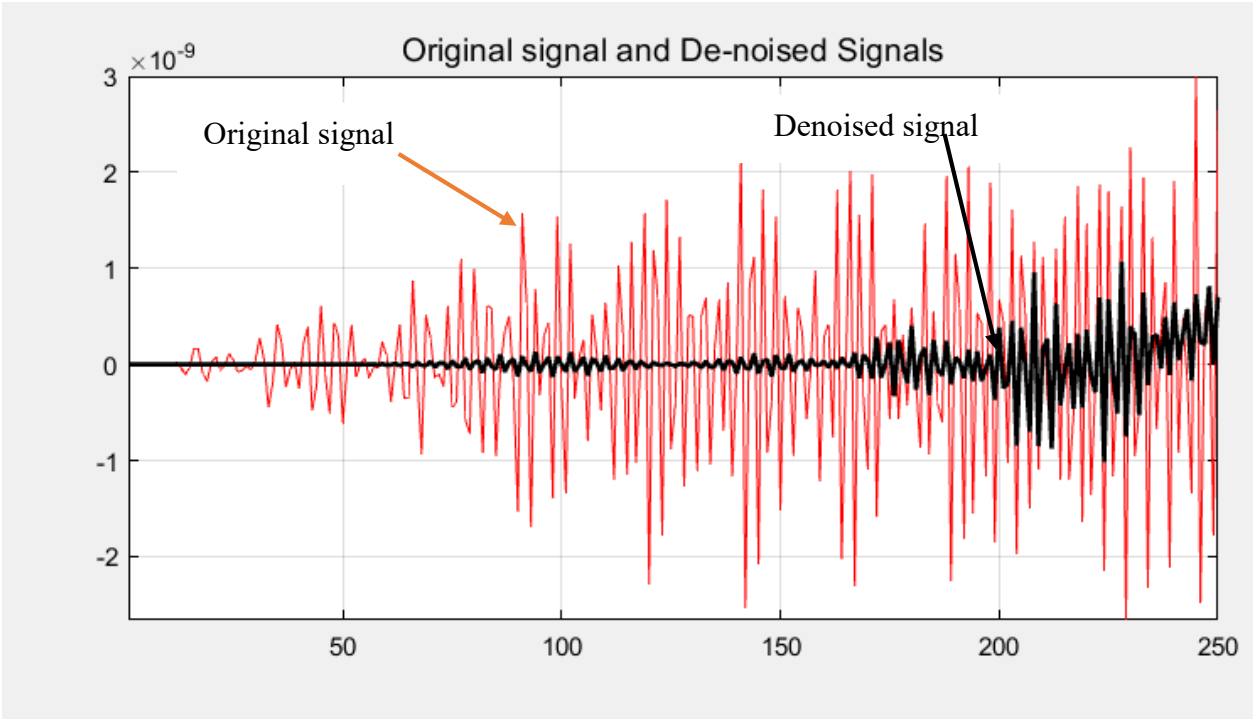


Figure 6.10 - Original and denoised signals of the difference between healthy and delaminated composite plate outputs registered by sensor 1

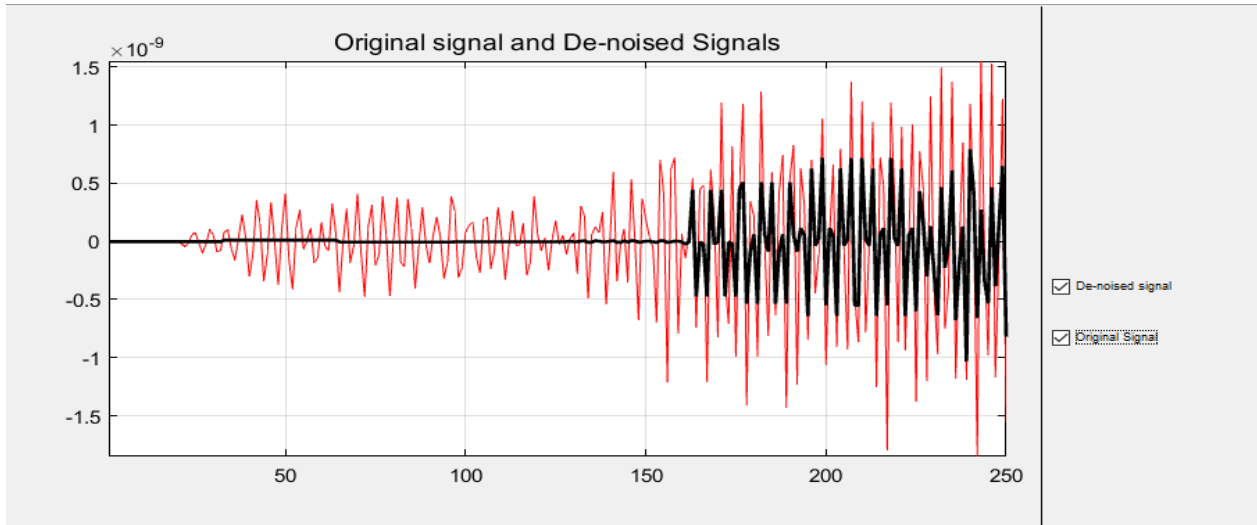


Figure 6.11 - Original (red) and denoised (black) signals of the difference between healthy and damaged (containing cut) composite plate outputs registered by sensor 1

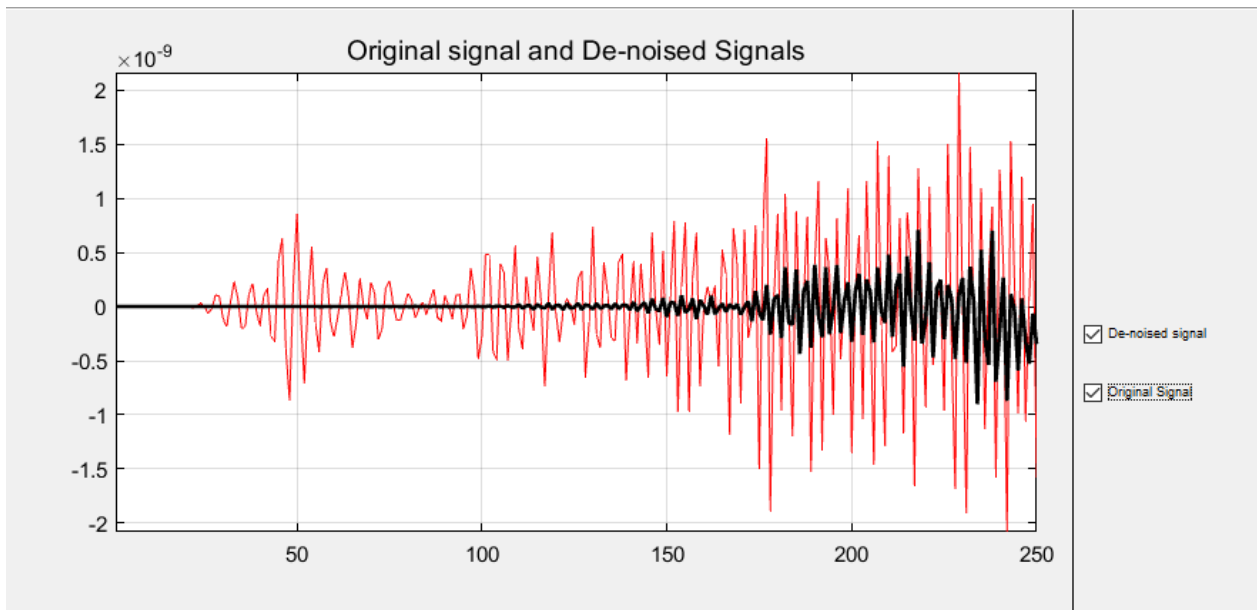


Figure 6.12 - Original and denoised signals of the difference between healthy and delaminated composite plate outputs registered by sensor 2

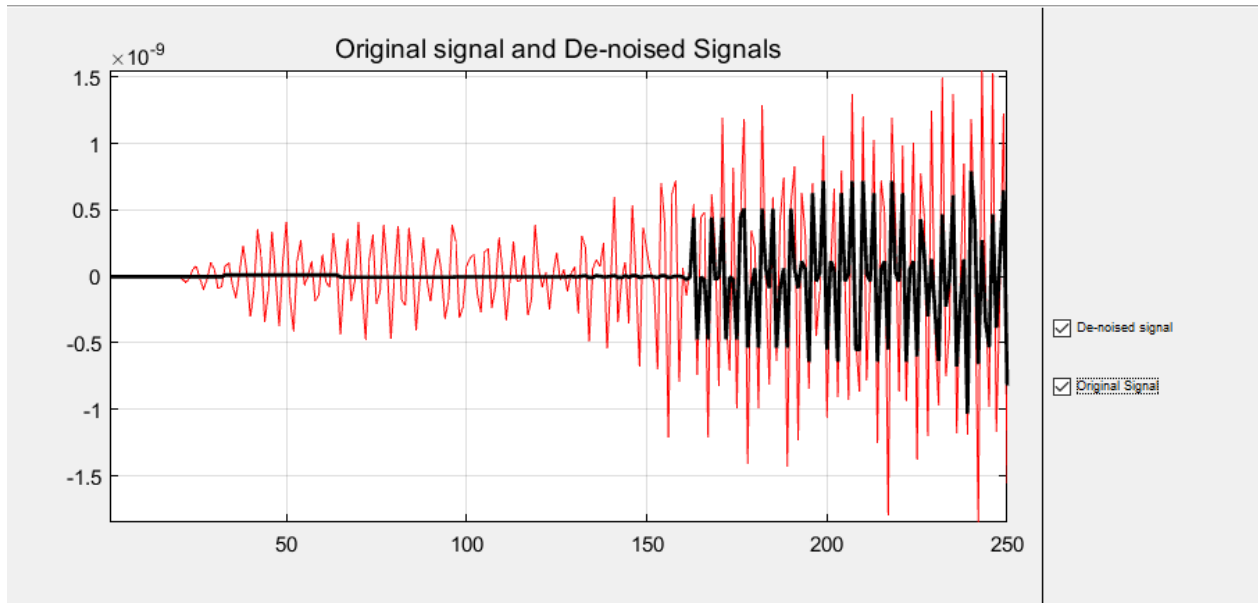


Figure 6.13 - Original (red) and denoised (black) signals of the difference between healthy and damaged (containing cut) composite plate outputs registered by sensor 2

## 6.4 Composite plate output signal Spectrograms

Figures 65 to 68 depict spectrograms resulting from both sample plate denoised signals at both sensors. The spectrograms allow us to visualize high peak signal areas and retrieve their arrival times. These arrival times, together with the wave velocities are then used to obtain the damaged geodesics. Similar to what was seen in the denoised signal, a majority of high peak signals occur at the tail end of the spectrograms, with a few less pronounced at the leading edges. Spectrograms from the cut-pristine difference signal indicate more high peak activity than the delamination. This may be due to their relative sizes or their locations. Arrival times derived from these spectrograms are used in the next section to obtain damage geodesics.

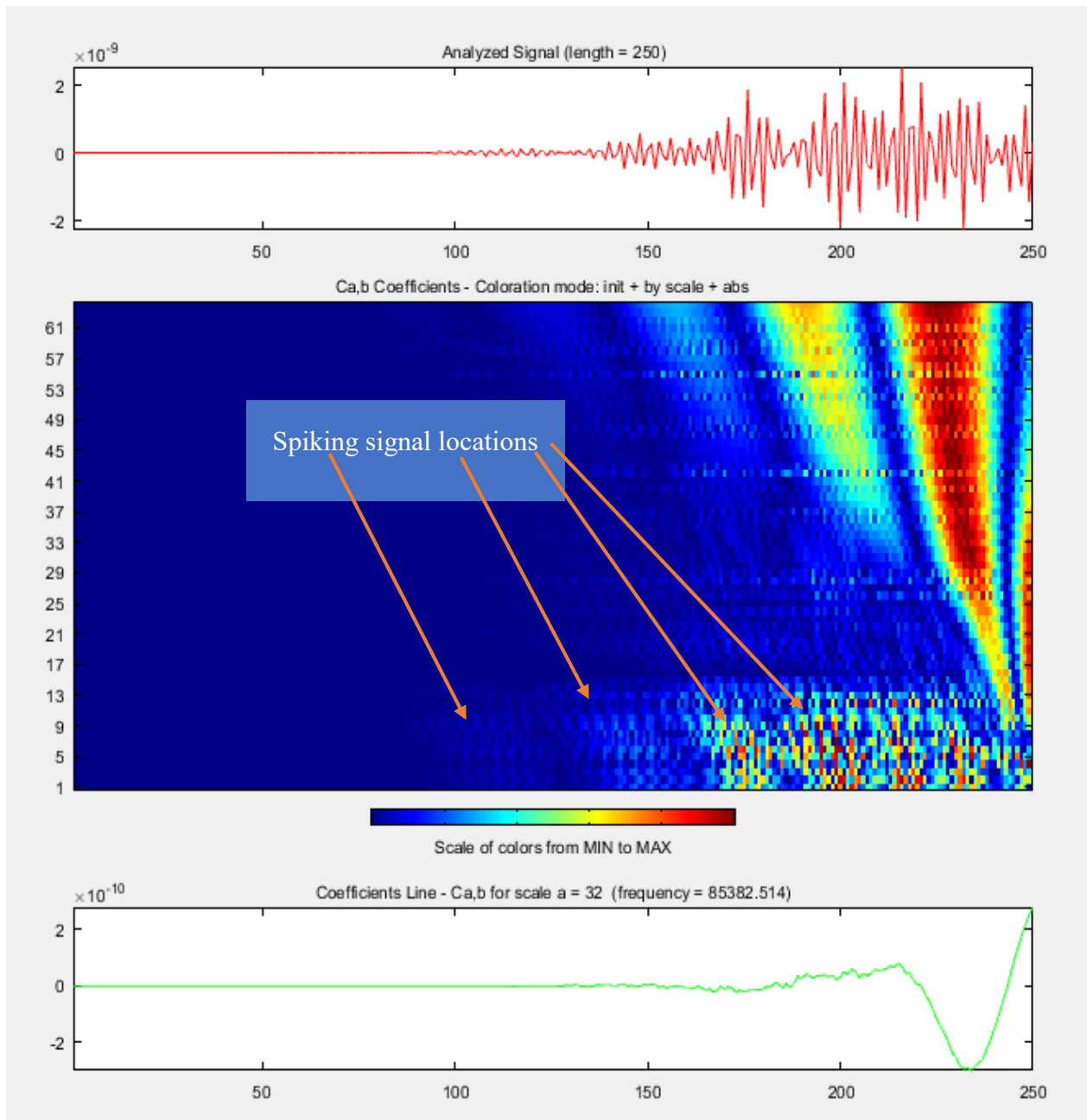


Figure 6.14 - Spectrogram from the difference between pristine composite plate and damaged (cut) composite plate voltage output derived from sensor 1.

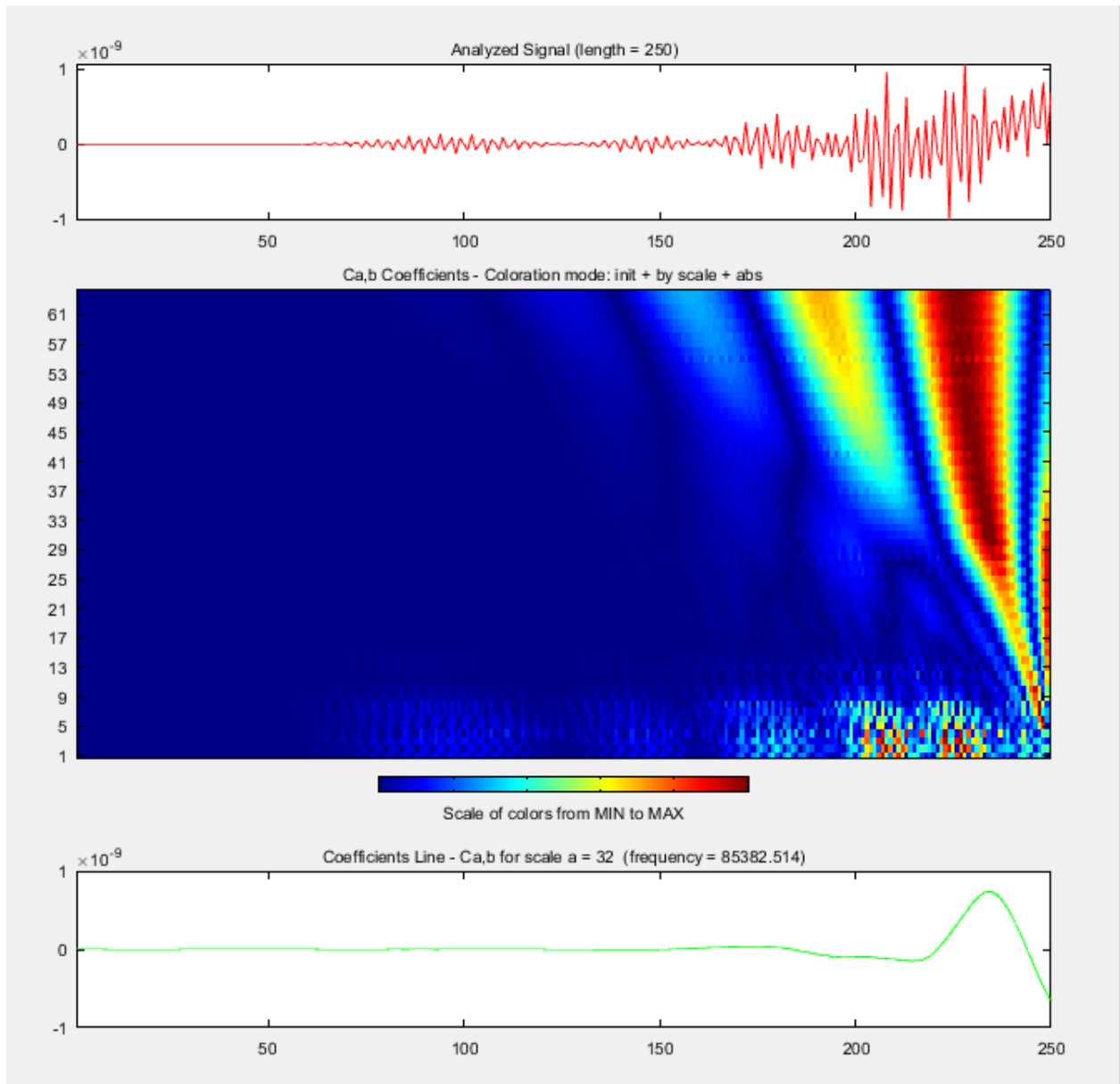


Figure 6.15 - Spectrogram from the difference between pristine composite plate and damaged (delamination) composite plate voltage output derived from sensor 1.

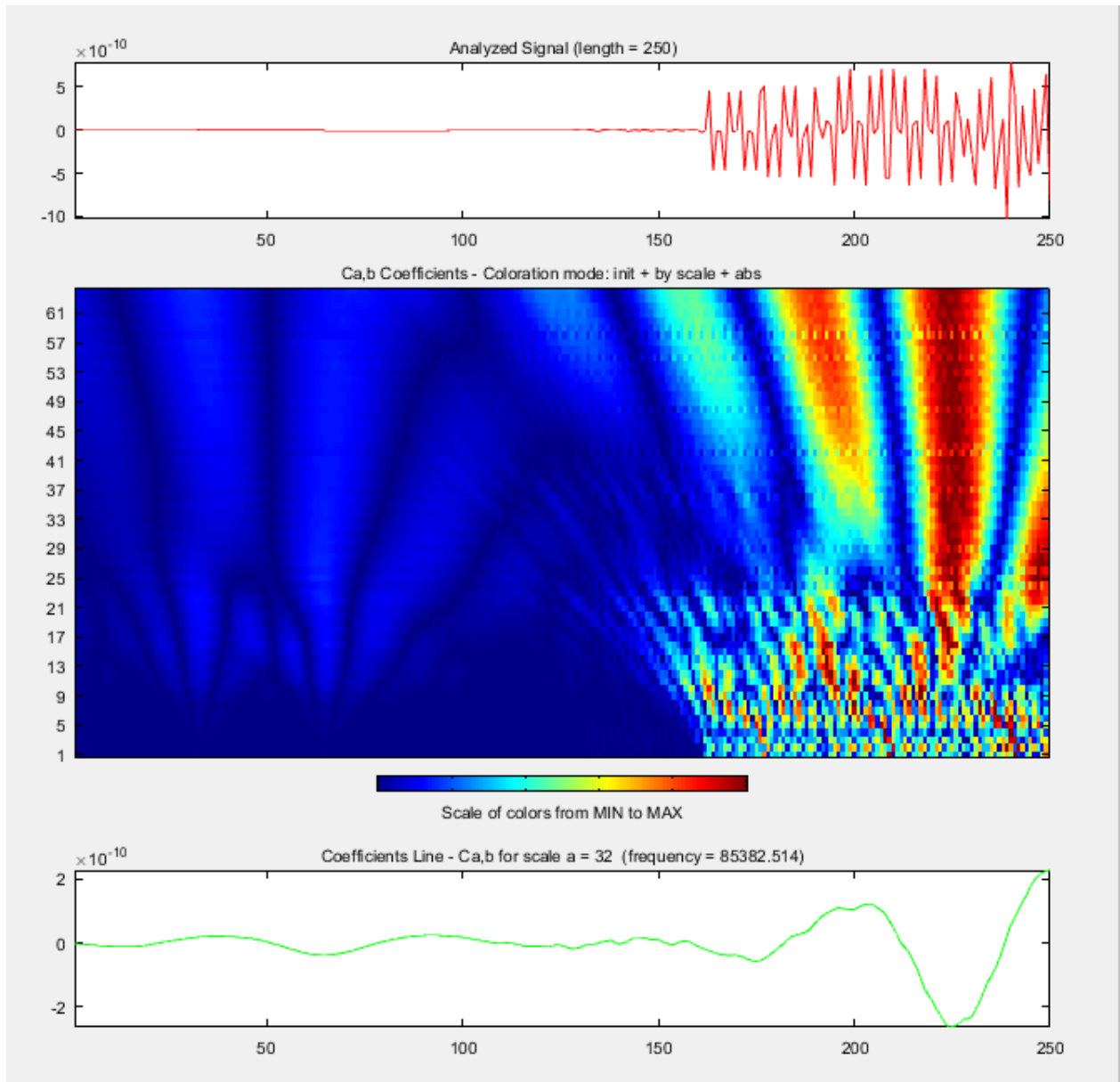


Figure 6.16 - Spectrogram from the difference between pristine composite plate and damaged (cut) composite plate voltage output derived from sensor 2.

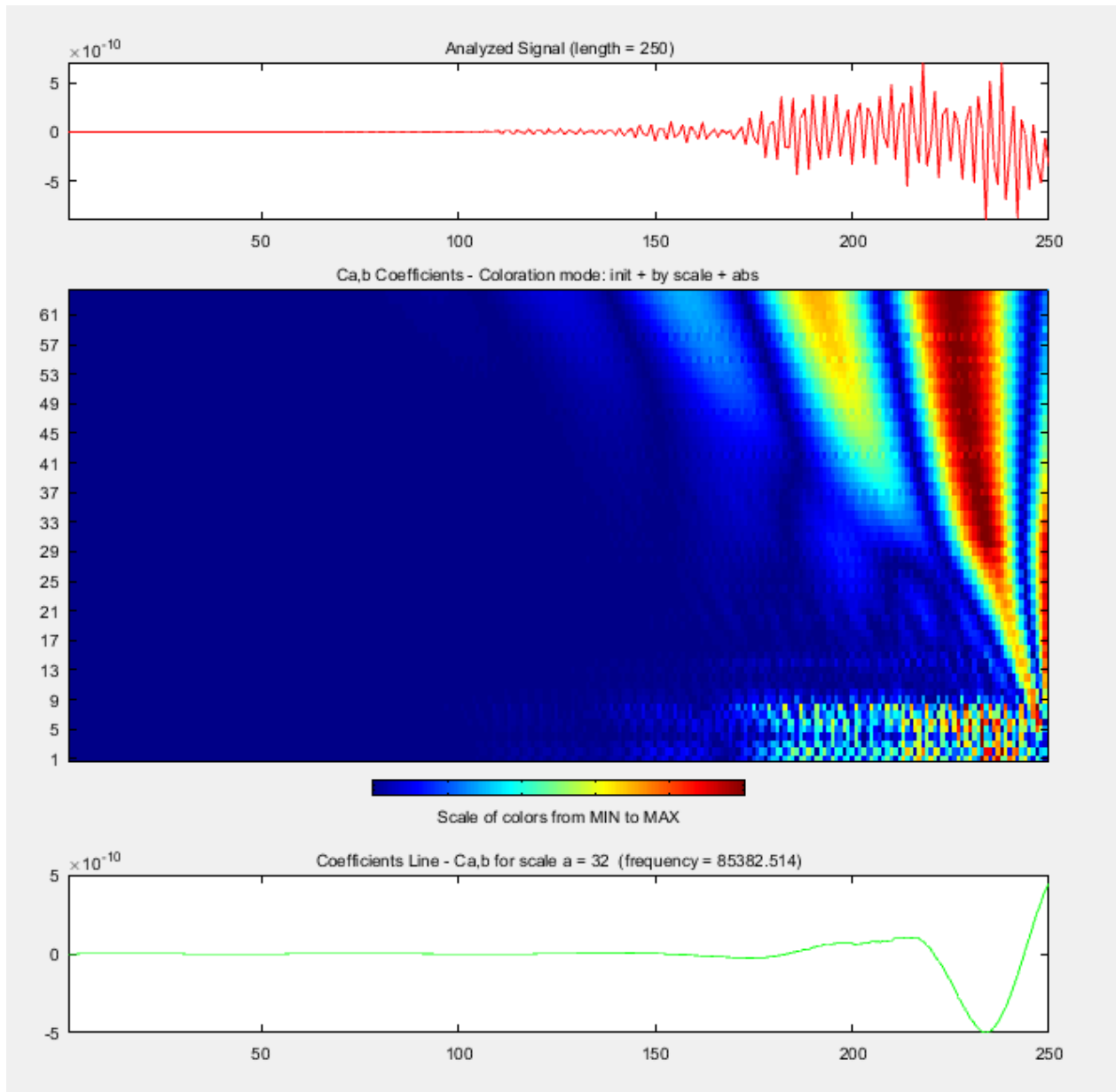


Figure 6.17 - Spectrogram from the difference between pristine composite plate and damaged (delamination) composite plate voltage output derived from sensor 2.

## 6.5 Damage Geodesics

Obtaining the damaged geodesics follows a correspondingly similar approach to how they were obtained in the aluminum plate case. As a recap, after obtaining the high peak voltage positions on the spectrograms, the corresponding arrival times are located within the sensor data set. The arrival times, together with the wave velocities are then used to calculate damage geodesics. It is at the intersection of a pair of damage geodesics from both sensors, that the x and y coordinates of damage locations illustrated in Table 17 are derived. These coordinates will be used later to plot approximate damage locations. Figures 69 to 73 illustrate the geodesic plots of the damage from which the x y location coordinates are derived. While in both damage cases, the geodesics are in general proximity to the modeled damage, the geodesics better approximate the cut damage than the delamination. This is due to the intersection of geodesics around the modeled cut damage compared to their intersection on the fringe of the delamination. Adjustment of center locations of geodesics improves their approximations, although only by small margins

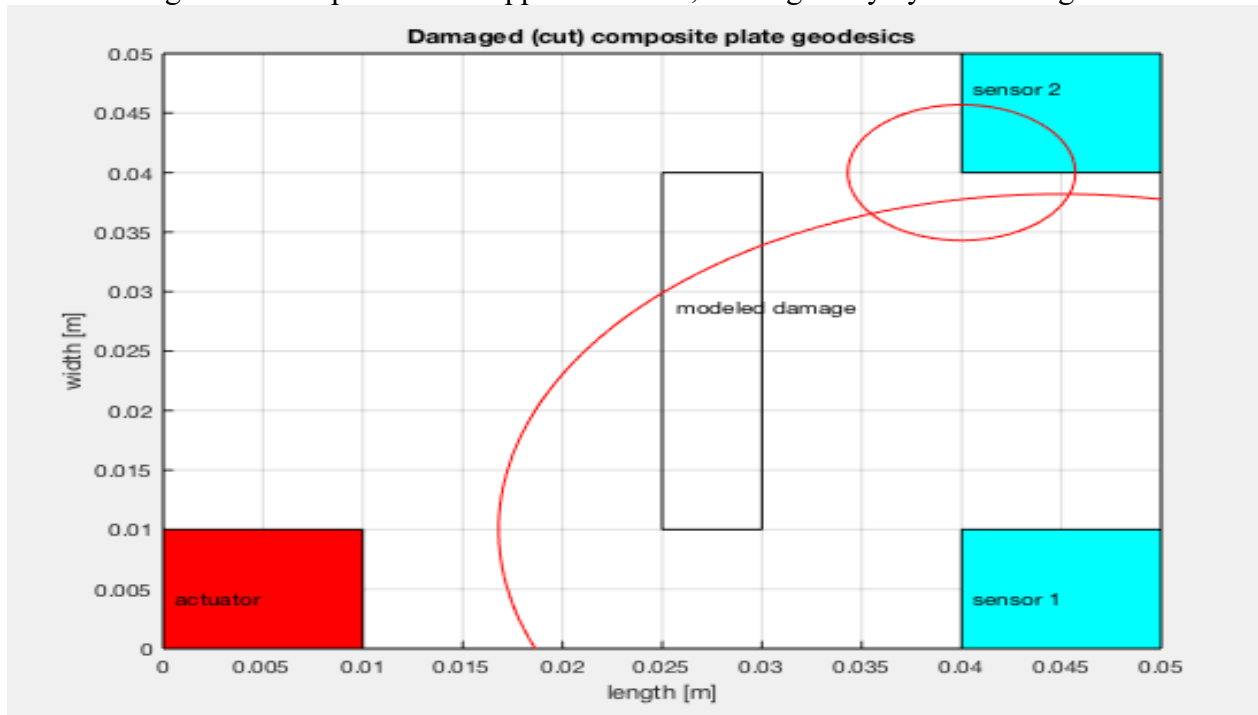


Figure 6.18 - Approximate geodesic damage location plot on composite plate with modeled cut damage

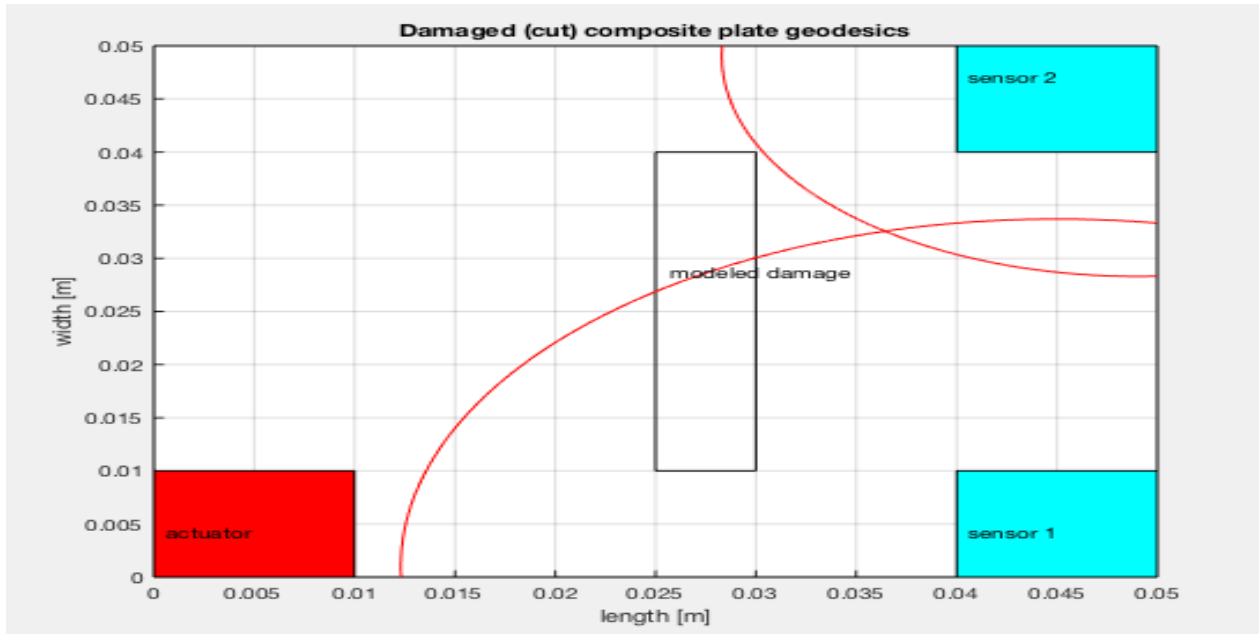


Figure 6.19 - Approximate geodesic damage location plot on composite plate with modeled cut damage

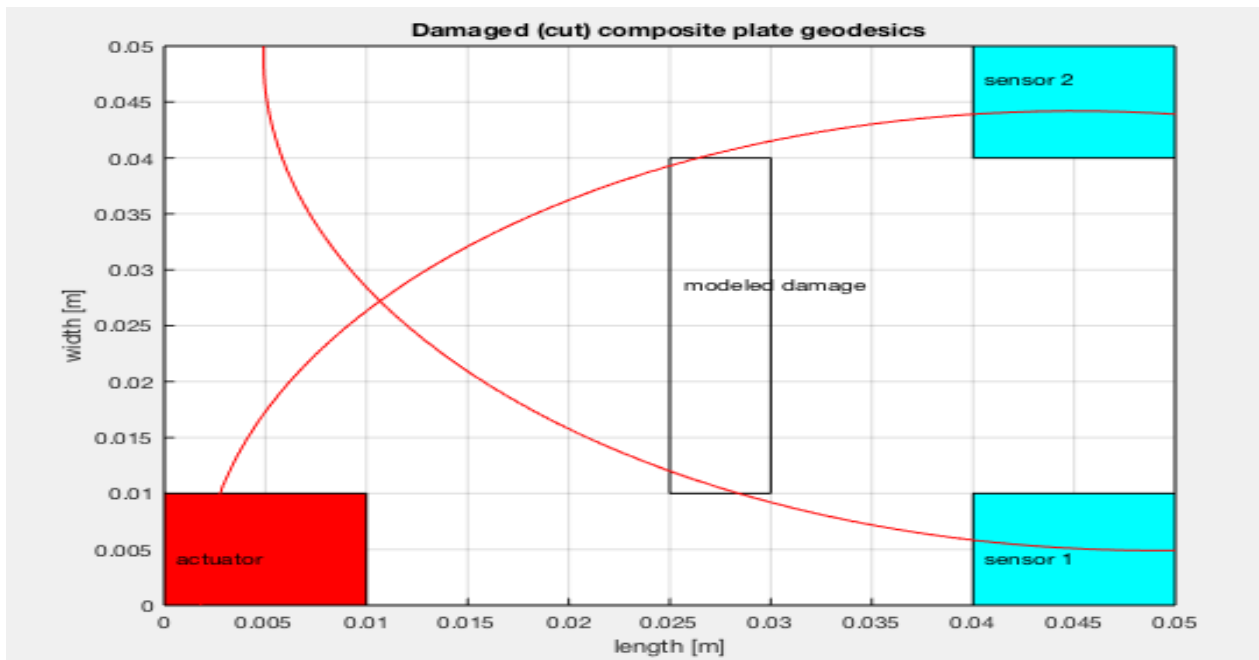


Figure 6.20 - Approximate geodesic damage location plot on composite plate with modeled cut damage

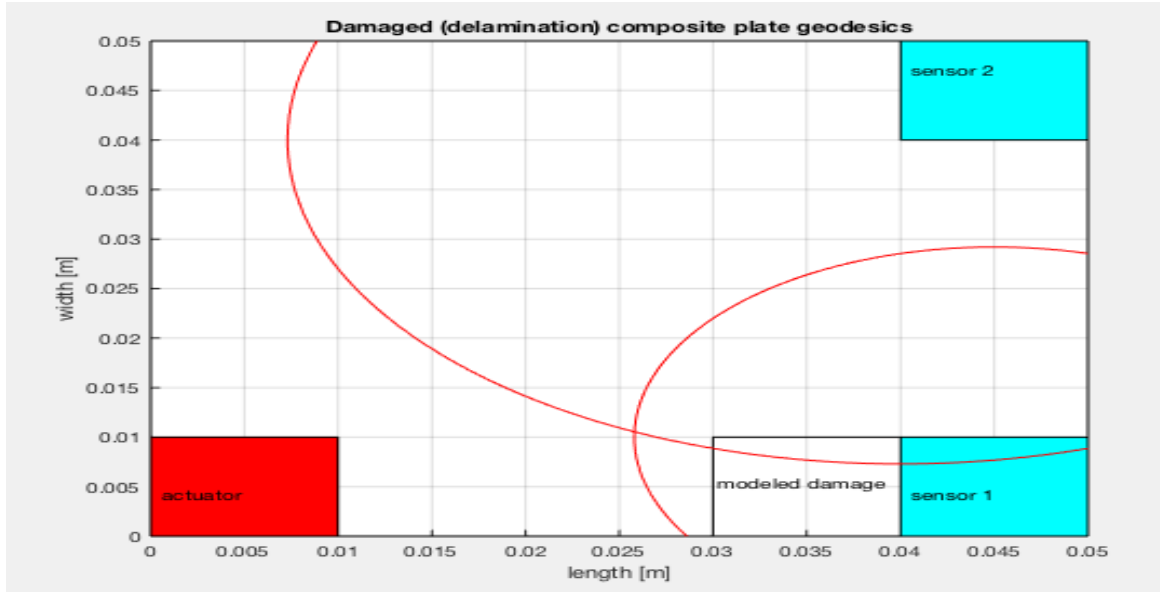


Figure 6.21 - Approximate geodesic damage location plot on composite plate with modeled delamination damage

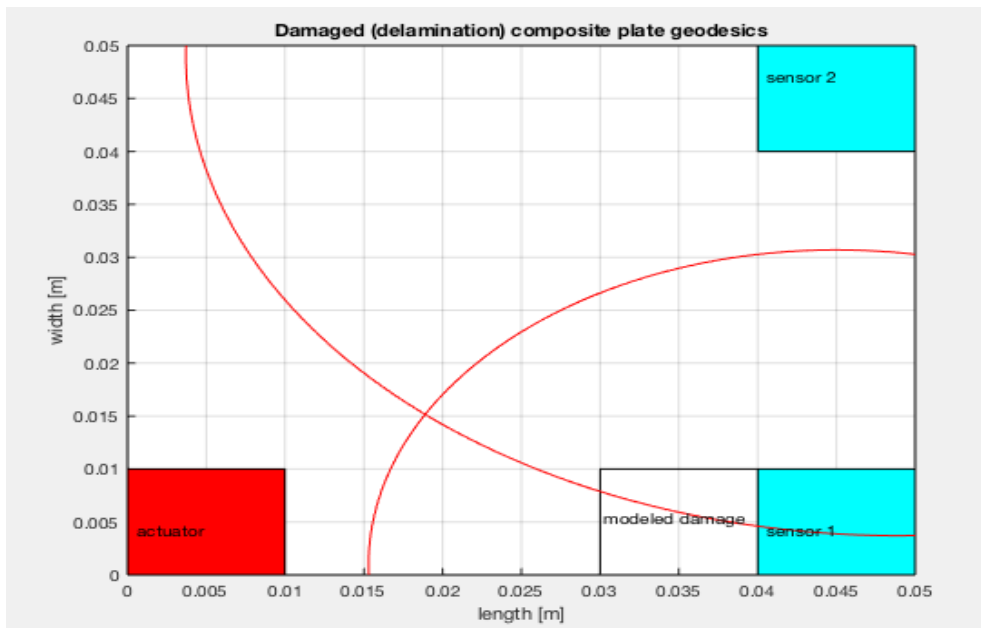


Figure 6.22 - Approximate geodesic damage location plot on composite plate with modeled delamination

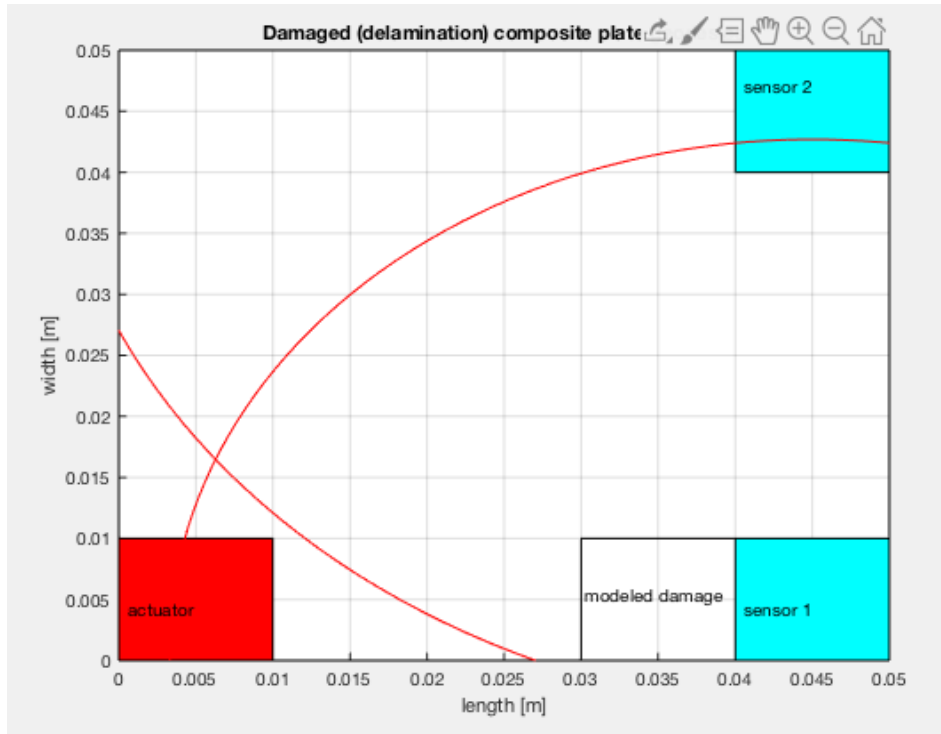


Figure 6.23 - Approximate geodesic damage location plot on composite plate with modeled delamination damage

Table 6.3 - X and Y coordinates of damage location obtained from geodesic plots

Composite plate with cut		
Pair number	Location	
	X [m]	Y [m]
1	3.545E-2	3.656E-2
2	3.665E-2	3.239E-2
3	1.075E-2	2.705E-2
Composite plate with delamination		
1	2.578E-2	1.055E-2
2	1.865E-2	1.537E-2
3	6.162E-3	1.662E-2

### 6.6 Damage locations

The damage location coordinates obtained from the geodesic intersections are used to plot the damage locations on the composite plate. A good amount of the approximated damage location falls within the modeled damage area for the plate with the cut.

For the plate with the delamination, however, the approximated damage falls outside the modeled damage area for the three sets of results. While figures 76 to 78 illustrate approximate damage locations about a quadrant away from the damaged location on average, this distance is considerably large when compared to the relative size of the plate. A more refined mesh gets the approximation closer to the modeled damage as seen by improvements in figures 77 and 78. When the simulations, however, incorporate a larger modeled delamination relative to the plate size as seen in figure 79, the method provides a good approximation of the damage. It is therefore evident that the method has limitations when it comes to approximating delamination sizes that are smaller beyond a certain size. Future work will incorporate a convergence analysis to determine what this limit is.

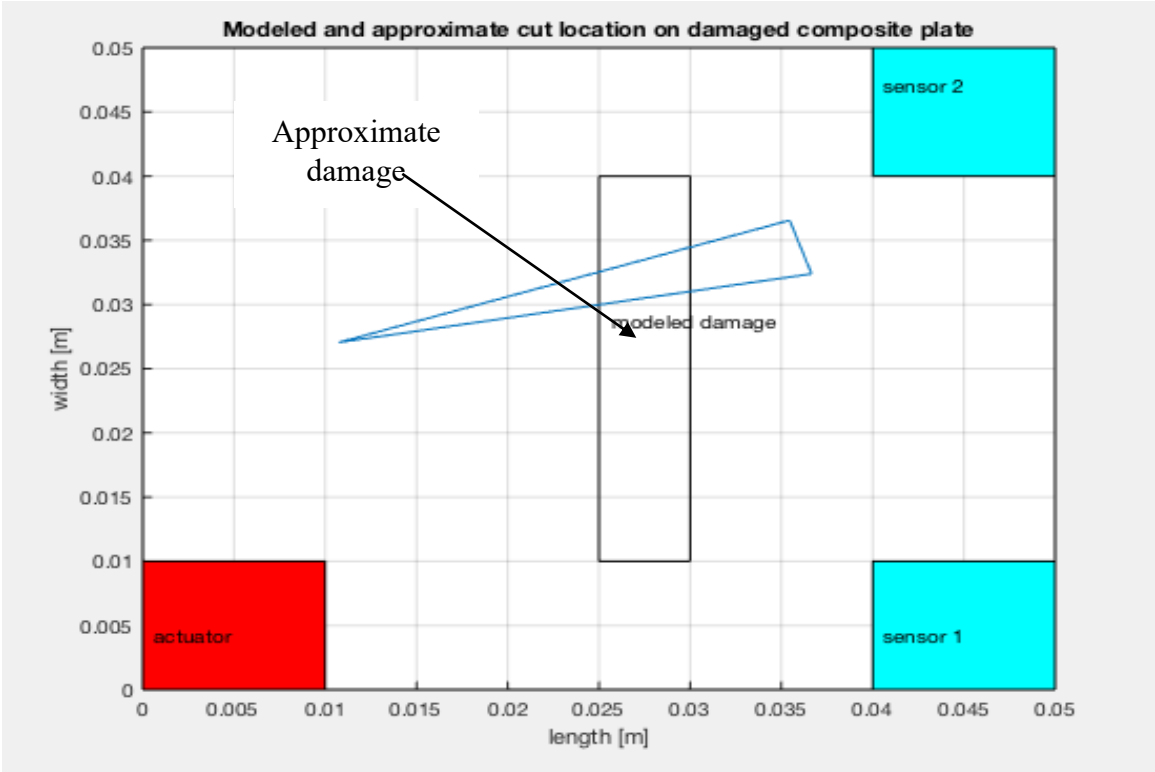


Figure 6.24 - Approximate vs modeled damage (cut) locations on a composite plate

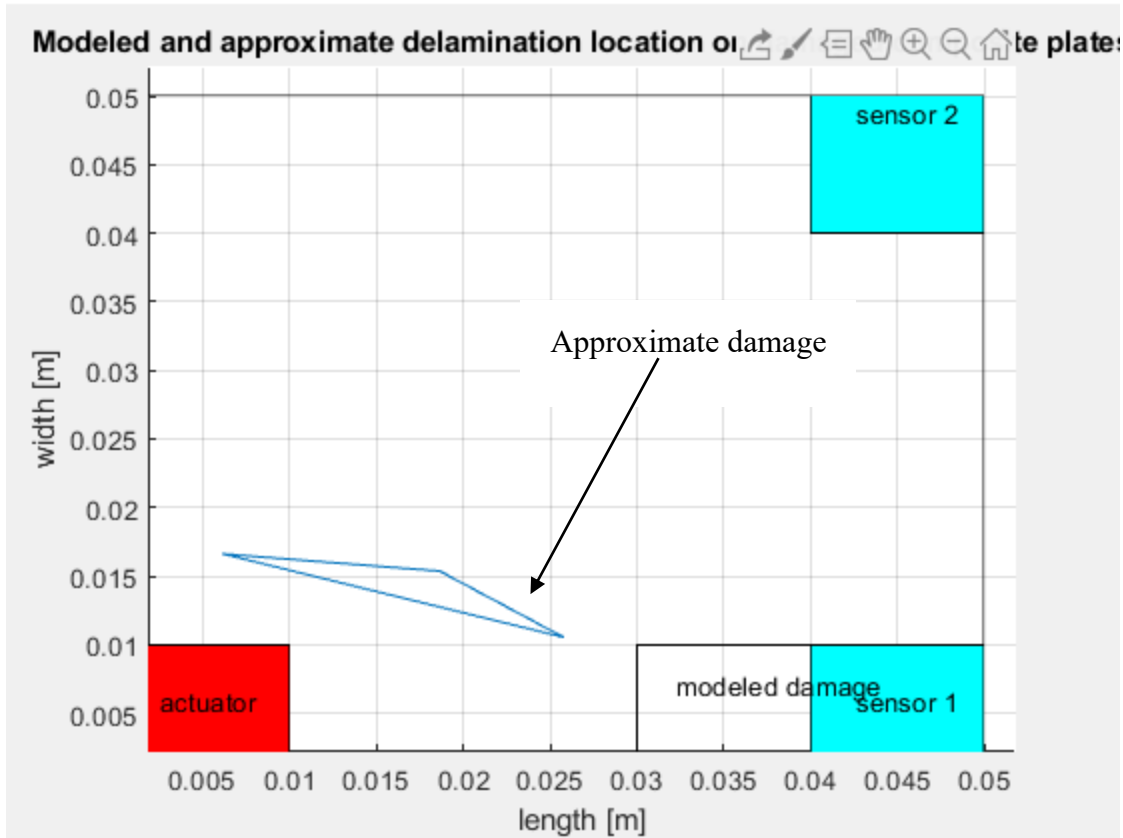


Figure 6.25 - Approximate vs modeled damage (delamination) locations on a composite plate

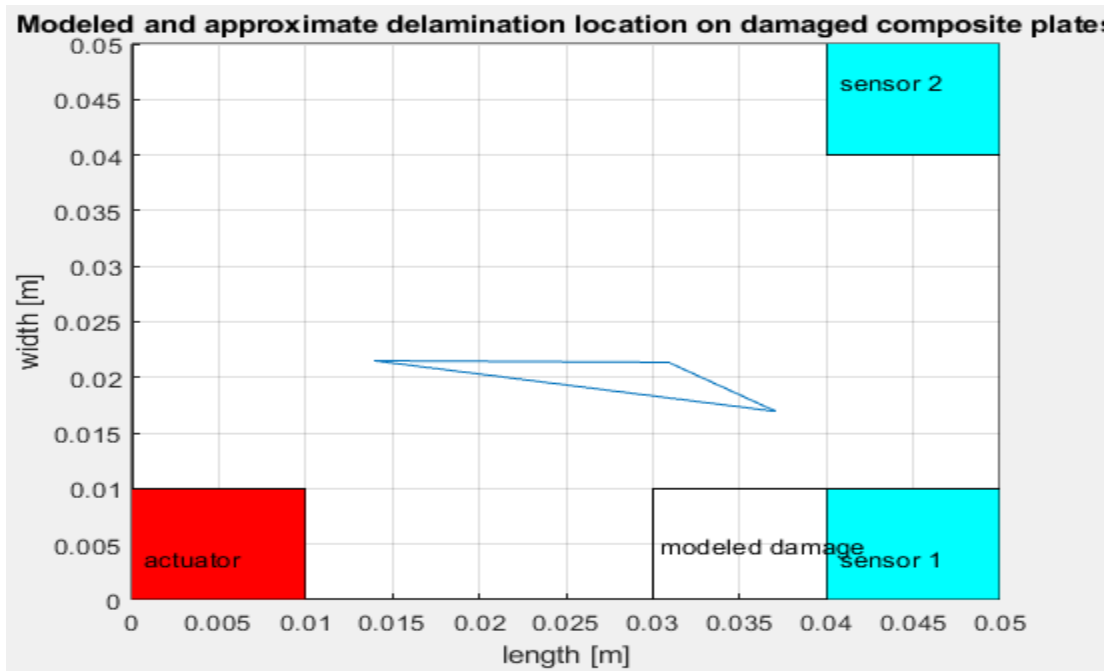


Figure 6.26 - Approximate vs modeled damage (delamination) locations on a composite plate

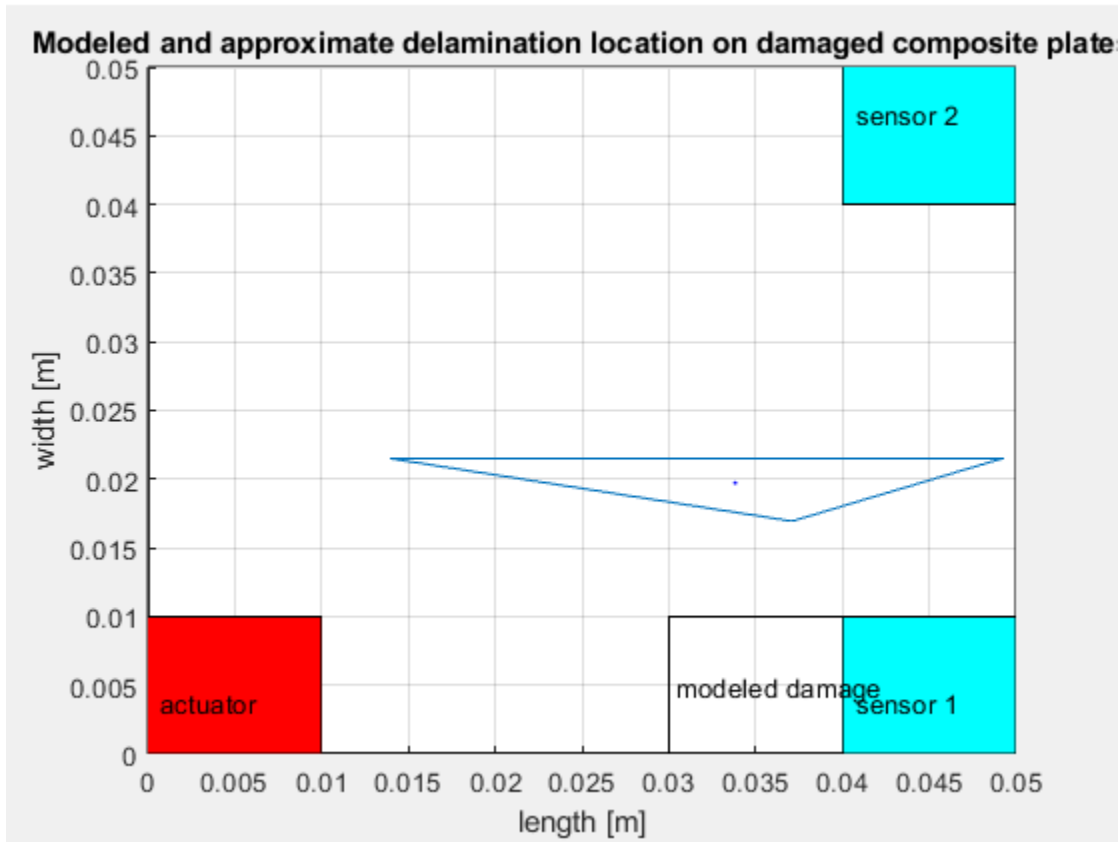


Figure 6.27 - Approximate vs modeled damage (delamination) locations on a composite plate

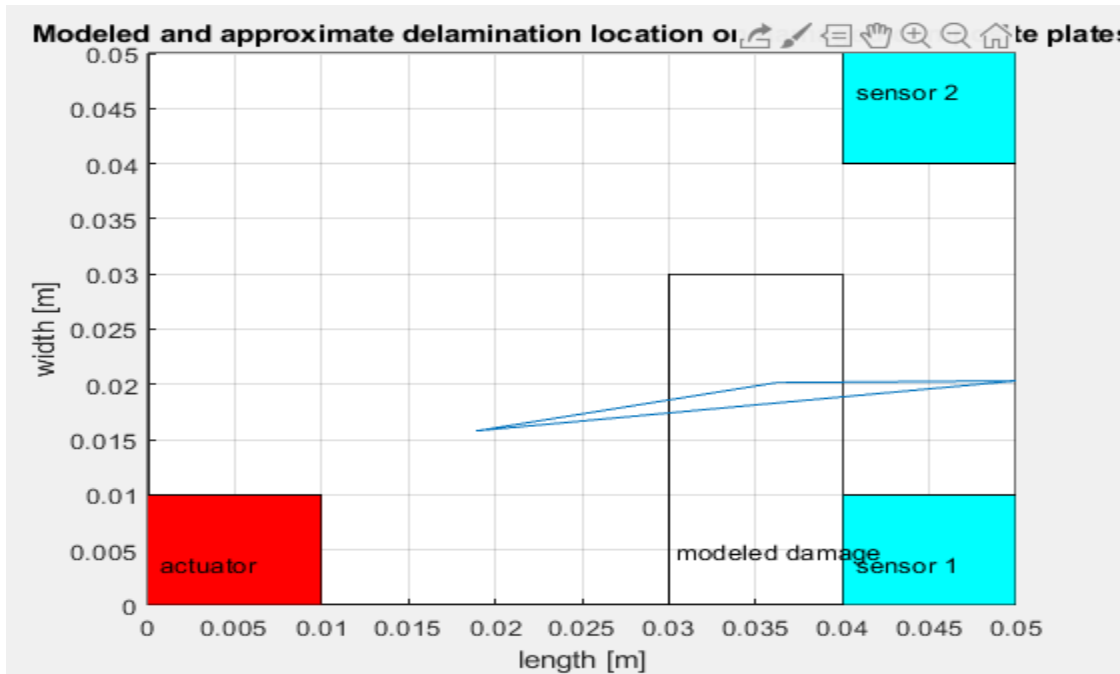


Figure 6.28 - Approximate vs modeled damage (delamination) locations on a composite plate

The data in Table 9 provides a dimensionless view of the approximations relative to the size of the plate and thus can be extended to other plate sizes. The analysis involves calculating the distance between the centroids of the modeled damage and those of the corresponding approximated damage. The difference is then used to obtain a percentage figure relative to the corresponding plate length. It is evident that the approximations in the plate with a cut were very good, with the percentage difference being under 15% relative to the plate size, and the damage locations overlapping.

The plate with the delamination however produced results that were not satisfactory for delamination of 0.01 by 0.01 meters. While there was progress towards a better solution through mesh refinement, a simulation with a slightly bigger delamination size (0.01 by 0.03 meters) resulted in good tracking of the modeled damage by the approximation. This shows that the technique is capable of providing good approximations of different types of damage, as long as the damage size limitations are observed. Overall, detection of damage using Lamb waves has shown significant promise by providing good results.

Table 6.4 - Centroid location distance between modeled and approximated damage locations and percentages of differences to the plate length

Modeled damage	X centroid location [m]	Y centroid location [m]	Approximate centroid location [m]		Difference between modeled and approximate x centroid [m]	Difference between modeled and approximate y centroid [m]	Percentage difference X centroid to X length	Percentage difference Y centroid to Y length
			X	Y				
delamination	3.5E-2	5E-3	1.69E-2	1.42E-2	1.83E-2	9.2E-3	36.6	18.4
			2.73E-2	1.49E-2	7.7E-3	9.9E-3	15.8	19.8
			3.3E-2	2E-2	2E-3	3E-1	4	30
cut	2.75E-2	2.5E-2	2.76E-2	3.2E-2	1E-4	7E-3	0.2	14

## 7. Chapter 7 – Conclusion

Capturing what has been involved in the entirety of the project, this chapter provides a summary of the steps involved in carrying out the project. It encompasses research into the subject of lamb waves, setting up of FEA models, choice of parameters and how they affected the results, the simulations carried out, and, finally the results. The chapter concludes by discussing the results, suggesting future work for better results, and, providing a concluding opinion on the suitability of the technique from the study.

### 7.1 Aerospace composites and SHM

Structural health monitoring is the continuous/on-time assessment of the condition of material making up a structure to mitigate failures. There exists a variety of structural health monitoring techniques that can be applied to different situations depending on factors such as the size of the specimen, accessibility, and cost among others. Structural health monitoring techniques can be categorized into non-destructive and destructive tests. Non-destructive tests preserve the quality of the material after the test and hence the structure can resume normal function once it passes the test. Destructive testing on the other hand involves testing the material to failure, hence structure cannot be put back to service after the test.

Non-destructive testing is critical in industries such as aerospace, where parts are usually made out of often expensive materials. Additionally, the costly nature of the failure of parts during operational service calls for early detection and correction of factors that might result in such failures. Therefore, SHM through non-destructive testing has immense applications in the aerospace industry. Examples of tests implementing non-destructive structural health monitoring include wing bending tests, landing gear drop tests, and, ultrasonic tests of the fuselage.

Aerospace parts often have stringent strength and weight properties hence making it difficult and expensive to find one single mineral material that can meet most of the requirements. It is therefore common practice to find aerospace materials made by combining different materials in a variety of ways depending on the end goal. Composite parts or materials are those that are made using more than one material. However, the production of these parts isn't always a seamless process, regardless of the high-quality standards set by the industry. Defects sometimes go unnoticed in parts. Defects that if left uncorrected would lead to premature failure of parts. Such defects include porosity, ply gaps and notches. In addition to manufacturing defects, accidents during maintenance sometimes lead to hidden defects that can grow and cause a major failure. This may include tool drop incidents that may initiate hidden cracks or delamination. These defects when not noticed early enough can result in costly and sometimes disastrous failures.

SHM provides techniques for assessing material to determine whether such defects exist and repair them on time. One technique of SHM that has been under research is the application of guided Lamb waves in the detection of damage in structures. This method can be applied through testing samples in a laboratory setting or modeling the samples and implementing the test through finite element analysis apparatus. Given the affordability and availability of the latter, this project focused on studying the application of guided Lamb waves to detect damage in plates via finite element analysis modeling. Lamb waves can be defined as a type of elastic wave whose propagation through a medium is dependent on reflection, refraction, and bulk mode conversion.

As a result, changes in material properties affect their propagation and lead to delays or loss of signals. It is this characteristic that SHM using guided lamb waves leverages.

## 7.2 Application of guided Lamb waves in a FEA environment

This project’s goal is to implement non-destructive structural health monitoring of composite structures through the propagation of Lamb waves. The models and tests were performed using Finite Element Analysis software. The first phase of the project involved researching lamb waves, their properties, applications, and previous work that had been done to advance their applications. Additional time was spent researching the modeling of PZT sensors and actuators to be utilized in the FEA tests. Piezo-electric Transducer (PZT) materials are a type of material whose electrical properties change with the application of a load and vice versa. Therefore, when a load, for instance in the form of a force is applied on one end of a PZT volume, the displacement of particles within the material results in the generation of a potential difference across the ends. On the other hand, the application of a voltage on one end of a PZT material volume results in expansion or contraction of the material depending on the sign of the voltage. These properties make PZT materials very useful as sensors and actuators.

The second phase of the project involved modeling a healthy aluminum plate sample test model. The model incorporated an actuator, two sensors, and the plate. The plate was fixed on one end and free on the other. The modeled actuator was attached on the free end, while the sensors were attached to the fixed end, at the extreme ends of the plate width. A voltage modeled using a Hanington function was used to model lamb waves. This wave was propagated through the plate and the resulting signal was collected from the sensor output location. Subsequent tests involved testing:

- Damaged (cut) aluminum plate
- Pristine composite plate
- Damaged (cut) composite plate
- Damaged (delaminated) composite plate

Several simulations were carried out to arrive at ideal setup conditions for running the simulations. Some of the variables that needed to be optimized for the iterations included:

- The element size (with consideration of the wavelength)
- The time step
- The model sizes

All these properties when refined improved the results. Hence it is vital to run several simulations to determine the appropriate parameters to run the models at. While more refined parameters meant better accuracy, increased refinement resulted in an increased time cost, and hence tradeoff had to be made to ensure a degree of accuracy and reasonable times for obtaining the results. The final parameters utilized for most of the models are:

Table 7.1- Optimal Parameters for simulation models

Parameter	Dimension	units
Element size	7.5E-4	Meters
Timestep	2E-6	seconds

Model size	0.05 by 0.05 by 0.01	Meters
------------	----------------------	--------

### 7.3 Results

The voltage results obtained from the sensors were used to calculate the difference in the signals emanating from the pristine plate and those from the damaged plates. However, before further analysis, denoising of the resultant signals had to be carried out. The signals obtained from the sensors contained a significant amount of noise and thus, their differences were also clouded with noise. This reduced the clarity of sharp peaks in the spectrograms. Therefore, a Matlab wave processing package was utilized to denoise the signals. Db signals were used as reference signals. The denoised signals provided clear spectrograms to be used in obtaining arrival time positions. Once the positions were located, they were matched to the corresponding arrival times in the signal data set. These arrival times, together with the wave velocities in the respective plates were then used to determine the damage geodesics. The geodesics were then plotted and their intersections were used to map out approximate damage location areas. Once these locations were obtained, they were plotted on the plates and contrasted with the modeled damage. This contrast was used to formulate an opinion on how good this SHM technique is in detecting damage in both aluminum and composite plates.

The results obtained hinted at a promising technique if optimized to the right setup parameters. The technique provided good tracking for modeled damage involving cuts in both the aluminum and composite plate, with centroid locations between the two types of damages (modeled and approximated) being less than 1% of the plate size in some instances.

On the other hand, the results obtained from composite plate delamination simulations did not accurately map the modeled damage location for small size delamination, despite continuously getting better at approximation when the mesh size was refined. Limitations of computational and time resources cut short further refinement of the simulations. However, when the size of the modeled delamination was increased the method provided a good approximation of the modeled damage. Hence, showing promising results. Future work will incorporate more simulations to determine the size beyond which the method fails to provide good approximations.

Overall, the results obtained provide good initial approximations of the modeled damage, despite being slightly off in some cases. Whereas the samples involved in this study were limited, benchmark studies with similar applications, have recorded good approximations of damaged areas, reinforcing the methodology as a good tool to implement in non-destructive structural health monitoring applications. This is a good additional tool in the testing of parts, especially composites, which may undergo internal delamination, which is difficult to visualize.

### 7.3 Future research

This project provided a good opportunity to apply guided Lamb waves to the SHM of material modeled in a Finite Element Analysis platform. Whereas the results obtained allowed the formulation of a preliminary conclusion on the efficacy of guided Lamb waves in SHM, further studies are needed to further reinforce the conclusion. A key aspect that needs to be further investigated, is the delamination size at which the methodology fails in providing good approximations. Additionally, the relationship between mesh size modeled damage size, and accuracy of the method need to be investigated further.

## 8. References

- [1] Zhang L., Wang X., Pei J., and Zhou Y., “Review of automated fibre placement and its prospects for advanced composites,” *J. Mater. Sci.*, vol. 55, no. 17, pp. 7121–7155, Jun. 2020, DOI: 10.1007/s10853019-04090-7.
- [2] Staszewski W., Mahzan S., and Traynor R., “Health monitoring of aerospace composite structures – Active and passive approach,” *Compos. Sci. Technol.*, vol. 69, no. 11, pp. 1678–1685, Sep. 2009, DOI: 10.1016/j.compscitech.2008.09.034.
- [3] Su Z., Tay T., Ridha M., and Chen B., “Progressive damage modeling of open-hole composite laminates under compression,” *Compos. Struct.*, vol. 122, pp. 507–517, Apr. 2015, DOI: 10.1016/j.compstruct.2014.12.022.
- [4] Bouvet C., and Rivallant S., “2 - Damage tolerance of composite structures under low-velocity impact,” in *Dynamic Deformation, Damage and Fracture in Composite Materials and Structures*, V. V. Silberschmidt, Ed. Woodhead Publishing, 2016, pp. 7–33. DOI: 10.1016/B978-0-08-100080-9.00002-6.
- [5] Turon A., Camanho P., Costa J., and Dávila C., “A damage model for the simulation of delamination in advanced composites under variable-mode loading,” *Mech. Mater.*, vol. 38, no. 11, pp. 1072–1089, Nov. 2006, DOI: 10.1016/j.mechmat.2005.10.003.
- [6] Liu P., and Zheng J., “Recent developments on damage modeling and finite element analysis for composite laminates: A review,” *Mater. Des.*, vol. 31, no. 8, pp. 3825–3834, Sep. 2010, DOI: 10.1016/j.matdes.2010.03.031.
- [7] Habib F., Martinez M., Artemev A., and Brothers M., “Structural health monitoring of bonded composite repairs – A critical comparison between ultrasonic Lamb wave approach and surface mounted crack sensor approach,” *Compos. Part B Eng.*, vol. 47, pp. 26–34, Apr. 2013, DOI: 10.1016/j.compositesb.2012.11.002.
- [8] Giurgiutiu V., “Chapter 2 - Fundamentals of Aerospace Composite Materials,” in *Structural Health Monitoring of Aerospace Composites*, V. Giurgiutiu, Ed. Oxford: Academic Press, 2016, pp. 25–65. DOI: 10.1016/B978-0-12-409605-9.00002-7.
- [9] Hassani F., Bouhfid R., and Qaiss A., “Modeling of Damage Evaluation and Failure of Laminated Composite Materials,” in *Structural Health Monitoring System for Synthetic, Hybrid and Natural Fiber Composites*, M. Jawaid, A. Hamdan, and M. T. Hameed Sultan, Eds. Singapore: Springer, 2021, pp. 101–125. DOI: 10.1007/978-981-15-8840-2\_8.
- [10] Elhajjar R., Grant P., and Ashforth C., *Composite Structures: Effects of Defects*. Newark, UNITED KINGDOM: John Wiley & Sons, Incorporated, 2018. Accessed: Sep. 30, 2021. [Online]. Available: <http://ebookcentral.proquest.com/lib/sjsu/detail.action?docID=5540446>
- [11] Irving P., *Polymer composites in the aerospace industry*, 1st edition. Cambridge, England ; Woodhead Publishing, 2015.
- [12] Yavas D., Gozluclu B., and Coker D., “Failure Mode Transition During Delamination of Thick Unidirectional L-Shaped Composite Laminates,” Nov. 2012, vol. 8. DOI: 10.1115/IMECE2012-88409.

- [13] Qian S., Liu X., Ye Y., Xu Q., Zhang T., and Li X., “Effect of gap and overlap fiber placement defects on the delamination behavior of L-shaped composite laminates,” *Compos. Struct.*, vol. 268, p. 113963, Jul. 2021, DOI: 10.1016/j.compstruct.2021.113963.
- [14] Li H., Yao Y., Guo L., Zhang Q., and Wang B., “The effects of delamination deficiencies on compressive mechanical properties of reinforced composite skin structures,” *Compos. Part B Eng.*, vol. 155, pp. 138–147, Dec. 2018, doi: 10.1016/j.compositesb.2018.08.034.
- [15] Diamanti K., and Soutis C., “Structural health monitoring techniques for aircraft composite structures,” *Prog. Aerosp. Sci.*, vol. 46, no. 8, pp. 342–352, Nov. 2010, DOI: 10.1016/j.paerosci.2010.05.001.
- [16] Missouri S., Allami M., Boutyour E., and Errkik A., “Delamination Localization in Sandwich Skin Using Lamb Waves by Finite Element Method,” *Adv. Acoust. Vib.*, vol. 2018, Jan. 2018, DOI: 10.1155/2018/9705407.
- [17] Shoja S., Berbyuk V., and Boström A., “Delamination detection in composite laminates using low frequency guided waves: Numerical simulations,” *Compos. Struct.*, vol. 203, pp. 826–834, Nov. 2018, DOI: 10.1016/j.compstruct.2018.07.025.
- [18] Kreja I. and Sabik A., “Equivalent single-layer models in deformation analysis of laminated multilayered plates,” *Acta Mech.*, vol. 230, no. 8, pp. 2827–2851, Aug. 2019, DOI: 10.1007/s00707-01902434-7.
- [19] Su Z., Ye L., and Lu Y., “Guided Lamb waves for identification of damage in composite structures: A review,” *J. Sound Vib.*, vol. 295, no. 3, pp. 753–780, Aug. 2006, DOI: 10.1016/j.jsv.2006.01.020.
- [20] Singh R., Ramadas C., Misal R., and Thakur D., “Numerical Analysis of Lamb Wave Propagation in Delaminated Composite Laminate,” *Procedia Eng.*, vol. 38, pp. 2510–2519, Jan. 2012, DOI: 10.1016/j.proeng.2012.06.296.
- [21] Masurkar F. and Yelve N., “LambWave Based Experimental and Finite Element Simulation Studies for Damage Detection in an Aluminium and a Composite Plate using Geodesic Algorithm,” *Int. J. Acoust. Vib.*, vol. 22, pp. 413–421, Feb. 2015, DOI: 10.20855/ijav.2017.22.4486.
- [22] Liu Z., “Lamb Wave Analysis of Acousto-Ultrasonic Signals in Plate.” <https://www.ndt.net/article/wcndt00/papers/idn602/idn602.html> (accessed Nov. 02, 2021).
- [23] Mohamed R. and Mason P., “Ansys Tutorial for Lamb Waves Propagation,” *pdfcoffee.com*. <https://pdfcoffee.com/ansys-tutorial-for-lamb-waves-propagation-pdf-free.html> (accessed Nov. 02, 2021).
- [24] “What is a Piezo Transducer?” <https://www.americanpiezo.com/piezo-theory/whats-atransducer.html> (accessed Dec. 14, 2021).
- [25] Bhalla S. and Moharana S., “Modelling of Piezo-Bond Structure System for Structural Health Monitoring Using EMI Technique,” Jul. 2013, vol. 569–570. DOI: 10.4028/www.scientific.net/KEM.569570.1234.
- [26] Hernandez-Fajardo L., Evangelatos G., Kougioumtzoglou I., Ming X., “Signal Denoising using Wavelet-based Methods - ELEC 301 Projects Fall 2008 - OpenStax CNX.” <https://cnx.org/contents/ahcuwm3R@1.1:-yxzQLO-@2/Signal-Denoising-using-Wavelet-based-Methods> (accessed Apr. 08, 2022).
- [27] “Choose a Wavelet - MATLAB & Simulink.” <https://www.mathworks.com/help/wavelet/gs/choose-a-wavelet.html> (accessed Apr. 08, 2022).
- [28] “Ansys mechanical | structural FEA analysis software.” <https://www.ansys.com/products/structures/ansys-mechanical> (accessed: 20-May-2022)

## 9. Appendices

### A. Sensor output results

TIME	Healthy	damaged
2.00E-06	-6.97E-18	-4.86E-18
4.00E-06	-2.52E-17	-1.11E-17
6.00E-06	-1.12E-15	-7.85E-16
8.00E-06	-1.26E-14	-9.99E-15
1.00E-05	-3.76E-14	-3.49E-14
1.20E-05	9.03E-14	4.97E-14
1.40E-05	7.53E-13	6.14E-13
1.60E-05	1.17E-12	1.23E-12
1.80E-05	-1.66E-12	-8.02E-13
2.00E-05	-5.79E-12	-5.30E-12
2.20E-05	1.65E-12	-1.25E-12
2.40E-05	1.60E-11	1.35E-11
2.60E-05	-1.47E-12	5.98E-12
2.80E-05	-3.36E-11	-2.79E-11
3.00E-05	6.39E-12	-1.02E-11
3.20E-05	5.29E-11	4.75E-11
3.40E-05	-2.94E-11	2.43E-12
3.60E-05	-5.14E-11	-6.21E-11
3.80E-05	7.60E-11	2.97E-11
4.00E-05	-1.08E-11	4.52E-11
4.20E-05	-1.06E-10	-7.20E-11
4.40E-05	1.57E-10	3.49E-11

Figure A.1 - Sensor 1 data output sample. Columns 2 and 3 correspond to individual voltages collected during each simulation separately. First with a pristine plate sample, followed by a damaged plate sample.

TIME	EP (V)
2.00E-06	-2.11E-18
4.00E-06	-1.41E-17
6.00E-06	-3.33E-16
8.00E-06	-2.64E-15
1.00E-05	-2.70E-15
1.20E-05	4.06E-14
1.40E-05	1.39E-13
1.60E-05	-5.53E-14
1.80E-05	-8.58E-13
2.00E-05	-4.90E-13
2.20E-05	2.90E-12
2.40E-05	2.52E-12
2.60E-05	-7.45E-12
2.80E-05	-5.74E-12
3.00E-05	1.66E-11
3.20E-05	5.37E-12
3.40E-05	-3.18E-11
3.60E-05	1.08E-11
3.80E-05	4.63E-11
4.00E-05	-5.59E-11
4.20E-05	-3.41E-11
4.40E-05	1.22E-10

Figure A.2 - Sensor 1 electric potential difference between healthy and damaged plate output sample

TIME	Healthy	Damaged	
2.00E-06	1.87E-15	1.87E-15	
4.00E-06	2.19E-14	2.19E-14	
6.00E-06	1.79E-14	1.81E-14	
8.00E-06	-3.89E-13	-3.89E-13	
1.00E-05	-8.85E-13	-8.88E-13	
1.20E-05	1.91E-12	1.89E-12	
1.40E-05	5.94E-12	5.93E-12	
1.60E-05	-5.51E-12	-5.39E-12	
1.80E-05	-1.81E-11	-1.79E-11	
2.00E-05	1.87E-11	1.85E-11	
2.20E-05	3.06E-11	2.96E-11	
2.40E-05	-6.23E-11	-6.21E-11	
2.60E-05	-1.13E-11	-9.10E-12	
2.80E-05	1.41E-10	1.40E-10	
3.00E-05	-9.72E-11	-1.01E-10	
3.20E-05	-1.76E-10	-1.72E-10	
3.40E-05	2.84E-10	2.87E-10	
3.60E-05	3.26E-11	2.04E-11	
3.80E-05	-3.21E-10	-3.20E-10	
4.00E-05	1.97E-10	2.20E-10	
4.20E-05	-2.83E-11	-4.06E-11	
4.40E-05	3.85E-11	6.35E-12	

Figure A.3 - Sensor 2 data output sample. Columns 2 and 3 correspond to individual voltages collected during each simulation separately. First with a pristine plate sample, followed by a damaged plate sample.

TIME	EP (V)
2.00E-06	6.70E-19
4.00E-06	-1.66E-17
6.00E-06	-2.04E-16
8.00E-06	-5.03E-16
1.00E-05	2.77E-15
1.20E-05	1.69E-14
1.40E-05	1.03E-14
1.60E-05	-1.21E-13
1.80E-05	-2.52E-13
2.00E-05	2.38E-13
2.20E-05	9.93E-13
2.40E-05	-2.42E-13
2.60E-05	-2.15E-12
2.80E-05	8.97E-13
3.00E-05	3.33E-12
3.20E-05	-4.14E-12
3.40E-05	-3.09E-12
3.60E-05	1.22E-11
3.80E-05	-1.34E-12
4.00E-05	-2.37E-11
4.20E-05	1.22E-11
4.40E-05	3.21E-11

Figure A.4 - Sensor 2 electric potential difference between healthy and damaged plate output sample

## B. MATLAB codes

### B.1 Geodesic location, damage modelling and damage approximation Matlab code

```
clear all
clc
t = linspace(0,2*pi,200);

%% composite plate 2d cut damage
figure(1)
% plate dimensions and plot
rectangle('position',[0 0 0.05 .05]);
hold on

%sensors 2d dimensions/locations on plate face
rectangle('position',[0 0 .01 .01],'FaceColor','r');
hold on
rectangle('position',[0.04 0 .01 .01],'FaceColor','c');
hold on
rectangle('position',[0.04 0.04 .01 .01],'FaceColor','c');

% modeled damage plot
rectangle('position',[0.025 0.01 .005 .03],'FaceColor','none');

% plotting ellipses

%ellipse center
x_c1 = 0.045;
y_c1 = 0.01;
r1 = .0282;
%ellipse x,y coordinates
x_t1 = r1*cos(t) + x_c1;
y_t1 = r1*sin(t) + y_c1;
a = plot(x_t1,y_t1,'r');
hold on

%ellipse center
x_c2 = 0.04;
y_c2 = 0.04;
r2 = .0057;
%ellipse x,y coordinates
x_t2 = r2*cos(t) + x_c2;
y_t2 = r2*sin(t) + y_c2;
b = plot(x_t2,y_t2,'r');

% limits and labels
xlim([0, 0.05]);
ylim([0, 0.05]);
title('Damaged (cut) composite plate geodesics');
xlabel('length [m]');
ylabel('width [m]');
```

```

annotation('textbox', [0.13, 0.1, 0.1, 0.1], 'String', "actuator",
'LineStyle','none');
annotation('textbox', [0.75, 0.1, 0.1, 0.1], 'String', "sensor
1",'LineStyle','none');
annotation('textbox', [0.75, 0.8, 0.1, 0.1], 'String', "sensor
2",'LineStyle','none');
annotation('textbox', [0.52, 0.5, 0.1, 0.1], 'String', "modeled
damage",'LineStyle','none');
grid on
hold off

figure(2)
% plate dimensions and plot
rectangle('position',[0 0 0.05 .05]);
hold on

%sensors 2d dimensions/locations on plate face
rectangle('position',[0 0 .01 .01],'FaceColor','r');
hold on
rectangle('position',[0.04 0 .01 .01],'FaceColor','c');
hold on
rectangle('position',[0.04 0.04 .01 .01],'FaceColor','c');

% modeled damage plot
rectangle('position',[0.025 0.01 .005 .03],'FaceColor','none');

% plotting ellipses

%ellipse center
x_c1 = 0.045;
y_c1 = 0.001;
r1 = .0327;
%ellipse x,y coordinates
x_t1 = r1*cos(t) + x_c1;
y_t1 = r1*sin(t) + y_c1;
a = plot(x_t1,y_t1,'r');
hold on

%ellipse center
x_c2 = 0.049;
y_c2 = 0.049;
r2 = .0207;
%ellipse x,y coordinates
x_t2 = r2*cos(t) + x_c2;
y_t2 = r2*sin(t) + y_c2;
b = plot(x_t2,y_t2,'r');

% limits and labels
xlim([0, 0.05]);
ylim([0, 0.05]);
title('Damaged (cut) composite plate geodesics');
xlabel('length [m]');

```

```

ylabel('width [m]');

annotation('textbox', [0.13, 0.1, 0.1, 0.1], 'String', "actuator",
'LineStyle','none');
annotation('textbox', [0.75, 0.1, 0.1, 0.1], 'String', "sensor
1",'LineStyle','none');
annotation('textbox', [0.75, 0.8, 0.1, 0.1], 'String', "sensor
2",'LineStyle','none');
annotation('textbox', [0.52, 0.5, 0.1, 0.1], 'String', "modeled
damage",'LineStyle','none');
grid on
hold off
%q = InterX([a;b]);

figure(3)
% plate dimensions and plot
rectangle('position',[0 0 0.05 .05]);
hold on

%sensors 2d dimensions/locations on plate face
rectangle('position',[0 0 .01 .01],'FaceColor','r');
hold on
rectangle('position',[0.04 0 .01 .01],'FaceColor','c');
hold on
rectangle('position',[0.04 0.04 .01 .01],'FaceColor','c');

% modeled damage plot
rectangle('position',[0.025 0.01 .005 .03],'FaceColor','none');

% plotting ellipses

%ellipse center
x_c1 = 0.045;
y_c1 = 0.001;
r1 = .0432;
%ellipse x,y cordinates
x_t1 = r1*cos(t) + x_c1;
y_t1 = r1*sin(t) + y_c1;
a = plot(x_t1,y_t1,'r');
hold on

%ellipse center
x_c2 = 0.049;
y_c2 = 0.049;
r2 = .0441;
%ellipse x,y cordinates
x_t2 = r2*cos(t) + x_c2;
y_t2 = r2*sin(t) + y_c2;
b = plot(x_t2,y_t2,'r');

% limits and labels
xlim([0, 0.05]);
ylim([0, 0.05]);
title('Damaged (cut) composite plate geodesics');

```

```

xlabel('length [m]');
ylabel('width [m]');

annotation('textbox', [0.13, 0.1, 0.1, 0.1], 'String', "actuator",
'LineStyle','none');
annotation('textbox', [0.75, 0.1, 0.1, 0.1], 'String', "sensor
1",'LineStyle','none');
annotation('textbox', [0.75, 0.8, 0.1, 0.1], 'String', "sensor
2",'LineStyle','none');
annotation('textbox', [0.52, 0.5, 0.1, 0.1], 'String', "modeled
damage",'LineStyle','none');
grid on
hold off
%q = InterX([a;b]);

%% composite plate 2d delamination damage
figure(4)
% plate dimensions and plot
rectangle('position',[0 0 0.05 .05]);
hold on

%sensors 2d dimensions/locations on plate face
rectangle('position',[0 0 .01 .01],'FaceColor','r');
hold on
rectangle('position',[0.04 0 .01 .01],'FaceColor','c');
hold on
rectangle('position',[0.04 0.04 .01 .01],'FaceColor','c');

% modeled damage plot
rectangle('position',[0.030 0 .01 .01],'FaceColor','none');

% plotting ellipses

%ellipse center
x_c1 = 0.04;
y_c1 = 0.01;
r1 = .0145;
%ellipse x,y coordinates
x_t1 = r1*cos(t) + x_c1;
y_t1 = r1*sin(t) + y_c1;
a = plot(x_t1,y_t1,'r');
hold on

%ellipse center
x_c2 = 0.04;
y_c2 = 0.04;
r2 = .0222;
%ellipse x,y coordinates
x_t2 = r2*cos(t) + x_c2;
y_t2 = r2*sin(t) + y_c2;
b = plot(x_t2,y_t2,'r');

% limits and labels
xlim([0, 0.05]);

```

```

ylim([0, 0.05]);
title('Damaged (delamination) composite plate geodesics');
xlabel('length [m]');
ylabel('width [m]');

annotation('textbox', [0.13, 0.1, 0.1, 0.1], 'String', "actuator",
'LineStyle','none');
annotation('textbox', [0.75, 0.1, 0.1, 0.1], 'String', "sensor
1",'LineStyle','none');
annotation('textbox', [0.75, 0.8, 0.1, 0.1], 'String', "sensor
2",'LineStyle','none');
annotation('textbox', [0.59, 0.12, 0.1, 0.1], 'String', "modeled
damage",'LineStyle','none');
grid on
hold off

figure(5)
% plate dimensions and plot
rectangle('position',[0 0 0.05 .05]);
hold on

%sensors 2d dimensions/locations on plate face
rectangle('position',[0 0 .01 .01],'FaceColor','r');
hold on
rectangle('position',[0.04 0 .01 .01],'FaceColor','c');
hold on
rectangle('position',[0.04 0.04 .01 .01],'FaceColor','c');

% modeled damage plot
rectangle('position',[0.030 0 .01 .01],'FaceColor','none');

% plotting ellipses

%ellipse center
x_c1 = 0.045;
y_c1 = 0.001;
r1 = .0153;
%ellipse x,y coordinates
x_t1 = r1*cos(t) + x_c1;
y_t1 = r1*sin(t) + y_c1;
a = plot(x_t1,y_t1,'r');
hold on

%ellipse center
x_c2 = 0.049;
y_c2 = 0.04;
r2 = .0294;
%ellipse x,y coordinates
x_t2 = r2*cos(t) + x_c2;
y_t2 = r2*sin(t) + y_c2;
b = plot(x_t2,y_t2,'r');

% limits and labels

```

```

xlim([0, 0.05]);
ylim([0, 0.05]);
title('Damaged (delamination) composite plate geodesics');
xlabel('length [m]');
ylabel('width [m]');

annotation('textbox', [0.13, 0.1, 0.1, 0.1], 'String', "actuator",
'LineStyle','none');
annotation('textbox', [0.75, 0.1, 0.1, 0.1], 'String', "sensor
1", 'LineStyle','none');
annotation('textbox', [0.75, 0.8, 0.1, 0.1], 'String', "sensor
2", 'LineStyle','none');
annotation('textbox', [0.59, 0.12, 0.1, 0.1], 'String', "modeled
damage", 'LineStyle','none');
grid on
hold off
%q = InterX([a;b]);

figure(6)
% plate dimensions and plot
rectangle('position',[0 0 0.05 .05]);
hold on

%sensors 2d dimensions/locations on plate face
rectangle('position',[0 0 .01 .01], 'FaceColor','r');
hold on
rectangle('position',[0.04 0 .01 .01], 'FaceColor','c');
hold on
rectangle('position',[0.04 0.04 .01 .01], 'FaceColor','c');

% modeled damage plot
rectangle('position',[0.030 0 .01 .01], 'FaceColor','none');

% plotting ellipses

%ellipse center
x_c1 = 0.045;
y_c1 = 0.001;
r1 = .0297;
%ellipse x,y coordinates
x_t1 = r1*cos(t) + x_c1;
y_t1 = r1*sin(t) + y_c1;
a = plot(x_t1,y_t1, 'r');
hold on

%ellipse center
x_c2 = 0.049;
y_c2 = 0.049;
r2 = .0447;
%ellipse x,y coordinates
x_t2 = r2*cos(t) + x_c2;
y_t2 = r2*sin(t) + y_c2;
b = plot(x_t2,y_t2, 'r');

```

```

% limits and labels
xlim([0, 0.05]);
ylim([0, 0.05]);
title('Damaged (delamination) composite plate geodesics');
xlabel('length [m]');
ylabel('width [m]');

annotation('textbox', [0.13, 0.1, 0.1, 0.1], 'String', "actuator",
'LineStyle', 'none');
annotation('textbox', [0.75, 0.1, 0.1, 0.1], 'String', "sensor
1", 'LineStyle', 'none');
annotation('textbox', [0.75, 0.8, 0.1, 0.1], 'String', "sensor
2", 'LineStyle', 'none');
annotation('textbox', [0.59, 0.12, 0.1, 0.1], 'String', "modeled
damage", 'LineStyle', 'none');
grid on
hold off
%q = InterX([a;b]);

%% damage locations
figure(7)
% plate dimensions and plot
rectangle('position', [0 0 0.05 .05]);
hold on

%sensors 2d dimensions/locations on plate face
rectangle('position', [0 0 .01 .01], 'FaceColor', 'r');
hold on
rectangle('position', [0.04 0 .01 .01], 'FaceColor', 'c');
hold on
rectangle('position', [0.04 0.04 .01 .01], 'FaceColor', 'c');

% modeled damage plot
rectangle('position', [0.025 0.01 .005 .03], 'FaceColor', 'none');

% approximate damage plot
aproxdl = [.03545 .03665 .01075 .03545; .03656 .03239 .02705 .03656];
plot(aproxdl(1,:), aproxdl(2,:))

% limits and labels
xlim([0, 0.05]);
ylim([0, 0.05]);
title('Modeled and approximate cut location on damaged composite plate');
xlabel('length [m]');
ylabel('width [m]');

annotation('textbox', [0.13, 0.1, 0.1, 0.1], 'String', "actuator",
'LineStyle', 'none');
annotation('textbox', [0.75, 0.1, 0.1, 0.1], 'String', "sensor
1", 'LineStyle', 'none');
annotation('textbox', [0.75, 0.8, 0.1, 0.1], 'String', "sensor
2", 'LineStyle', 'none');
annotation('textbox', [0.52, 0.5, 0.1, 0.1], 'String', "modeled
damage", 'LineStyle', 'none');
grid on

```

```

hold off

figure(8)
% plate dimensions and plot
rectangle('position',[0 0 0.05 .05]);
hold on

%sensors 2d dimensions/locations on plate face
rectangle('position',[0 0 .01 .01],'FaceColor','r');
hold on
rectangle('position',[0.04 0 .01 .01],'FaceColor','c');
hold on
rectangle('position',[0.04 0.04 .01 .01],'FaceColor','c');

% modeled damage plot
rectangle('position',[0.030 0 .01 .03],'FaceColor','none');

% aproximate damage location
aproxd2 = [.0190 .03621 .04996 .0190; .01581 .020164 .02032 .01581];
plot(aproxd2(1,:),aproxd2(2,:))

% limits and labels
xlim([0, 0.05]);
ylim([0, 0.05]);
title('Modeled and approximate delamination location on damaged composite
plates');
xlabel('length [m]');
ylabel('width [m]');

annotation('textbox', [0.13, 0.1, 0.1, 0.1], 'String', "actuator",
'LineStyle','none');
annotation('textbox', [0.75, 0.1, 0.1, 0.1], 'String', "sensor
1",'LineStyle','none');
annotation('textbox', [0.75, 0.8, 0.1, 0.1], 'String', "sensor
2",'LineStyle','none');
annotation('textbox', [0.59, 0.12, 0.1, 0.1], 'String', "modeled
damage",'LineStyle','none');
grid on
hold off

```

C. Geodesics from additional simulations  
C.1 Geodesic plots incorporating enlarged modeled delamination

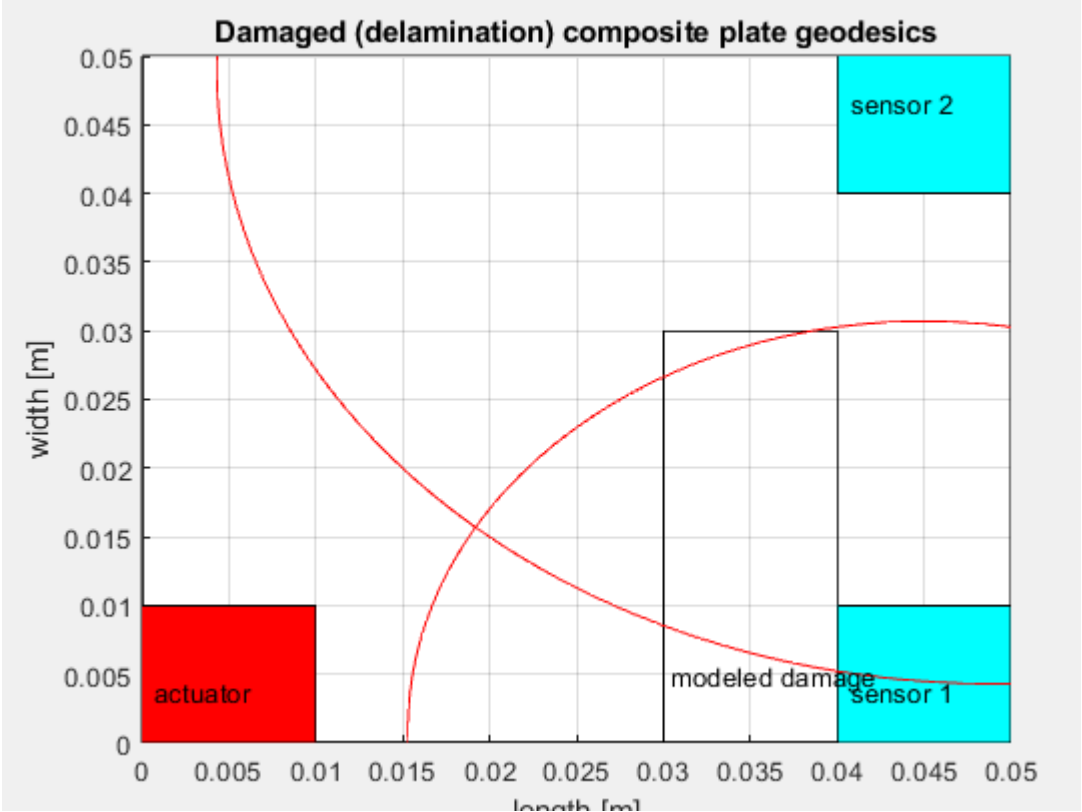


Figure C.1 – Geodesic plot approximating damage location on a delaminated composite plate. Delamination size enlarged relative to previous simulations.

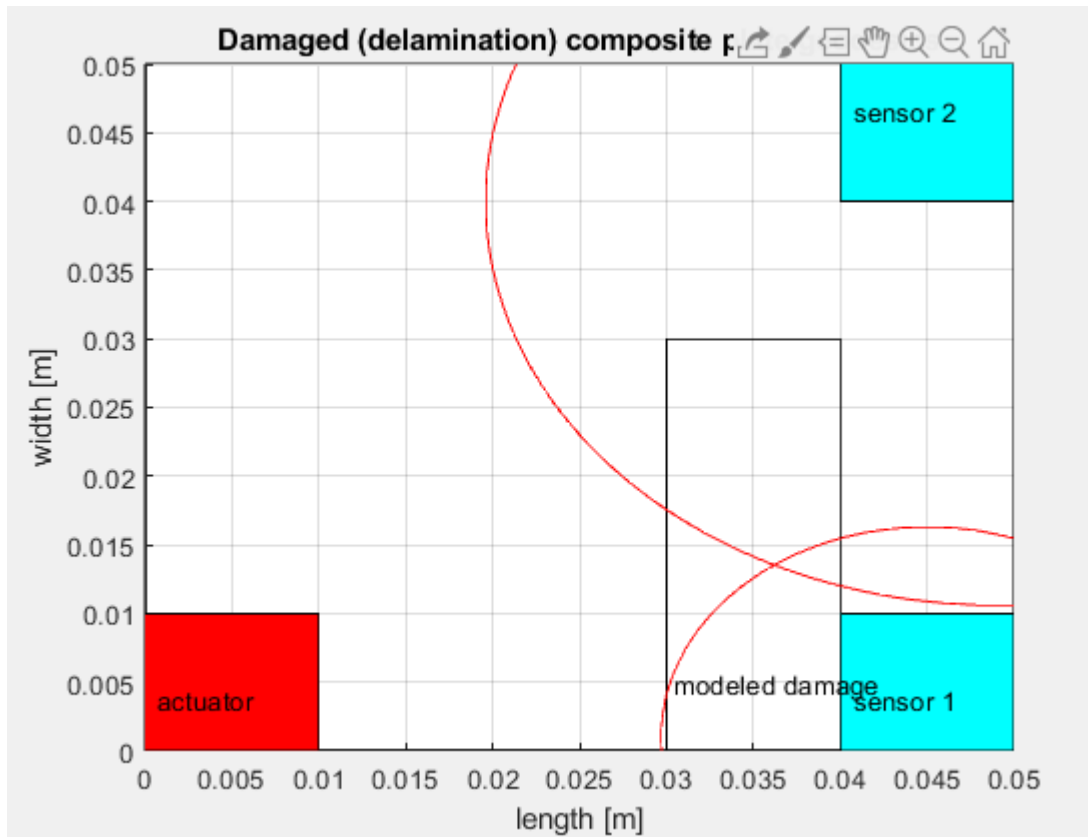


Figure C.2 – Geodesic plot approximating damage location on a delaminated composite plate. Delamination size enlarged relative to previous simulations.

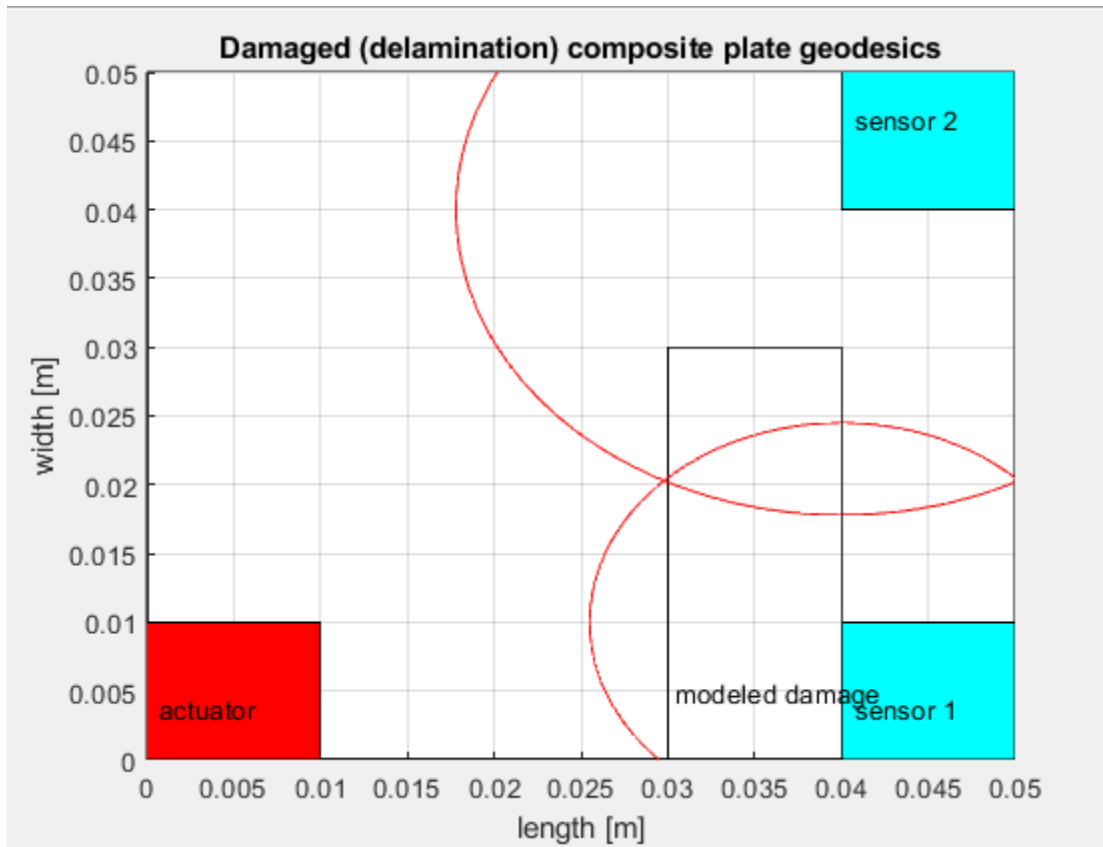


Figure C.3 – Geodesic plot approximating damage location on a delaminated composite plate. Delamination size enlarged relative to previous simulations.